COMSAT
Technical Review

Volume 16 Number 2, Fall 1986

Advisory Board Joseph V. Charyk
John V. Evans

Editorial Board Geoffrey Hyde, Chairman
Richard A. Arndt
Ali E. Atia
S. Joseph Campanella
Dattakumar M. Chitre
Russell J. Fang
Howard W. Flieger
Melvyn Grossman
Ivor N. Knight
Larry C. Palmer
Edward E. Reinhart
David V. Rogers
Hans J. Weiss
Albert E. Williams
Pier L. Bargellini, Editor Emeritus

Editorial Staff
MANAGING EDITOR
Margaret B. Jacocks
TECHNICAL EDITORS
Barbara J. Wassell
Diane Haugen
PRODUCTION
Barbara J. Wassell
Louis P. Stephens, Jr.
CIRCULATION
Shirley H. Taylor
Shirley T. Cofield

COMSAT TECHNICAL REVIEW is published twice a year by Communications Satellite Corporation (COMSAT). Subscriptions, which include the two issues published within a calendar year, are: one year, $15 U.S.; two years, $25; three years, $35; single copies, $10; article reprints, $2.50. Overseas air mail delivery is available at an additional cost of $18 per year. Make checks payable to COMSAT and address to Records Department, Communications Satellite Corporation, 22300 Comsat Drive, Clarksburg, MD 20871-9475, U.S.A.

© COMMUNICATIONS SATELLITE CORPORATION 1986
COMSAT IS A TRADE MARK AND SERVICE MARK
OF THE COMMUNICATIONS SATELLITE CORPORATION

COMSAT TECHNICAL REVIEW

Volume 16 Number 2, Fall 1986

319 MULTIPATH FADING CHARACTERIZATION OF L-BAND MARITIME MOBILE SATELLITE LINKS **W. A. Sandrin** AND **D. J. Fang**

339 20-GHz PHASED-ARRAY-FED ANTENNAS UTILIZING DISTRIBUTED MMIC MODULES **R. M. Sorbello, A. I. Zaghloul, B. S. Lee, S. Siddiqi,** AND **B. D. Geller**

375 A COMPARISON OF THREE MAC TV TRANSMISSION FORMATS **L. C. Palmer**

425 LOW-COMPLEXITY CODING METHODS FOR HIGH-DATA-RATE CHANNELS **F. Hemmati** AND **R. J. F. Fang**

449 A BOUND ON DIURNAL ERROR IN PREDICTED RANGES OF NEARLY GEOSTATIONARY SATELLITES **P. C. Kammeyer**

CTR NOTES

459 NEW ANODE CATALYST FOR THE NEGATIVE ELECTRODE OF THE NICKEL-HYDROGEN BATTERY **H. Vaidyanathan**

467 SYNTHESIZED C-BAND DOWN-CONVERTER **E. W. Rothermich** AND **S. T. Williams**

481 TRANSLATIONS OF ABSTRACTS
FRENCH 481 SPANISH 484

Index: antennas, communication satellites, mobile communication systems, propagation

Multipath fading characterization of L-band maritime mobile satellite links*

W. A. SANDRIN AND D. J. FANG

(Manuscript received December 2, 1985)

Abstract

Models of the maritime multipath fading process oriented toward communications systems engineers are presented. These models are primarily based on experimental data obtained from several sources and include both fading amplitude and time/frequency models. The fading amplitude models consist of both a Ricean model for fading statistics, which is applicable for most of the time, and a specular reflection model that assumes a smooth sea. The models are described parametrically in terms of elevation angle and ship earth station antenna gain. Fading (or Doppler) spectrum, fade duration times, and correlation bandwidths are also characterized. Finally, methods for combating multipath fading applicable to commercial maritime communications are surveyed.

Introduction

In a commercial maritime satellite communications system such as that operated by INMARSAT, ship earth stations (SESs) operating at L-band (approximately 1.6 GHz up-link and 1.5 GHz down-link) are used for the SES-to-satellite links. Multipath fading caused by reflections from the sea

* This paper is based on work performed at COMSAT Laboratories under the sponsorship of the International Maritime Satellite Organization (INMARSAT). Views expressed are not necessarily those of INMARSAT.

surface can significantly impair this type of channel, especially at low elevation angles or when SESs having low-gain antennas are used.

The bulk of the literature has concentrated either on the physics of this phenomenon or on specific experiments. In contrast, this paper presents a series of characterizations and simple models that describe the overall multipath fading process in terms directly useful to communications engineers.

The characterizations and models described here are based primarily on experimental results obtained from the open literature and from recent data furnished by the DFVLR.* Both fading amplitude and time/frequency characterizations are given. For the case of fading amplitude, models for both rough and smooth sea states are included. Time/frequency characteristics are described in terms of fading spectrum, fade duration statistics, and correlation bandwidth. Various methods for combating multipath fading are also described.

Multipath fading amplitude

It is well known [1] that multipath reflections from the sea surface consist of specular and diffuse components. The relative strength of these components is a function of wave height and, to a lesser extent, elevation angle [2]. For calm sea states, the specular component dominates, but diminishes rapidly as wave height increases. For relatively small wave heights, the strength of the diffuse component increases rapidly with height and becomes essentially constant for greater wave heights. For example, at a 10° elevation angle and a wave height of 0.5 m (measured crest to trough), the specular component has a very low level while the diffuse component has reached the same level as for higher waves. At a 5° elevation angle, the strength of the specular component is higher, it is not reduced to as low a level, and the diffuse component does not reach a relatively constant level until the wave height is about 1 m.

Karasawa and Shiokawa [3] give plots of sea state probability densities for various ocean regions. These plots show that wave heights are usually greater than 0.5 m and less than 5 m. Based on these considerations and the observation (discussed later) that most of the experimental data on multipath fading amplitudes are essentially independent of sea state, it is assumed for the purpose of systems design and performance analysis that rough sea conditions will exist for most of the time, and thus amplitude fading can be expressed in statistical terms. However, on the relatively infrequent occasions

* Deutsche Forschungs- und Versuchsanstalt für Luft- und Raumfahrt (German Institute for Aerospace Research).

when specular reflections dominate, these must also be considered. In this situation, fade amplitudes cannot be characterized in statistical terms, and a model that assumes a perfectly smooth sea is used to obtain a bound on fade depth extremes. Information is also given on the sensitivity of fade depths as the sea varies from perfectly smooth to a slightly rough condition.

Statistical model for multipath fading amplitudes

For a satellite maritime mobile link where the dominant component of multipath is diffuse, the signal can be represented by one large (direct-component) vector to which many smaller vectors are added. The in-phase and quadrature components of these smaller vectors have a zero-mean Gaussian distribution, so that the amplitude of the multipath component is Rayleigh-distributed and its phase is uniformly distributed over 2π.

The theoretical description of this process as one having Ricean statistics is presented by Beckmann and Spizzichino [1], and the Ricean process itself is described in a number of textbooks as well as in References 4, 5, and 6. The key parameter in a Ricean distribution is the ratio of the direct component power to the power in the multipath component. This is defined as the Rice factor, C/M. Figure 1 gives the probability that the composite signal is above a certain level (with respect to the total signal power) for the Rice factor values of interest.

To obtain a generalized model for amplitude fading statistics, experimental data from a number of sources [5]–[16] were examined. The resulting model is parametric in SES antenna gain and elevation angle, and this factor is used to determine the probability distribution function, as illustrated in Figure 1.

The data in several of the sources are presented in terms of Rice factors, while the data in the remaining sources are described in terms sufficient to allow estimation of a Rice factor. In general, nearly all of the experimental data (except for cases of very low sea state and elevation angle) have been found to be a good fit to the Ricean distribution, at least in the range of percent-of-time values (from 90 to 99 percent) which are of greatest interest to maritime communications engineers.

The Rice factors determined for the source data were plotted as a function of elevation angle for different SES antennas. A linear fit of Rice factor *vs* elevation angle was made to the plotted points for each antenna gain value, and the resulting linear relationships were evaluated to form a general model of Rice factor *vs* elevation angle for antenna gain values covering the range of applicable SES antennas. This model, shown in Figure 2, can be described as follows:

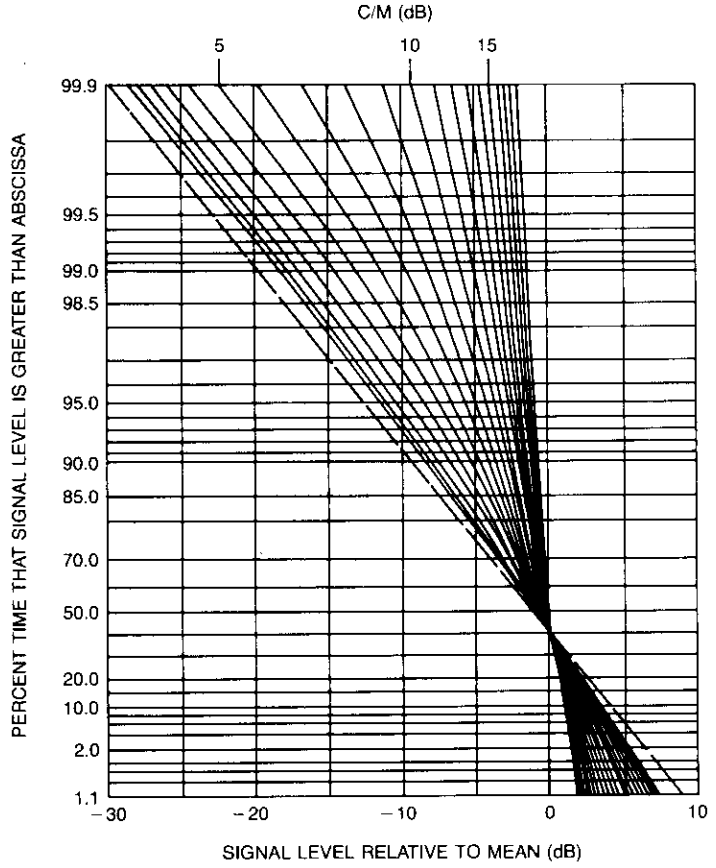

Figure 1. *Ricean Probability Distribution Function for Various Values of Rice Factor, C/M [6]*

a. For antenna gains from 0 to 16 dBi, the Rice factor is given by

$$C/M = E\ell + 4 \qquad 2° \leq E\ell \leq 4°$$

where C/M is the Rice factor in decibels and $E\ell$ is the elevation angle in degrees.

b. For antennas with gains ranging from 0 to 16 dBi, the Rice factor for elevation angles greater than 4° is given by a line passing through the point (C/M = 8 dB, $E\ell$ = 4°) and the point defined by the C/M value given in Figure 3 at $E\ell$ = 16°.

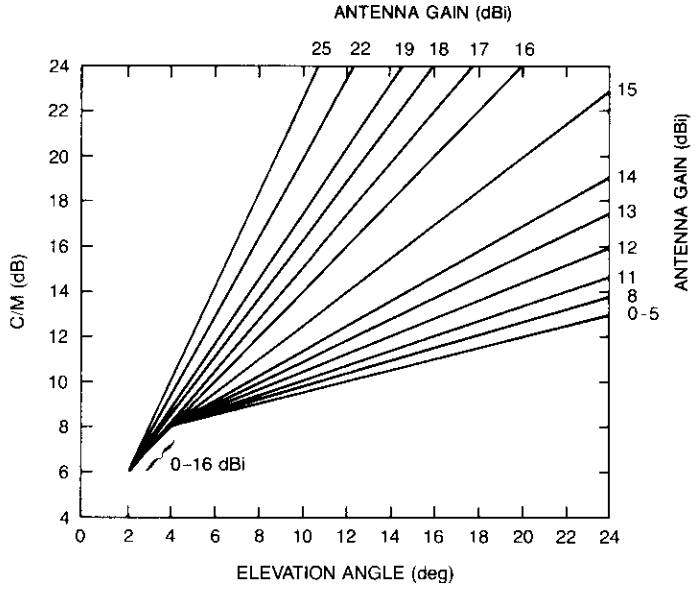

Figure 2. *C/M vs Elevation Angle: Generalized Model*

c. For antennas with gains ranging from 16 to 25 dBi, the Rice factor for elevation angles greater than 2° is given by a line passing through the point (C/M = 6 dB, $E\ell$ = 2°) and the point defined by the C/M value given in Figure 3 at $E\ell$ = 16°.

d. For elevation angles and C/M values outside the boundaries of Figure 2 (*i.e.*, $C/M > 24$ dB and $E\ell > 24°$), little experimental evidence is available to provide an adequate model, except for some medium and low antenna gains (<14 dB) which indicate that the model can be extrapolated up to at least $E\ell$ = 28°.

Figures 1, 2, and 3 can be used together to obtain information for a given SES antenna gain and elevation angle. This information will generally typify the channel (*i.e.*, non-smooth sea states), subject to the qualifications noted below.

Antenna pattern effects

In most of the experimental data used as the basis for the generalized Ricean fading model shown in Figure 2, antenna performance was specified simply by gain (dBi). However, different antennas having the same gain can

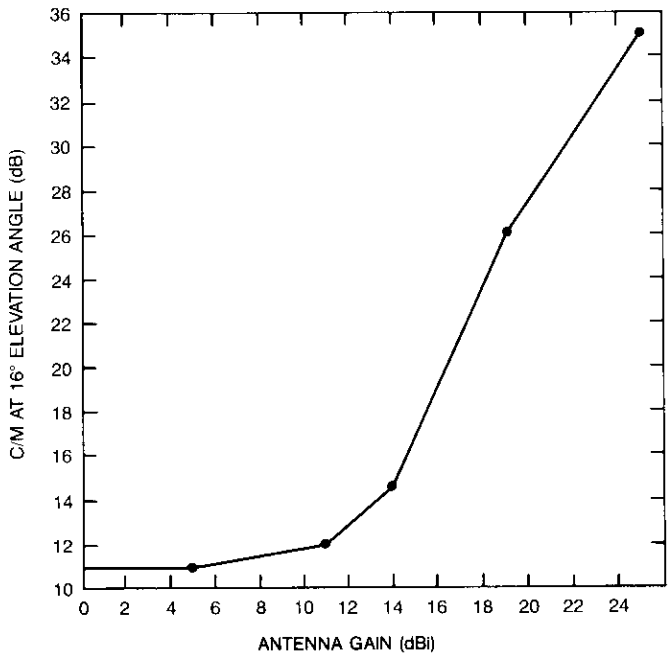

Figure 3. *Rice Factor Values at $E\ell = 16°$ for Generalized Model*

exhibit major differences in radiation patterns. Because of this pattern variation, it is especially difficult to generalize fading *vs* elevation angle for low-gain antennas. Hence, in Figure 2 the same curve is used for antennas having gains of from 0 to 5 dBi. Pattern shapes that provide multipath rejection are difficult to generalize in this range, but are usually broad enough so that pattern discrimination is small at low elevation angles.

Multipath discrimination depends not only on the antenna pattern, but also on the mount, which for low-gain omni-azimuthal antennas may be either fixed or horizontally stabilized.

The 0- to 5-dBi curve in Figure 2 fits very closely to the 5-dBi antenna fading data listed in Reference 5, and fits reasonably closely to the data computed for an isotropic (0 dBi) antenna. These latter values are derived by using the modeled curves for gains of 10 dBi and above and subtracting computed pattern discrimination effects, assuming that the mainlobe of the antenna is pointed at the satellite and that the major portion of the diffuse multipath comes from a point approximately halfway between the point of specular reflection and the horizon. This assumption regarding the origin of diffuse multipath is supported by Figure 4 of Reference 2.

At higher elevation angles, the 0- to 5-dBi curve of Figure 2 is not a good fit to data measured with a 3-dBi antenna, as given in Reference 5. For example, the Rice factor at a 16° elevation angle is 11 dB for the model of Figure 2 and about 9.6 dB for a linear fit to the experimental data, while at a 24° elevation angle, the Rice factors are 13 and 10.2 dB, respectively. This observation suggests that for low-gain antennas and elevation angles higher than about 15°, the model of Figure 2 may not accurately predict Rice factors, in part because of low-gain antenna pattern variations.

For antennas with gains above 10 dBi, it can be assumed that coverage is not omni-azimuthal and that the patterns have well-defined main lobes so that the antennas must be pointed at the satellite. Although the experimental results used to model Rice factors for antenna gains of 10 dBi and higher in Figure 2 did not always explicitly state that active tracking was employed, this condition was assumed for antennas in this gain range.

Variability of experimental data and adequacy of Ricean distribution

The model shown in Figure 2 is a generalization of several sources of experimental data and provides the systems analyst with a good basis for characterizing fading amplitude statistics. However, in a practical application it must be recognized that the model may not accurately predict fading amplitude statistics for a specific antenna over any one particular time duration. Also, the fading amplitude statistics may not be exactly a Ricean process. The reasons for the variability of low-gain antennas have already been discussed. This section examines the nature of the model inaccuracies and the resulting impact in terms of system analysis.

Comparison of the experimental results of References 5 through 16 with the generalized model shown in Figure 2 reveals that the Rice factors generally cluster within ± 2 dB for a given antenna gain and elevation angle, although points outside of this range are not uncommon. Also, many of the points shown in the various experimental results are averages of several observations.

The model of Figure 2 is intended to represent typical fading characteristics by generalizing the results of several different experiments. As such, it is not a worst-case model. For a worst-case analysis, the use of a somewhat lower Rice factor would be appropriate. A more conservative (but still not worst-case) condition could be achieved by lowering the Rice factor 1 dB for low elevation angles ($<10°$) and 2 dB for higher elevation angles.

The DFVLR reports [5],[6] show that experimental results for fading amplitude closely match Ricean distributions. Data from other sources, which describe fading in terms of percent time, generally closely fit Ricean distributions for time percentages of 90 to 99. Since this is the range of

greatest interest for systems analysis, the use of the Ricean distribution for this application is considered to be reasonable.

Polarization effects

Since the model shown in Figure 2 is based on experimental results using nominally circularly polarized antennas, it includes the effect of imperfectly polarized SES and satellite antennas. An analysis of the effect of polarization impurities on fading statistics revealed that, for antennas having axial ratios of 2 dB or lower, the polarization impurity effect would be negligible in a diffuse multipath environment. The effects of polarization impurities on the specular multipath model, and the use of polarization shaping as a means of reducing fade depth, are discussed in subsequent sections.

Comparison of Rice factor model with additional experimental results

After the model shown in Figure 2 was formulated, Hagenauer *et al.* [17] obtained additional experimental results in the form of a series of Rice factor *vs* elevation angle plots for a number of SES antennas having gains in the 9.5- to 17-dBi range. These are independent data against which the model can be compared. Table 1 presents such a comparison for Rice factors at a 10° elevation angle. For all cases except one, the Rice factor comparisons are within 1 to 2 dB, with the Rice factor for the data of Reference 16 always being higher than that predicted by Figure 2. The data of Reference 17 also show that individual data points (*i.e.*, Rice factors for individual test runs) occasionally have a significant variability about the straight-line relationships that are fitted to the data points.

An explanation of why these new results exhibit systematically better *C/M* (*i.e.*, have higher Rice factors, which translates to less severe multipath fading) than the model developed here cannot be given without more details

TABLE 1. COMPARISON BETWEEN MODEL SHOWN IN FIGURE 2 AND RESULTS FROM REFERENCE 17

ANTENNA GAIN (dBi)	RICE FACTOR AT 10° AS GIVEN BY REFERENCE 17	RICE FACTOR AT 10° AS GIVEN BY FIGURE 2
9.5	11.0	9.9
9.8	15.8	9.9
11.5	12.0	10.2
12.5	11.8	10.6
15.0	14.7	12.5
17.0	16.2	15.0

regarding all the experiments. However, the difference is small, especially at low elevation angles. Also, from a systems analysis viewpoint, it is preferable that the generalized model be slightly conservative.

Worst-case model for smooth sea

A smooth-sea model is used, together with the diffuse multipath model described in the preceding section, to provide the systems analyst with a range of possible fading conditions. No directly applicable experimental results were found. However, since the physics in this case is straightforward, a theoretical relationship is sufficient. References 2, 18, and 19 describe theoretical models for the specularly reflected component, and the plots given here are based on results given in Reference 18.

Reference 18 plots the worst-case fade levels for a number of situations. Figure 4 is a plot based on results shown in Reference 18 for an isotropic antenna and illustrates how worst-case specular reflection is affected by surface roughness. Figure 5 uses the smooth-sea curve of Figure 4 to illustrate fade depth for different antenna gains. Figure 5 was obtained by computing

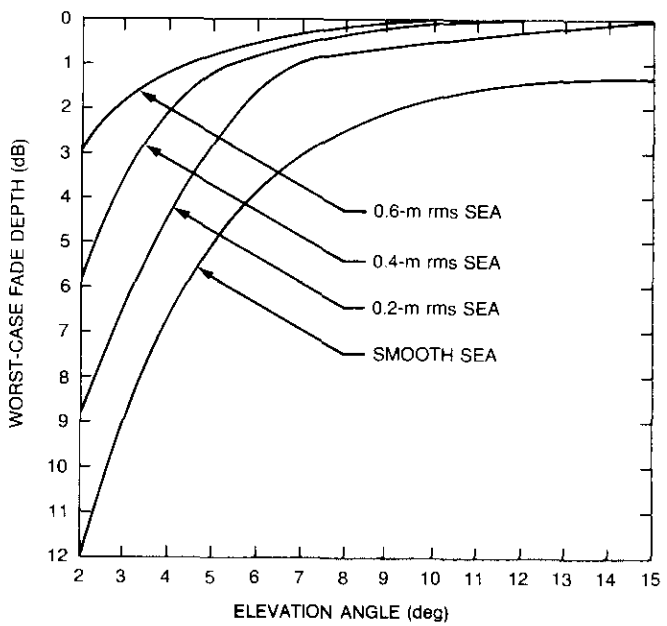

Figure 4. *Worst-Case Fade Depth for Specular Reflection: Isotropic Antenna Assumed [18]*

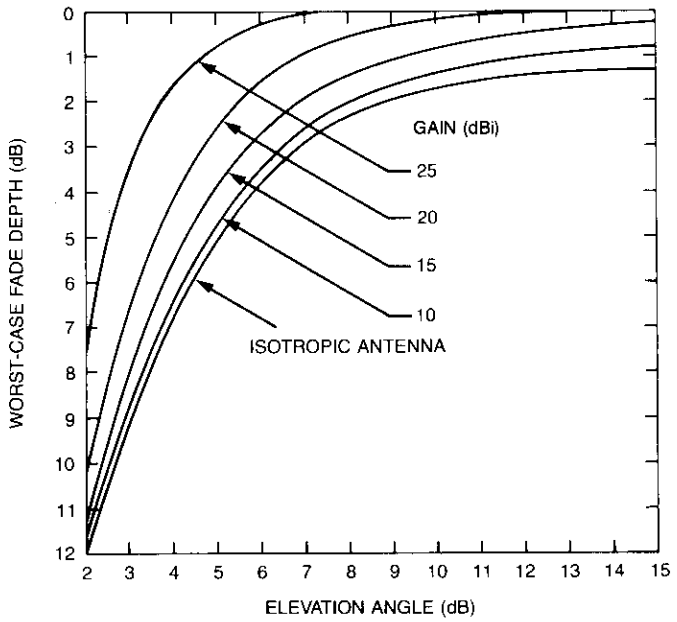

Figure 5. *Worst-Case Fade Depth for Specular Reflection: Smooth Sea Assumed*

antenna pattern effects for the gain values illustrated, assuming that the antennas are pointed directly toward the satellite.

By using Figure 5 to obtain a worst-case fade level for the relatively rare event of a nearly smooth sea, and by combining this information with results obtained from the generalized Ricean model (described in the preceding section) for the usual condition of rough seas, the systems analyst can bracket the fade amplitudes that will occur over the range of SES antenna gains and elevation angles of interest.

Time/frequency characterizations

Wave motion and ship motion produce differential Doppler shifts in the reflected multipath components, and this effect determines important aspects of the fading process such as the multipath spectrum, fade duration times, fade rates, and interfade intervals. This section summarizes the results of a review of experimental fading spectra and fade duration times. Because these results are difficult to summarize in the form of a generalized model, as was possible for the fading amplitude statistics, examples of reduced data are presented and generalizations are made regarding these processes.

Multipath fading spectrum

The fading spectrum is commonly used to describe the time/frequency characteristics of the multipath fading process. A number of multipath fading spectrum measurements have been made for an L-band satellite-to-SES link [5],[7],[8],[11]–[13],[20],[21], and these were reviewed to obtain a generalized description. The bulk of the data on fading spectra (from Reference 5) were obtained for SES antennas having gains in the range of 3 to 13 dBi, at various elevation angles. Reference 20 also contains a significant amount of data.

Based on the data surveyed, the maritime multipath fading spectrum was characterized. The -3 dB bandwidth ranges from values on the order of 0.1 Hz to values of about 1 Hz, while the -20 dB bandwidth is usually within the 3- to 8-Hz range, although its extremes range from slightly below 1 Hz to greater than 10 Hz. This general characterization is qualified as follows:

a. Within the limits given above, the 3-dB spectral width tends to become narrower and the 20-dB spectral width tends to become wider as the elevation angle increases.

b. Generally, a weak relationship exists between sea state and spectral width, with calm seas producing narrower spectra. In the limit, a systems analysis should consider the case of a nearly perfectly calm sea where the spectrum will be very narrow and the fade durations long.

c. Some of the measured fading spectra reviewed may have contained other propagation anomalies, particularly ionospheric scintillation effects [22].

d. Within the limits given above, the consistency among the experimental results is adequate for systems analysis purposes.

Fade duration times

Although the distribution of fade durations and other characteristics of the fading process can be approximated from the fading spectrum by using either analytic or time domain simulation techniques, actual measured data are preferable. In analysis and simulation techniques, assumptions of stationarity and a lack of higher order statistics prevent the derivation of an accurate description of the fading process from the fading spectrum. For example, periodic effects of both ship motion and wave motion may have a strong influence on the nature of fades, but may not strongly influence the fading spectrum itself.

Only one data source provided reduced fade measurements for an L-band satellite-to-SES link in terms other than the fading spectrum [5]. These data consist of a large number of measurements made at various elevation angles using several SES antennas that ranged in gain from 3 to 13 dBi. Hagenauer *et al.* reduced these measurements to a series of plots that include the following for each measurement period of about 2 hours:

- fading power spectrum;
- autocorrelation estimate (Fourier transform of the fading power spectrum);
- distribution function of fade durations, conditioned by the existence of a fade;
- distribution function of connection durations (where a connection is the opposite of a fade), conditioned by the existence of a connection;
- distribution function of fade durations;
- distribution of fade levels;
- distribution of connection levels;
- maximum length of fades;
- maximum length of connections;
- mean length and mean plus standard deviation of fades; and
- mean length and mean plus standard deviation of connections.

A detailed examination of the fade duration distributions of Reference 5 revealed significant variability in the mean and maximum fade duration times at a given fade depth, even for experiments where differences appear to be minor. Therefore, it is difficult to generalize the results into a simple working assumption model, although fade durations tend to be slightly shorter with increasing elevation angle. This is due in part to multipath spectrum broadening at higher elevation angles, and in part to the higher Rice factor values that occur at higher elevation angles.

Table 2 presents a concise summary of fade duration times as obtained from the data Reference 5, and provides the systems analyst with the range of fade duration times that can be expected for low-gain antennas (3 to 13 dBi) at various fade depth thresholds.

Delay spread and coherence bandwidth

The specular and diffuse components of multipath transmission have propagation times that differ from the direct component and differ from one another. This delay spread effect has a Fourier transform relationship to the coherence or correlation bandwidth. Because of the relatively narrow

TABLE 2. SUMMARY OF MEASURED FADE DURATION TIMES

FADE THRESHOLD* (dB)	MEAN FADE LENGTH RANGE (s)	MAXIMUM FADE LENGTH RANGE (s)
−2	0.02–0.17	0.3–3.5
−5	<0.01–0.12	<0.01–1.6
−8	<0.01–0.08	<0.01–0.9

* Relative to mean received power.

transmission bandwidths and short differential path lengths that characterize a maritime mobile satellite link, these effects are usually not important considerations for commercial maritime transmissions.

Although no directly applicable experimental results were found in regard to delay spread or coherence bandwidth, Reference 23 gives a simplified analysis in which an entire coherence bandwidth of 11 MHz (or about a 5-MHz, 3-dB bandwidth) was roughly estimated for the system geometry assumed (a 20-m SES antenna height and a 20° elevation angle).

One experimental result not directly applicable is an aeronautical experiment described by Thompson *et al.* [24]. For transoceanic flights, 3-dB coherence bandwidths of 200 kHz were typically measured for 15° to 30° elevation angles at a flight altitude of 30,000 ft. Because of extreme height relative to an SES antenna, the coherence bandwidth was much narrower than for the maritime case.

For engineering purposes, it can be concluded that the coherence bandwidth for commercial maritime applications is significantly larger than the signaling bandwidths, and is probably on the same order as (or somewhat narrower than) the 15-MHz up- and down-link L-band allocation bandwidths. However, it is much smaller than the 101.5 MHz that separates the up- and down-link L-band allocations.

Multipath fading reduction techniques

A number of fading reduction techniques are available to the systems designer, including polarization shaping, multi-element antenna systems, forward error correction (FEC) code interleaving, pattern shaping, and frequency diversity.

Polarization shaping

As described by Reed and Russell [25] and Katz [26], a horizontally polarized signal is reflected from a smooth sea with a small amount of attenuation and a phase reversal, whereas a vertically polarized component

is reflected without a phase reversal, but with a large amount of attenuation at low elevation angles. In terms of circular polarization, the reflected component of the same sense diminishes with increasing elevation angle, while the reflected component of the opposite sense increases with increasing elevation angle. These differences in the polarization of reflected multipath components can be exploited to reduce multipath fading by using either passive or active techniques.

In the passive technique, an antenna that is vertically polarized at low elevation angles is used to suppress multipath reflections. While such a solution is not practical for relatively high-gain directional antennas because of the resultant 3-dB loss in the direct component, it may be relevant to those antennas that provide hemispherical coverage, such as the low-gain Standard-C SESs.

With a hemispherical coverage antenna, it is not possible to provide pure circular polarization coverage over the entire hemisphere. For such an antenna at low elevation angles, a design in which polarization becomes increasingly more vertical as the elevation angle decreases may be preferable. In fact, ground plane effects make this a characteristic of certain hemispherical coverage antennas.

The optimum transition from circular to vertical polarization for this type of antenna is a tradeoff between direct component polarization loss and multipath rejection. Another factor involved in the design tradeoff is antenna gain *vs* elevation angle. Assuming a gravity-stabilized platform, the gain should be low at very low elevation angles, peak at moderately low elevation angles, and can be reduced at high elevation angles.

Kokusai Denshin Denwa Company, Ltd. (KDD) Laboratories has developed an active polarization shaping technique to achieve multipath fading reduction. The polarization ellipse is adjusted so that the antenna polarization is, as much as possible, orthogonal to the multipath reflections from the sea. In the implementations described in References 16 and 27, short-backfire and paraboloidal antennas are fed by a pair of crossed dipoles, with the antenna ellipticity controlled by a variable phase shifter in the feed of one of the dipoles. In the process of adjusting the polarization ellipse for optimum fading reduction, the axial ratio is altered from pure circular polarization to the point where the polarization loss for the direct component is 1 to 2 dB.

Although more testing and development are needed before the active polarization shaping technique can become operational, this technique demonstrates a definite advantage. Table 3 summarizes the KDD experimental results and shows approximately a 1- to 3-dB improvement in 99-percent fade levels for 10° elevation angles, and from 4- to 5-dB improvement at 5°.

TABLE 3. SUMMARY OF 99-PERCENT FADE LEVEL IMPROVEMENTS FOR VARIOUS POLARIZATION SHAPING TESTS

ANTENNA GAIN (dBi)	ELEVATION ANGLE (deg)	MODE	FADING IMPROVEMENT DUE TO POLARIZATION SHAPING* (dB)
13	11.2	Receive	2.6
13	11.2	Receive	2.2
15	5	Receive	4.8
15	5	Transmit	3.9
15	10	Receive	1.1
15	10	Transmit	2.8
13	7.2	Receive	4.0

* Includes approximately 1.5-dB reduction of direct signal due to polarization shaping.

Multi-element antenna systems design

An SES antenna system with multiple elements can be designed in a number of ways to protect against fading. The simplest implementation is a switched spatial diversity scheme in which the elements can either be spaced closely (in which case vertical arrangements are preferable), or distributed at various points about the ship. Although the latter arrangement has the advantage of providing protection against superstructure blockage, the expense of multiple installation locations and extra cabling will probably make such a scheme too expensive to be practical.

An array of closely spaced antenna elements can be actively controlled to provide maximum signal strength, as well as protection against multipath fading. Such techniques are described in References 23 and 28, where two schemes are preferred: a self-phasing design (equivalent to maximum-ratio predetection diversity combining) and a digitally adaptive array controlled by a microprocessor.

Another approach described by KDD [16],[27] is the maximum-level tracking method in which a single phase shift value is used in two elements of a quad-helix antenna (positive value in one element, negative in another) to control the antenna pattern in the vertical plane. This scheme has been implemented and tested in a controlled environment (on a beach, with a signal source located on a hill across a bay). The results have demonstrated a significant amount of fading reduction as well as enhancement in the average signal level.

FEC code interleaving

The use of interleaved FEC codes has been investigated by both DFVLR [5],[6],[29] and COMSAT Laboratories [30]. In this scheme, code symbols

are interleaved at the transmitter and de-interleaved at the receiver prior to decoding. This process randomizes and spreads out burst errors caused by deep fades, and thus preserves the error correction features of the code.

Although treated independently of other fading reduction techniques, the use of interleaving combined with a simple fading reduction technique such as polarization shaping may be worthy of further investigation. The performance of FEC code interleaving alone is limited in the maritime channel because fade durations are relatively long compared to transmission rates and burst rates, unless complex schemes requiring large buffers are used. Similarly, the single control element used in the polarization shaping scheme limits performance in a diffuse multipath environment. However, when the two schemes are used together, the fading reduction provided by polarization shaping might permit the use of a simplified interleaving scheme, resulting in performance equivalent to that of a more complex interleaving technique.

The disadvantage of FEC interleaving is that it uses the time domain and hence cannot be used for duplex voice communications because of delays that are on the order of a few seconds.

Pattern shaping

Another fading reduction approach suggested by KDD [16] is based on the use of an SES antenna having a very sharp cutoff below the horizon, that is, in the direction of the multipath. For a directional antenna, this approach requires a highly tapered aperture distribution with resulting low antenna efficiency. However, this concept may be more applicable to hemispherical coverage antennas where both directivity and polarization characteristics at very low elevation angles can be used to minimize fading and maximize signal levels for relatively low elevation angles.

Frequency diversity

Brief studies of frequency diversity [16],[23] have concluded that this technique is not practical for commercial maritime applications because the correlation bandwidth (approximately 10 MHz) is on the same order as the bandwidth allocated for the maritime mobile service (15 MHz).

Summary and conclusions

Models for the multipath fading process have been presented that are oriented toward the systems engineer. These include both fading amplitude and time/frequency models, and are based largely on experimental data. Additionally, techniques to combat multipath fading that are applicable to commercial maritime communications links have been surveyed.

Regarding the Ricean model presented for fading amplitude statistics, the consistency among several sources of data for SES antennas greater than 10 dBi and for elevation angles greater than 5° confirms that the Ricean model is valid in this range. However, less experimental data are available for lower elevation angles and lower SES antenna gains, and the results are not as consistent. This may be due in part to varying pattern shapes for low-gain SES antennas. Additional experimental data for these cases would be useful.

Further experimental data would also be useful in measuring the performance of the various antifade schemes surveyed.

In contrast to the experimentally based and application-oriented models described in this paper, theoretical models are based on multipath propagation physics. Of these models, the one described by Karasawa and Shiokawa [2] appears to be the most detailed and completely developed. However, in its published form, quantitative fading information for specific antenna gains, elevation angles, and sea states is difficult to obtain.

The reflections and blockage caused by ship superstructure is an important topic that has not been addressed in this paper. Much less theoretical material and experimental data were found on this subject than on multipath reflections from the sea. Therefore, it is recommended that more emphasis be placed on this topic in the future.

Acknowledgments

The results presented in this paper are a condensation of the results of a study contract performed by COMSAT Laboratories for INMARSAT, which has kindly given permission for publication of the material and has supplied much of the referenced material to the authors. D. R. Mullins, INMARSAT Contract Technical Monitor, has provided much valuable assistance and guidance in this work.

The kind cooperation of J. Hagenauer and his colleagues of the DFVLR in providing their extensive and recently obtained measured data on multipath fading amplitude and time/frequency characteristics is also very much appreciated. The work done at the DFVLR on the topic of the maritime satellite communications channel will be summarized in a forthcoming paper [31].

References

[1] P. Beckmann and S. Spizzichino, *The Scattering of Electromagnetic Waves From Rough Surfaces*, Elmsford, New York: Pergamon Press, 1963.

[2] Y. Karasawa and T. Shiokawa, "Characteristics of L-Band Multipath Fading due to Sea Surface Reflection," *IEEE Transactions on Antennas and Propagation*, Vol. AP-32, No. 6, June 1984, pp. 618–623.

[3] Y. Karasawa and T. Shiokawa, "Analysis of Multipath Fading due to Sea Surface Scattering in Maritime Satellite Communication," Technical Group on Antennas and Propagation, IECE, Japan, October 1980.

[4] K. A. Norton *et al.*, "The Probability Distribution of the Amplitude of a Constant Vector Plus a Rayleigh-Distributed Vector," *Proc. IRE*, Vol. 43, No. 10, October 1955, pp. 1354–1361.

[5] J. Hagenauer *et al.*, "Multipath Fading Effects and Data Transmission for Small Ship Earth Stations (Standard C)," DFVLR, Final Report for ESA/ESTEC Contract 5323/82/NL/JS, November 15, 1984.

[6] DFVLR, "Technical Assistance Study of Lightweight Shipborne Terminals," Final Report for ESA/ESTEC Contract 4786/81/NL/MD, April 1982.

[7] J. Hagenauer *et al.*, "Propagation Experiments for Distress Transmitter Buoys and Its Application for CCIR Satellite EPIRB System Tests," DFVLR/NTNF Report, 1982.

[8] D. J. Fang, F. T. Tseng, and T. O. Calvit, "A Measurement of the MARISAT L-Band Signals at Low Elevation Angles Onboard Mobile Aero," *IEEE Transactions on Communications*, Vol. COM-30, No. 2, February 1982, pp. 359–365.

[9] CCIR, "Proposed Modification to Draft Report AQ/8, Results of Measurement of 1.5-GHz Multipath Fading," CCIR Study Group Document 8/380-E, May 7, 1981.

[10] CCIR, "Proposed Amendment to Report 763-1: Signal Level Variation due to Multipath Effect Over Links of the Maritime Mobile-Satellite Service," CCIR Study Group Document 8/28-E, January 16, 1984.

[11] CCIR, "Signal Level Variation due to Multipath Effect Over Links of the Maritime Mobile-Satellite Service," 1975 Satellite-to-Ship Tests, Report 763-1, Vol. VIII, XVth Plenary Assembly, Geneva, 1982.

[12] CCIR, "Maritime Satellite Tests in Band 9 (UHF)," Report 598-1, Vol. VIII, XIVth Plenary Assembly, Kyoto, 1978.

[13] CCIR, "Effects of Multipath on Digital Transmission Over Links in the Maritime Mobile-Satellite Service," DFVLR Data on Standard-A Terminal, Report 762-1, XVth Plenary Assembly, Geneva, 1982.

[14] CCIR, "U.S. ATS-6 Tests Averaged Results 1974–1975," Report 762-1, XVth Plenary Assembly, Geneva, 1982.

[15] A. Davies and R. J. Kemp, "Signal Fading Data at L-Band (1.5 GHz) due to Multipath Reflections From the Sea," IEE International Conference on Maritime and Aeronautical Satellite Communication and Navigation, London, March 1978.

[16] Kokusai Denshin Denwa Company Ltd., "Studies on Digital Transmission Systems Applicable to the INMARSAT System," Vols. I and II, Techical Note 162, KDD Research and Development Laboratories, Japan, 1982.

[17] Appendix to Reference 5, 1985.

[18] General Electric (British), "Report on Standard A Antenna Propagation Studies," for INMARSAT contract, 1983.

[19] D. J. Fang and R. H. Ott, "A Low Elevation Angle L-Band Maritime Propagation Measurement and Modeling," Third International Conference on Satellite Systems for Mobile Communications and Navigation, *IEE Conference Publication 222*, June 1983, p. 45.

[20] Y. Karasawa and T. Shiokawa, "Spectrum of L-Band Multipath Fading due to Sea Surface Reflection," *Transactions IECE*, (in Japanese), Japan, Vol. J67-B, No. 2, 1984, pp. 171–178.

[21] C. I. Beard and I. Katz, "The Dependence of Microwave Radio Signal Spectra on Ocean Roughness and Wave Spectra," *IRE Transactions on Antennas and Propagation*, Vol. AP-5, April 1957, pp. 183–191.

[22] D. J. Fang and C. H. Liu, "Statistical Characterizations of Equatorial Scintillation in the Asian Region," *Radio Science*, Vol. 19, No. 1, January–February 1984, pp. 345–358.

[23] COMSAT Laboratories, "Study of Various System Aspects Related to the Use of Standard-C Ship Earth Stations in the INMARSAT System," Final Report for INMARSAT Contract 006, 1982.

[24] A. D. Thompson *et al.*, "Air Traffic Control Experimention and Evaluation with the NASA ATS-6 Satellite: Multipath Channel Characterization Tests," FAA Report FAA-RD-75-173, Vol. V, 1976.

[25] H. R. Reed and C. M. Russell, *Ultra High Frequency Propagation*, Lexington, Massachusetts: Boston Technical Publishers, 1964.

[26] I. Katz, "Radar Reflectivity of the Ocean Surface for Circular Polarization," *IEEE Transactions on Antennas and Propagation*, Vol. AP-11, No 4, July 1963, pp. 451–453.

[27] T. Shiokawa and Y. Karasawa, "Shipborne Antennas Suppressing Multipath Fading in Maritime Satellite Communication," IEEE AP-S International Symposium, Albuquerque, New Mexico, May 1982, *Digest*, Vol. 2, pp. 390–393.

[28] W. A. Sandrin and E. Carpenter, "Antenna Studies for INMARSAT Standard-C Terminal," Third International Conference on Satellite Systems for Mobile Communications and Navigation, *IEE Conference Publication 222*, June 1983, pp. 125–129.

[29] E. Lutz, "Code and Interleaver Design for Data Transmission Over Fading Channels," IEEE Global Telecommunications Conference, Atlanta, Georgia, November 1984, *Conference Record*, Vol. 1, pp. 381–386.

[30] COMSAT Laboratories, "Digital Modulation and Coding Techniques Applicable to INMARSAT Standard-C Ship Earth Stations," Final Report for INMARSAT Contract INM/83-063, October 1984.

[31] J. Hagenauer *et al.*, "The Maritime Satellite Communication Channel—Channel Model, Performance of Modulation and Coding," provisionally accepted for publication in *IEEE Transactions on Selected Areas in Communications*.

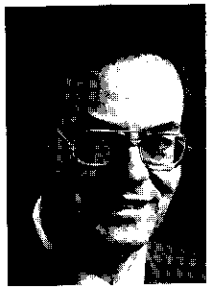

William A. Sandrin received a B.S.E.E. degree from the University of Vermont in 1963, and an M.E.E. degree from Rensselaer Polytechnic Institute in 1966. From 1966 to 1971, he worked for the Boeing Company, Aerospace Group, where he was involved in space communications system design and in the development of phased-array antennas. In 1971, he joined COMSAT Laboratories, where he has been engaged in multibeam antenna studies; transponder linearizer development; transmission impairments analysis; studies of domestic, maritime, and aeronautical satellite systems; a study of adaptive phased-array antennas for small-terminal applications; and frequency planning studies. He is presently Manager of the Systems Modeling and Analysis Department of the Communications Techniques Division. Mr. Sandrin is a member of IEEE, Tau Beta Pi, and Eta Kappa Nu.

Dickson J. Fang received a B.S.E.E. in 1962 from Taiwan University, Taipei, China, and an M.S.E.E. and Ph.D. from Stanford University in 1964 and 1967, respectively. From 1967 to 1974, he was a Radio Physicist at Stanford Research Institute studying electromagnetic wave propagation, radio auroras, and ionospheric irregularities. While on leave from Stanford (1969–1970), he was a visiting professor at Taiwan University, where he published a graduate textbook on electromagnetic theory.

Dr. Fang joined the Propagation Studies Department at COMSAT Laboratories in 1974 and became Manager in 1980. He was involved in studies of ionospheric scintillations, the effects of precipitation on microwave transmission, and atmospheric optical transmission characterizations. In 1985, he left COMSAT to become Vice President of the Massachusetts Technological Laboratory. He is the author or co-author of more than 50 technical papers.

Index: antennas, communication satellites, phased-array antennas, satellite antennas, multibeam antennas, microwave integrated circuits, MMICs

20-GHz phased-array-fed antennas utilizing distributed MMIC modules

R. M. SORBELLO, A. I. ZAGHLOUL, B. S. LEE, S. SIDDIQI, AND B. D. GELLER

(Manuscript received May 3, 1985)

Abstract

This paper describes multiple scanning-beam and multiple fixed-beam antenna systems operating at 20 GHz which utilize monolithic microwave integrated circuit (MMIC) modules that provide both RF power and dynamic phase control. Specific array-fed dual-reflector configurations presented include a phased array feeding a pair of confocal parabolas for both the scanning-beam and fixed-beam applications, and a focal-region-fed Cassegrain system for fixed-beam application. A reflector geometry, feed element, and array design are developed for each configuration, and secondary radiation patterns are computed to determine the achievable e.i.r.p. levels, sidelobe isolation, and cross-polarization isolation. The secondary radiation patterns are calculated using a new method in which the phased array for each scanning direction is simulated by a fictitious point source, thus performing the ray tracing and surface current integration in a time-efficient manner. The focal-region-fed Cassegrain reflector was judged better for fixed multiple-beam applications, while the phased-array-fed, dual-reflector configuration was chosen for multiple scanning beams. Breadboard models were fabricated and tested for some of the key elements in the phased-array design, which included radiating square horn, square orthomode transducer, and a waveguide-to-MMIC-to-waveguide transition to transform energy in the MMIC devices to either a waveguide or the radiating horn element.

Introduction

To accommodate the continued rapid growth of communications traffic (voice, data, and video), satellites will be required to provide increased

capacity. One way to achieve this is to operate at higher frequencies such as 20 and 30 GHz where the allocated bandwidths of 2.5 GHz are considerably larger than the bandwidths allocated at C-band and K_u-band. An even greater increase in capacity may be possible through advances in frequency reuse antenna technology.

Antennas that can provide multiple fixed or scanning beams at 20 GHz and have the potential to provide 6 to 18 times the frequency reuse have previously been investigated. Ford Aerospace Communications Corporation (FACC) [1] and TRW [2] have examined dual-reflector antenna systems that can generate multiple scanning or multiple fixed spot beams. Both antennas are focal-region-fed designs in which far-field beams are generated by clusters of feeds that comprise part of the total feed array. Scanning in these systems is accomplished by changing the amplitude distribution in the focal region. The radiated power for each beam is generated by a single traveling wave tube (TWT), which is sized to compensate for any output loss caused by multiplexers and beam-forming networks (BFNs). New antenna concepts that can provide a similar number of frequency reuses are described in this paper. Development of these antennas could provide the capacity required for future communications satellite systems.

With the advent of monolithic microwave integrated circuit (MMIC) amplifiers and phase shifters, new satellite architectures which blend both antenna and transponder technologies will be possible. This paper investigates such architectures by considering antenna systems that use distributed amplification and phase control. These antennas provide a number of scanning and fixed beams with a true phased array to feed a dual-reflector system. In this concept, all elements in the array (not just a cluster) are used to generate the far-field beams, and scanning is accomplished by varying the phase taper across the whole array.

The miniaturization of MMIC amplifiers and phase shifters allows these devices to be placed directly behind each radiating element, thus minimizing output loss and offering potential weight and volume savings over the more conventional approaches investigated in References 1 and 2. This marriage of antenna and transponder technologies enables a true systems approach to be employed in the design of these antennas. The antenna concepts addressed in this paper could provide for more rapid scanning and a higher e.i.r.p. level than are achievable with more conventional approaches. With future developments and improvements in MMIC devices, 20-GHz phased-array-fed antenna systems will become operational and will be key contributors to increased satellite capacity.

Coverage requirements

Coverage requirements for multiple scanning spot-beam and multiple fixed spot-beam operations dictate the performance prerequisites of the associated antenna systems. The angular field of view (FOV) for the coverage area determines the maximum scan requirements of an antenna system, while the spacing between frequency reuse beams is the driver for the required antenna aperture size.

The antennas presented in this paper are designed for continental United States (CONUS) coverage from a geosynchronous altitude at west longitudes of 90° to 105°. Composite antenna coverage is generated by overlaying the maps at the orbital extremes and applying up to ±0.6° of pitch bias to minimize the apparent spread of earth locations over the longitude range. The resulting antenna FOV, shown in Figure 1, is ±3.5° in azimuth and ±1.5° in elevation. This FOV determines the angular extent over which the optical system used should provide minimal scan loss.

In Figure 1a, CONUS is divided into six vertical sectors, each corresponding to one independent scanning beam and resulting in a sixfold frequency use. Any two adjacent sectors are orthogonally polarized to ensure isolation between co-polarized beams. The size of the individual scanning spot beams and their number in each sector are determined by the size of the main aperture of the reflector system. For example, a 3.8-m aperture will generate approximately 300 spot beams of 0.3° width for full CONUS coverage.

Figure 1b depicts the coverage configuration for the fixed spot-beam case where 18 such beams cover the population centers across the U.S. Each beam must be isolated from the others either spatially through sidelobe cancellation or by polarization. Since the angular spacing between two spatially isolated beams is related to the resolution of the reflector system [3], the smallest spacing required will determine the size of the reflector's main aperture. This relationship can be expressed as

$$\sigma = \frac{100\lambda}{D} \tag{1}$$

where σ is the interzone angular spacing in degrees and D is the required reflector diameter. This expression has been derived empirically for a 27-dB interzone isolation and verified on several INTELSAT programs. The Boston-to-Washington spacing is the closest and will be the driver for the main reflector size. At 105° west longitude, this spacing minimizes to 0.42°, which implies from the above expression that a reflector size of 3.58 m (11.75 ft) will be required.

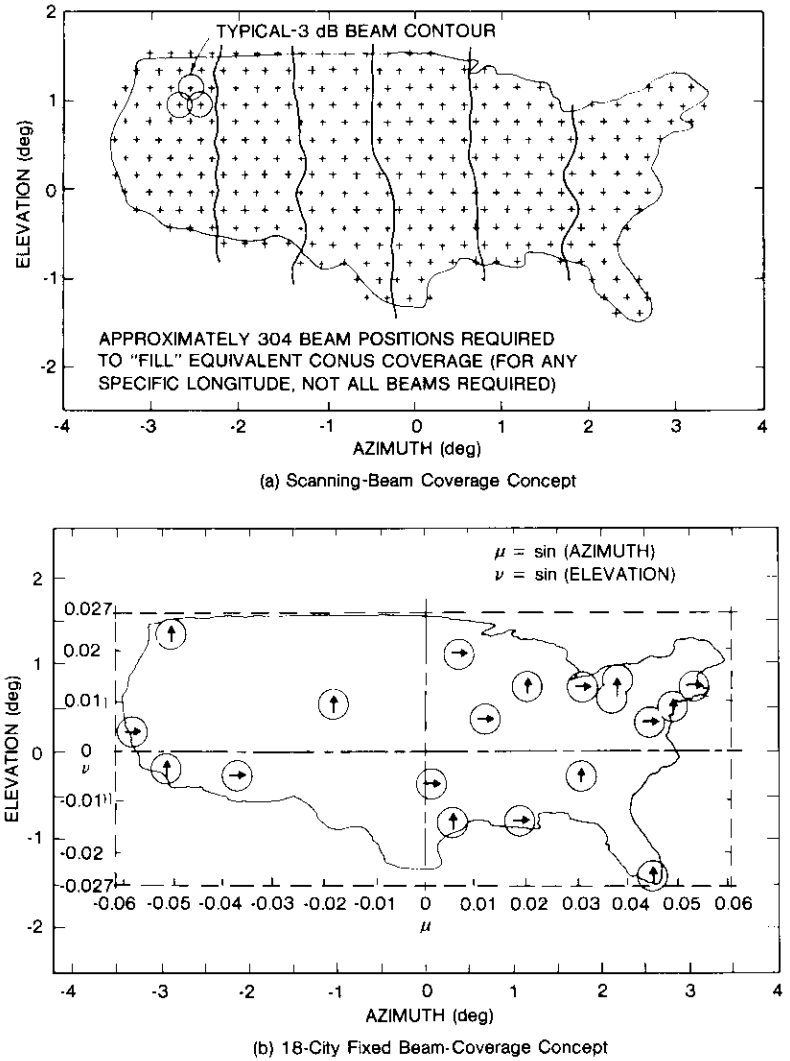

Figure 1. *Multiple Scanning and Multiple Fixed-Beam Coverages*

Phased-array vs focal-region-fed systems

With the availability of MMIC modules, new satellite system architectures based on an array-fed reflector system with distributed RF power may be attractive alternatives to the conventional focal-region-fed antenna systems

employed on most existing satellites. Figure 2 depicts two dual-reflector systems, each capable of forming both fixed and scanning beams but based on different principles.

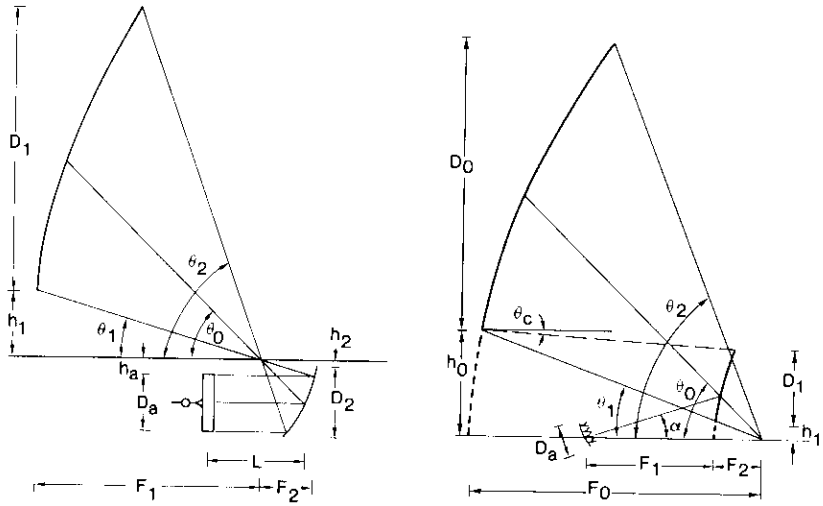

Figure 2. *Phased-Array-Fed and Focal-Region-Fed Dual-Reflector Systems*

The phased-array system utilizes all the elements in the array to form an incident wave on the subreflector surface. The subreflector exists in the near field of the array, and the optics are designed to transform the approximate plane wave of the array into a magnified version by using a pair of confocal parabolas (whose optics will be discussed later). A scanned beam is formed by adjusting the phase shifter setting on each element to vary the phase taper of the incident plane wave. Large e.i.r.p.'s can be achieved with this system via distributed amplifiers. For an amplifier with fixed output power, required RF powers can be obtained by increasing the number of elements in the array. Since the power amplifier stages are located close to the radiating elements, complex and lossy feed networks can be used earlier in the array without severely impacting the overall efficiency of the system. On the other hand, the amplifier efficiencies at the backed-off levels required for multisignal operation will affect overall system efficiency.

The focal-region-fed system typically employs an optical configuration that transforms a spherical wave generated by the feed array into a plane

wave in the far field. Scanning beams or multibeams are formed by using different portions of the feed cluster in the focal region. Cassegrain and Gregorian reflector systems are likely candidates for the optics. Movement of the beams in the far field is accomplished by displacement of the amplitude distribution among a cluster of feed elements. Since a relatively small number of elements (1, 7, or 19) are typically used to form each beam, large amounts of RF power cannot be achieved by distributed amplification. Typically, a high-powered TWT is placed before the BFN. Since the BFN can be quite complex (depending on the coverage requirement), the TWT must be of sufficient power to compensate for BFN losses and any additional loss (from multiplexers, circulators, switches, etc.) between the output of the TWT and the BFN. In this case, TWT efficiency at the backed-off level, along with BFN losses, are the primary factors in overall system efficiency.

To determine the viability of the phased-array approach with distributed amplifiers *vs* the conventional TWT configuration, a system comparison is performed based on the total DC-to-RF efficiency for the scanning-beam case. Figure 3 presents block diagrams of the power flow for the two approaches. The requirements for such a case are summarized in Table 1. The FOV is dictated by the required orbital locations of 90° to 105° W. The minimum edge of coverage (EOC) gains assume an antenna efficiency of 60 percent,

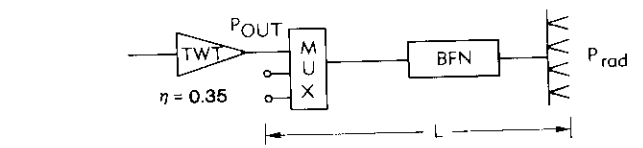

(a) Conventional (Focal-Region-Fed) Approach

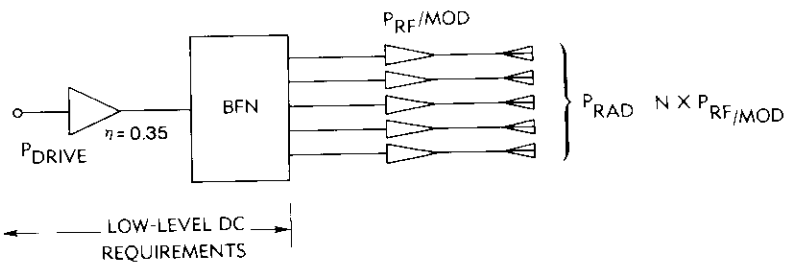

(b) Distributed Amplifier (Phased-Array-Fed) Approach

Figure 3. *Feeding Block Diagrams of Conventional and Distributed Amplifier Approaches*

TABLE 1. SCANNING BEAM ANTENNA SYSTEM REQUIREMENTS

PARAMETER	REQUIREMENT
Field of View	±3.5° E-W, ±1.5° N-S
Main Aperture	2.743–4.267 m
Frequency Range	17.7–20.2 GHz
Bandwidth	500 MHz
Component Beamwidth (3 dB)	0.4°–0.25°
Total No. of Beams (6 at any one time)	180–450
On-Axis Peak Gain (η = 0.6)	52.5–56.5 dBi
Minimum Gain in FOV (2.5-dB scan loss)	50–54 dBi
e.i.r.p.	67–75 dBW

which is typical for multibeam applications, and an EOC scan loss of 2.5 dB. Depending on the main reflector diameter, between 180 and 450 beam locations will be needed to provide the required coverage. At any instant, only six beams, corresponding to the six sectors, will exist. For comparison, a baseline 3.81-m (12.5-ft) reflector capable of achieving 53-dBi EOC gain is chosen. For this reflector, the required e.i.r.p. of 67 to 75 dBW necessitates between 25 and 158 W of RF power for each beam, with a total requirement for the six beams of 150 to 950 W.

In the conventional focal-region-fed approach, a TWT is assumed to have 35-percent efficiency at saturated output power (based on existing space-qualified K_u-band TWTs). If the total output loss from the TWT to the radiating elements (defined as L in Figure 3a) is 4 dB based on a 3-dB predicted loss for the BFN and a 1-dB output multiplexer loss, the resulting RF-to-DC efficiency for all e.i.r.p. levels will be 13.9 percent. This assumes time-division multiple-access (TDMA) traffic using a single carrier in each transponder. Multicarrier operation would require backoff which would significantly reduce the efficiency. The BFN loss is based on values predicted by FACC and TRW for their 20/30-GHz antenna [1], [2]. Both loss estimates are considered to be optimistic, and, depending on the complexity of the system and the number of beams required, total output losses in excess of 4 dB are likely.

The distributed amplifier approach is assumed to use MMIC modules with the characteristics listed in Table 2. This configuration uses a 0.5-W MMIC amplifier module at 15-percent efficiency with a gain of 20 dB at full power. This efficiency is for multicarrier operation with a carrier-to-intermodulation ratio of better than 20 dB. Since the amplifiers are placed directly in front of the radiating elements, as shown in Figure 3b, minimal dissipation of RF power is incurred. For this comparison, a 0.2-dB insertion loss attributable to the MMIC transition is assumed at the output of each amplifier.

TABLE 2. CHARACTERISTICS OF THE PHASE CONTROL AND VARIABLE POWER AMPLIFIER MODULES

CHARACTERISTIC	VARIABLE PHASE CONTROL MODULE	VARIABLE POWER AMPLIFIER MODULE
Frequency (GHz)	17.7–20.2	17.7–20.2
Impedance	50 Ω (nominal)	50 Ω (nominal)
VSWR	Less than 1.3:1	Less than 1.3:1
RF Output Power and Power-Added Efficiency	200 mW at 15%	500 mW at 15% 125 mW at 12% 50 mW at 9% 12.5 mW at 6% 0 mW*
Gain (dB)	16	20 (at full power)
Gain Variation (dB)	1.0 (2.5-GHz band) 0.4 (any 500-MHz bandwidth)	1.0 (2.5-GHz band) 0.4 (any 500-MHz bandwidth)
Phase Shifter:	Time-delay type	
Control	5 bit	
Lowest Bit	11.25°	
Tolerance	±3°	
Response Time (ns)	10	10

* Maximum dissipation = 50 mW.

To produce six beams, three for each polarization, a combiner with 4.8 dB of losses is placed before each amplifier. In this manner, the combining loss will have only a small impact on overall system efficiency, yet each amplifier will be operating with multiple carriers. It is also assumed that the BFN is fabricated in low-loss waveguide, with losses ranging from 1 to 3 dB, based on the required number of elements for the 67- to 75-dBW cases.

Table 3 presents a breakdown for the power efficiencies for three levels of e.i.r.p. The DC-to-RF efficiency is over 14.3 percent for the three cases. This reduction in efficiency from the maximum of 15 percent is attributable to the transition loss and the driver tube. The TWT linear drive power required for each case is less than 1, 2, and 4 W, respectively, well within the range presently achievable.

This comparison shows that phased-array systems with distributed amplifiers can be competitive with conventional approaches in terms of total DC-to-RF efficiencies. It should be emphasized that this conclusion is based on combined output losses in the conventional systems of 4 dB or more and amplifier efficiencies in the distributed amplifier system of 15 percent. As amplifier efficiencies improve, the tradeoff will be even more favorable to the phased-array-fed systems.

TABLE 3. EFFICIENCY OF DISTRIBUTED AMPLIFIER PHASED-ARRAY-FED APPROACH

e.i.r.p. (dBW)	GAIN (dBi)	P_{rad}/BEAM (W)	P_{RF}/MOD (W)	MOD EFFIC (%)	NO. ELEM*	P_{DC}/MOD (W)	P_{DC}/BEAM** (W)	TOTAL EFFIC (%)
67	53	25	0.5	15	52	3.3	173	14.45
71	53	63	0.5	15	132	3.3	439	14.35
75	53	158	0.5	15	330	3.3	1,098	14.39

* Assumes 0.2-dB MMIC transition loss.
** Includes RF drive to BFN (driver efficiency of 35%).

Parameter tradeoffs

Table 2 lists the relevant characteristics of the MMIC modules employed in the subsequent designs which have an important impact on the design and performance of the antenna configuration. In addition to the two modules specified in the table, the existence of a third is assumed, a variable-gain/variable-phase transmit module consisting of a 5-bit phase shifter and a variable 0.5-W amplifier. The variable amplifier consists of a fixed-gain, 0.5-W amplifier with an input five-state attenuator.

The appropriate location of the amplifier/phase-shift module for a viable scanning-beam configuration requires identification. Figure 4 shows two possible amplifier locations. To provide six independent scanning beams, it will be necessary to associate a six-way power combiner with each element,

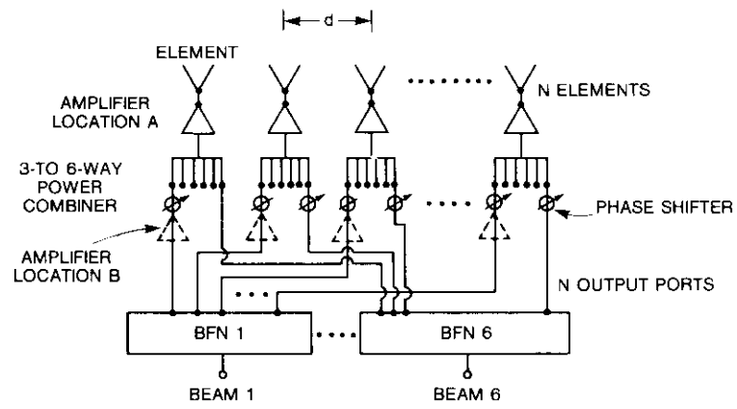

Figure 4. *Possible Amplifier Locations in a Phased-Array BFN*

as shown, implying that all scanning beams would be co-polarized. A more likely arrangement would only have three-way combiners at each orthogonally polarized port of the dual-polarized feed elements.

Each of the six power-combiner ports connects with a BFN which contains the basic N-way power division to distribute the signal to all elements. For amplifier location A, the active module must provide an average total power, P_o, with each of the six carriers (0.2 W/carrier) coexisting in the amplifier. Since this module is operating as a multicarrier, it must provide linear amplification with an acceptable ratio of carrier-to-intermodulation product power of better than 20 dB.

For amplifier location B, the input to each amplifier is a wideband signal. If this is a single carrier, the amplifier can operate close to saturation; however, these inputs are usually multiple carriers and similar backoff restrictions apply. Because the amplifier outputs must be combined via a six-way power combiner, five-sixths of the output power will be dissipated in the isolation resistors that must form a part of the combiner design. Therefore, each module must initially produce 1.2 W just to deliver 0.2 W to the radiators. For a system in which cross-polarized beams are used, two-thirds of the output power will be dissipated in a three-way combiner, which will require each module to produce 0.6 W in order to deliver 0.2 W.

One of the configurations investigated relied on using only the variable-phase control module specified in Table 2. However, use of this module in a configuration such as that shown in Figure 4 presents a dilemma. Since the amplifier and phase shifter sections are an integrated unit, it must be decided which location, A or B, is most appropriate. From a power efficiency viewpoint, the previous discussion has shown that location A is more appropriate. On the other hand, to provide independent scanning control for each beam, the phase shifter must be placed at location B. This particular module is not optimum, as the combiner losses are encountered after amplification. A more optimum design would separate phase shifting and amplifying.

In addition to the limitations imposed on the array design by the amplifier modules, the discrete 5-bit phase-shifting module will impose a limitation on the element size used in the phased array. Two conditions limit element spacing, d, in the phased array: the available phase increment associated with scanning step requirements and the grating lobe appearance in the scanning range. The parameters are defined as follows:

f_1, f_2 = lowest and highest frequency of operation
$\theta_3 = \theta_{BW}$ = 3-dB beamwidth in the main reflector far field
M = magnification factor (confocal paraboloid optics)

K = overlapping ratio of the 3-dB beam contours
$\Delta\theta$ = scanning step in the array far field
ϕ_{inc} = smallest available phase increment, including phase shifter errors
θ_s = scanning range in the main reflector far field

The scanning step, $\Delta\theta$, is given as $\Delta\theta = KM\theta_3$, where K is the overlapping ratio and depends on the array lattice. The scanning step must be greater than or equal to the corresponding step achievable through the minimum phase increment. This leads to $(2\pi d/\lambda) \sin \Delta\theta > \phi_{inc}$, thereby setting a lower limit for the element spacing, d. This expression is valid for small angles of scan from broadside, resulting in

$$\frac{d}{\lambda} \geq \frac{\phi_{inc}}{2\pi \sin KM\theta_3} \quad . \tag{2}$$

The upper limit of element spacing is set by the grating lobe criterion. To have the scanning domain free of grating lobes as the main beam scans the CONUS coverage region requires $2 \sin (M\theta_s) \leq \lambda/d$, which leads to

$$\frac{d}{\lambda} \leq \frac{1}{2 \sin (M\theta_s)} \quad . \tag{3}$$

Equations (2) and (3) give upper and lower bounds on the element spacing. For narrow beams and small scanning angles, the condition for array realizability can be written as

$$\phi_{inc} \leq \frac{180 \sin (KM\theta_3)}{\sin (M\theta_s)} \simeq \frac{180 \sin (K\theta_3)}{\sin \theta_s} \text{ deg} \quad . \tag{4}$$

Since $K\theta_3$ denotes the scanning step and $2\theta_s$ is the total scanning range, equation (4) indicates that for a realizable system, $\phi_{inc} \leq 360/$(number of scanning steps in the scanning range).

For the 5-bit phase-shifter module assumed in Table 2, the smallest phase shift is specified to be 11.25°. Figure 5 is a graphical representation of equations (2) and (3). Parts a and b of the figure are based on an 11.25° increment, a triangular lattice arrangement as shown, and assumed 3-dB beamwidths (θ_3) of 0.3° and 0.4°, respectively. Figure 5 demonstrates the narrow bound imposed on the element size and spacing as a function of the optics magnification. For all the designs subsequently discussed in this paper, element sizes within the constraints of equations (2) and (3) have been used.

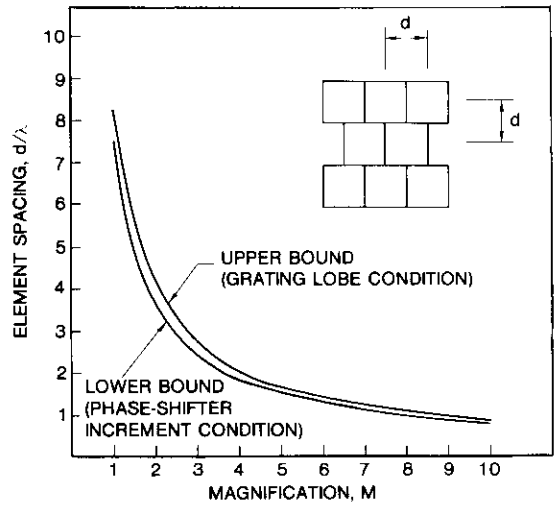

(a) 0.3° Beamwidth and 5-bit Phase Shifter

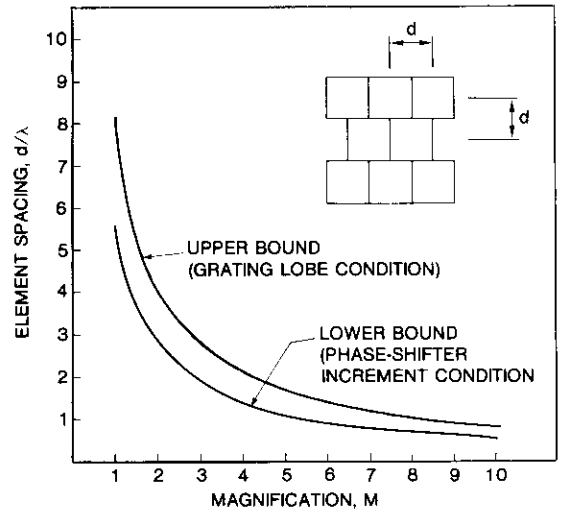

(b) 0.4° Beamwidth and 5-bit Phase Shifter

Figure 5. *Upper and Lower Bounds on Element Spacing*

Phased-array-fed confocal system

An offset near-field Gregorian reflector system with a phased-array feed has been designed for a multiple scanning-beam coverage over CONUS. The key components of this design are the reflector optics, the array configuration, and the BFN. The design of each of these components and system performance are discussed in the following subsections.

Reflector optics

The reflector system used in this application comprises two offset confocal paraboloids which act as a magnifier of a properly placed feed system illuminating the subreflector (Figure 2a). The phased-array feed system is placed so that the subreflector is in its near field and in the vicinity of a conjugate point of the system [4]. The conjugate points in an optical system are defined so that rays originating from one point are transformed by the system into rays that pass through another point. Magnified field distribution of the phased-array aperture is recreated approximately in the main aperture.

The main optical parameters in the design of the confocal reflector system are magnification factor, the ratio of focal length to aperture diameter, array location, and offset height. Selection of each of these parameters is described below.

MAGNIFICATION FACTOR

The magnification factor, M, is defined as

$$M = D_1/D_a = \theta_a/\theta_s \tag{5}$$

where θ_a is the array scan angle corresponding to the main reflector scan angle, θ_s.

It is desirable to have a large M in order to make the phased array physically small. However, a large M means a higher scan loss, a higher sidelobe level, and larger aberrations since the array has to scan to a larger angle ($M\theta_s$). Scan losses for different values of M are shown in Figure 6. The subreflector size and focal length are tied to M through the primary reflector size and focal length. If a small M is used, significantly less beam degradation is achieved, but the subreflector size usually becomes impracticably large for a given primary reflector size. A tradeoff among the various parameters suggests that M lies between 3 and 4 for the present application. The final choice of M is dependent on the phased-array design requirements discussed in the next three subsections.

RATIO OF FOCAL LENGTH TO APERTURE DIAMETER

In a paraboloidal reflector system, the degradation of a scanned beam is determined by the amount of phase aberration, which is proportional to the focal length and inversely proportional to the aperture diameter, D_p, of the parent parabola where $D_p = 2(D_1 + h_1)$. Thus the ratio between the focal

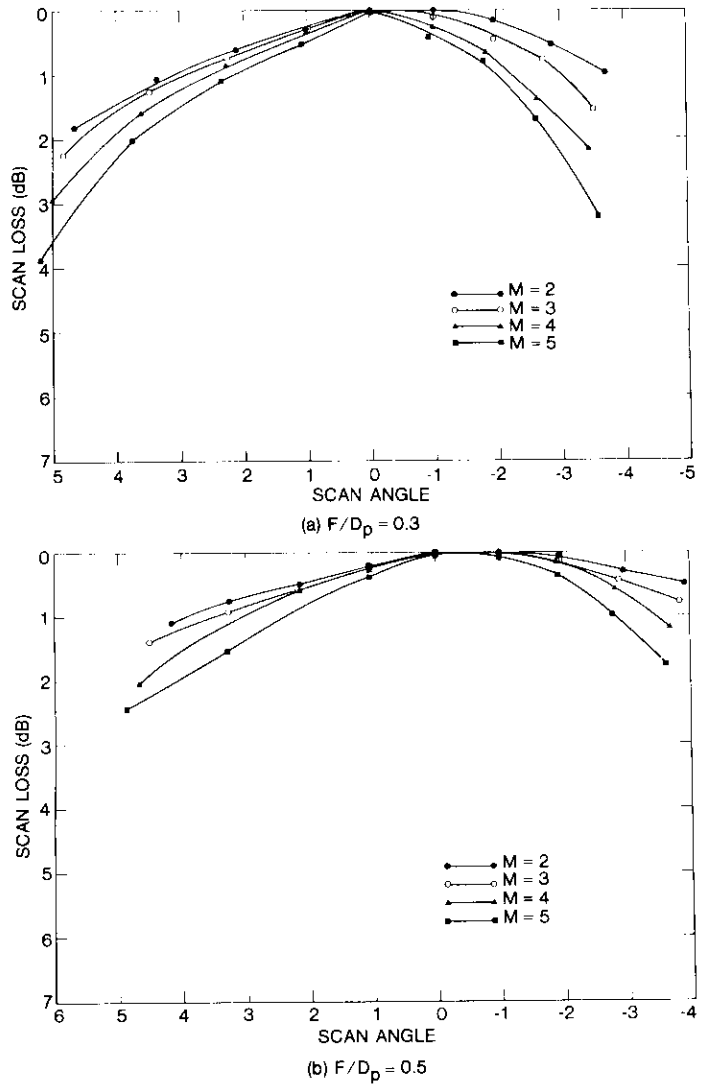

Figure 6. *Scan Loss vs Scan Angle for Confocal Systems*

length and the aperture diameter characterizes the scan performance of a paraboloidal reflector system. As shown in Figure 6, the larger the ratio, the lower the scan loss. However, a large ratio necessitates the use of a large subreflector to minimize spillover. This ratio is also limited by the maximum

available space for the antenna system. A tradeoff between scan loss and antenna size suggests a focal-length-to-aperture-diameter ratio of 0.4.

ARRAY LOCATION

The placement of the array for maximum illumination efficiency is determined by the conjugate points of the system, which are the centers of the main reflector and the array. A good estimate of the array location for limited scan angles can be given by the distance between the array center and the subreflector center

$$L = R_s \frac{M + 1}{M} \tag{6}$$

where R_s is the radial distance from the focal point to the center of the subreflector. The final location of the array is determined by minimizing spillover without blocking the ray paths between the two reflectors.

OFFSET HEIGHT

For parabolic reflector systems, a large offset height produces a high cross-polarized component. Therefore, the lowest offset is chosen for both reflectors which creates no blockage by the array or the subreflector.

The final optical design is determined after the necessary tradeoffs. The various parameters that define the geometry of Figure 2a are listed in Table 4.

TABLE 4. ANTENNA PARAMETERS FOR NEAR-FIELD GREGORIAN SYSTEM

PARAMETER	DIMENSION	PARAMETER	DIMENSION
D_1	271.3 cm	h_a	36.7 cm
F_1	323.5 cm	L	134.6 cm
h_1	133.1 cm	θ_0	45.11°
D_2	134.6 cm	θ_1	23.25°
F_2	91.1 cm	θ_2	64°
h_2	7.4 cm	M	3.6
D_a	76.0 cm		

Phased-array design

The basic parameters in the phased-array design are the element type and shape, total array size, number of elements, lattice arrangement, periodic spacing between the elements, and amplitude and phase distributions. Many of these parameters are interlaced to satisfy certain requirements so that choosing one parameter leads to determining the rest.

A square pyramidal horn is chosen as the array element, lending itself for use in both orthogonal senses of polarization and filling the aperture optimally for highest gain. The taper angle and length of the horn are chosen to produce a uniform phase front at the horn aperture and to eliminate the TM_{12} mode, which would cause the array to be blind at some scan angles.

A primary reflector size of 2.713 m will have an approximate far-field beamwidth of 0.4°. For the phased array, a triangular lattice arrangement is chosen because it offers fewer component beams, with beam overlapping to ensure that no point within CONUS falls outside the 3-dB beamwidth.

The periodic spacing, d, between elements is determined by satisfying the two conditions of equations (2) and (3). A magnification factor, M, of 3.6 is selected which is well within the range of 3 to 4 determined by optical considerations. The grating lobe condition requires that d not exceed a maximum of 2.3λ. If a 5-bit phase shifter is used ($\phi_{inc} = 11.25°$), the minimum value for d is 1.6λ. A 2λ (3.166-cm at band center, 18.95-GHz) square aperture size with a wall thickness of 0.508 mm is chosen for the array element.

For a magnification factor of 3.6 and a main reflector diameter of 2.74 m (9 ft), the approximate size of the array is 76.1 cm in both dimensions. With an element spacing of 3.266 cm, the number of elements in the array is determined to be 576 (24 × 24), as shown in Figure 7. The total array size is 78.38 × 80.03 cm. The elements are arranged in a triangular lattice with a half-element offset between elements in alternate rows. The y-axis is

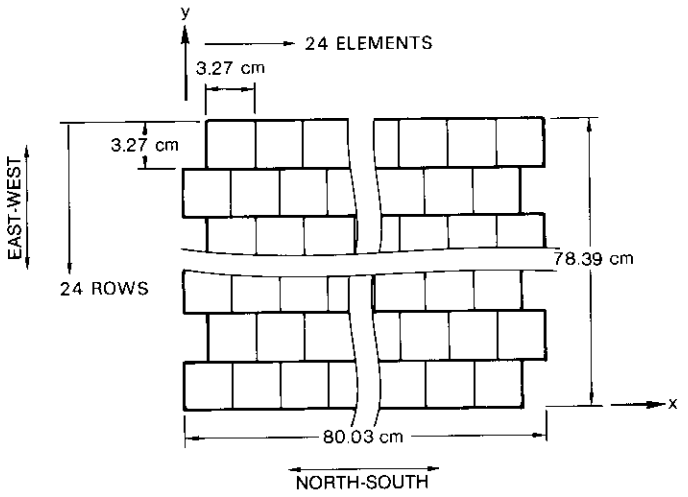

Figure 7. *576-Element Phased-Array Design*

parallel to the offset direction of the dual-reflector system, which is also the east-west axis of the spacecraft.

The 576-element array satisfies the e.i.r.p. requirements with enough margin if the elements are excited uniformly. However, this produces sidelobe levels which are higher than desirable. In order to achieve a co-polarization isolation of 27 dB between the two nearest sectors having the same polarization, an amplitude taper must be introduced. A 30-dB Taylor distribution is used in the east-west direction. In the north-south direction, uniform distribution is maintained since no isolation is needed. The tapered excitation results in lower aperture and power efficiencies. The average power per element using the combined 30-dB Taylor/uniform distribution is about 50 percent of the maximum available power, or 0.25 W. This produces the required e.i.r.p. with co-polarization isolation greater than 27 dB.

Beam-forming network

Six simultaneous scanning beams, one each for the six equal sectors of CONUS, are generated by the BFN shown in Figure 8. Each beam is produced by a 1-input, 576-output power-dividing network (PDN). A low-power, variable-power amplifier (VPA)/variable phase-shifter (VPS) MMIC module is connected at each output of each PDN. The corresponding module outputs of three PDNs are combined and then connected to high-power VPA MMIC modules. The same is done with the other three PDNs. The corresponding VPA outputs are connected to the orthogonal ports of orthomode transducers (OMTs) which feed the array elements. The phase-shifter part of the VPA/VPS modules sets the proper phase gradient for scanning the beam, while the amplifier part sets the 30-dB Taylor distribution.

Performance of the phased-array-fed confocal system

The final design of the complete system of 24 × 24, 2λ waveguide elements was evaluated. Figure 9 shows a number of scanned beams (2-dB contours calculated at 18.95 GHz) generated from an array with a 30-dB Taylor distribution in the east-west direction and uniform distribution in the north-south direction. The various beams show the scanned positions when the element phase shifts are incremented by 11.25°. The angular dimensions of CONUS, as viewed from the satellite, are 6.6° E-W and 3° N-S. The no-scan position of the array is biased 0.15° to the west to make the scan loss almost equal at the east and west extremities, resulting in a scan extreme of 3.15° to the west (scan loss = 1.54 dB) and 3.45° to the east (scan loss = 1.86 dB). Scan step in the far field is 0.25°, which corresponds to 0.9° for the phased array. Figure 9 also shows a cluster of beams around the unscanned position and beams scanned to the northwest, northeast,

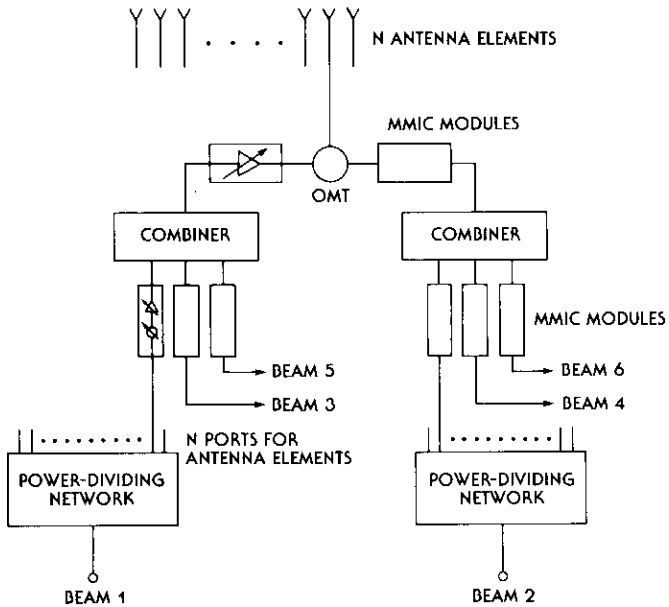

Figure 8. *Feeding Configuration for Full Array With Three-Way Combiners*

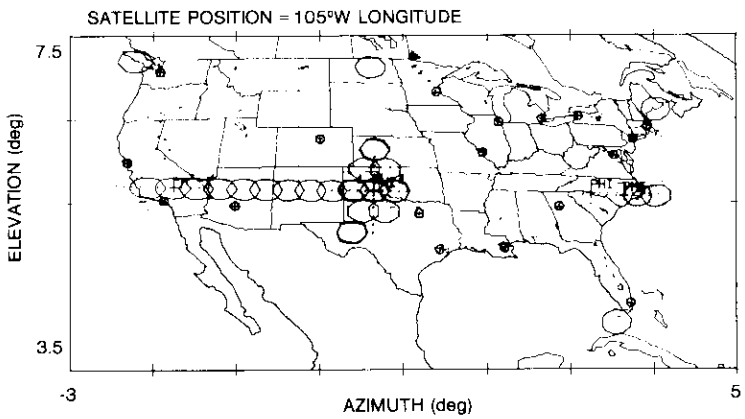

Figure 9. *2-dB Contours of Scanned Beams Over CONUS*

southeast, and extreme north positions. The level of complete contour overlap between three adjacent beams on a triangle is about 2 dB.

Isolation between the two nearest co-polarized sectors is determined by scanning the beam to the edge of the westmost sector and observing the level of sidelobe falling in the other sector. Because both the amplifiers and phase shifters are digitally controlled as outlined in Table 2, only limited quantization levels are used in the calculations. It is observed that the choice of quantization levels of the amplifier outputs could yield the desired co-polarization isolation. Figure 10a shows one case in which a 30-dB Taylor distribution at one set of quantized levels (1, 0.75, 0.5, 0.25, 0) resulted in 27-dB isolation for the worst case (105°W). As shown in Figure 10b, about 33-dB isolation can be achieved with an ideal continuous 30-dB Taylor distribution.

Focal-region-fed Cassegrain system

For the generation of multiple, fixed spot beams, the focal-region-fed Cassegrain system was preferred [5] over the phased-array-fed configuration because of its simplicity in both optical arrangement and feed array design. In a focal-region-fed system, each spot beam corresponds to a feed element or a cluster located in the vicinity of the focal point. By displacing the feed elements, multiple scanned beams can be generated in a straightforward manner. Even though beam degradation due to optical aberration occurs when a feed is defocused, the offset Cassegrain has been proven to perform well for small to medium scanning applications.

Reflector configuration

Figure 2b shows the geometry of the antenna configuration. The main reflector is a parabola and has a circular projected aperture of 271.3 cm, a focal length of 335.28 cm, and an offset height of 142.5 cm. For a reflector with this size, the beamwidth is approximately 0.4° at 20 GHz.

The subreflector is a section of a hyperboloid with a circular projected aperture of 116.8 cm. The focal lengths of the subreflector (114.3 cm and 63.5 cm) result in a magnification factor of 1.8. The offset height is 67.3 cm and the clearance angle is 3.49°. The offset height and the diameter of the subreflector are chosen to minimize the spillover for the maximum scan angle while maintaining a blockage-free configuration.

The subreflector parameters were determined based on a tradeoff study of the magnification factor and the focal lengths of the hyperboloid *vs* antenna gain under the constraint that a blockage-free condition must be maintained. For a hyperbolic subreflector, the magnification M, which is defined as the

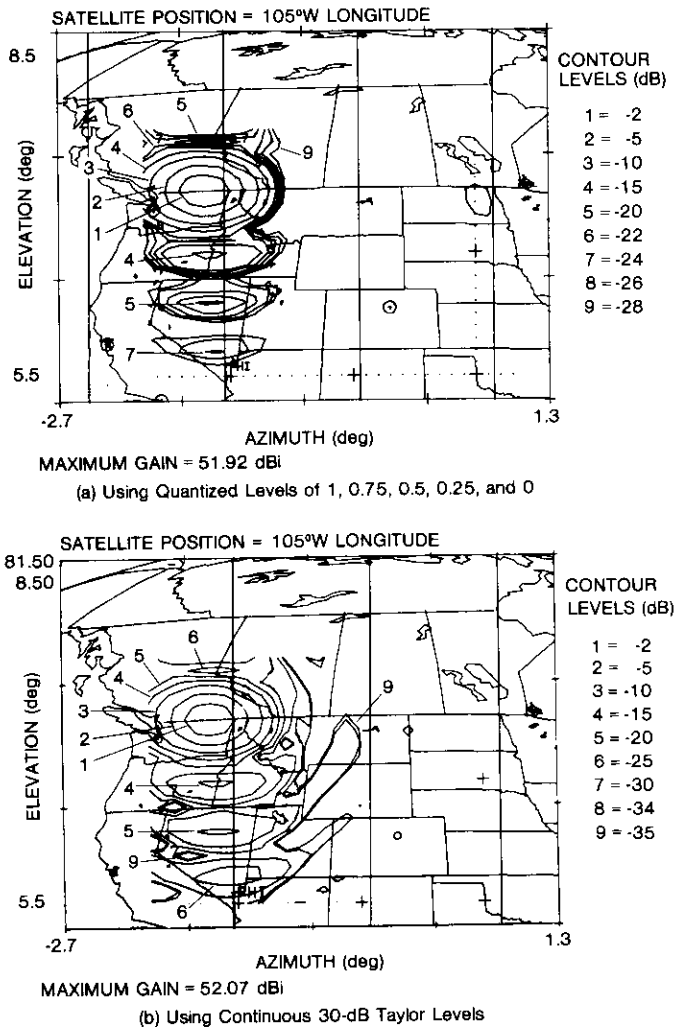

Figure 10. *Sidelobe Isolation for Worst-Case Scanned Beam*

ratio of the longer focal length to the shorter one, is proportional to the curvature of the surface. This proportionality becomes obvious when M is expressed in an alternate form as $M = (e + 1)/(e - 1)$, where e is the eccentricity of the hyperboloid. A large surface curvature causes the reflected energy from the surface to be more spread out than for smaller surface curvature. This greater spread increases the main reflector spillover, especially

for large scanning; therefore, a small to moderate magnification is recommended to reduce scan loss. On the other hand, a small magnification system requires a relatively large subreflector, which may cause blockage problems. By placing the focal points closer to the subreflector (*i.e.*, decreasing F_1), the subreflector size can be reduced while keeping a fixed magnification.

Table 5 summarizes the geometries of the Cassegrain systems with various magnification factors. All the systems have the same main reflector mentioned above. The table reveals that the system with the smallest magnification ($M = 1.5$) has the largest subreflector. On the other hand, the system with the smallest M also has the highest gain at boresight, as indicated in Figure 11. For a small-M system, the spacing between any two horn elements is also reduced (*i.e.*, the size of the horn element is small), resulting in more spillover and less gain. In general, for the same value of F_1, the spacing between two feed elements corresponding to two scanning directions is proportional to the magnification. As a result of the tradeoff study, the final design configuration is chosen from the smallest magnification that offers the highest gain and meets the isolation requirement.

TABLE 5. COMPARISON OF CASSEGRAIN SYSTEMS

M	F_1 (cm)	F_2 (cm)	D_1 (cm)
1.5	106.7	71.1	136.1
1.8	114.3	63.5	120.7
2.0	118.4	59.2	113.5
2.5	127.0	50.8	100.6
3.0	133.4	44.5	91.9

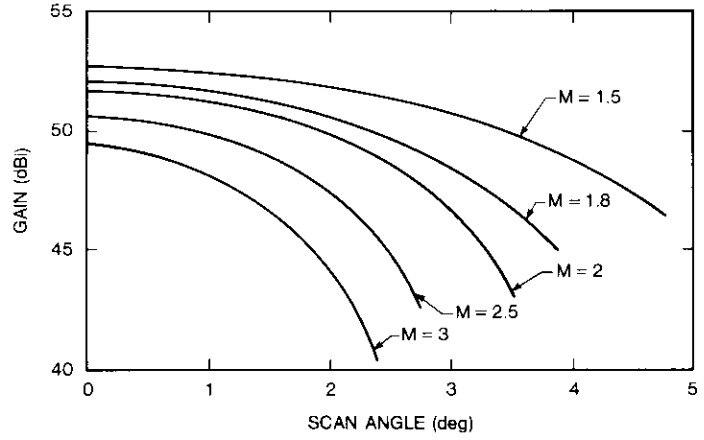

Figure 11. *Scan Curves for Cassegrain Antenna Systems*

Feed-array configuration

In a reflector antenna system, gain and beamwidth performance are normally governed by reflector size. However, feed design is essential to sidelobe control and beam shaping to meet optimal coverage and beam isolation requirements. For the fixed spot-beam application, the Boston, New York City, and Washington, D.C., region has the most stringent isolation requirements because the separation between the two cities sharing the same polarization is very small. In order to obtain good isolation between any two co-polarized beams, instead of single feed elements a cluster feed is used to generate each spot beam, offering the freedom to adjust the power distribution of the component beams and thus control the sidelobe levels and increase isolation. Furthermore, because these three cities are so close together, horn sharing must be utilized between the elements in different clusters to maximize the feed cluster aperture.

In general, a higher peak gain can be achieved in a reflector system fed by a square horn than in one fed by a circular horn with the same dimension. It can be shown that the gain for a square-horn-fed system is approximately 0.5 dB higher than that for a circular-horn-fed system for a wide range of horn sizes. In addition, a square-horn cluster allows finer aperture distribution control because of the greater number of horn elements in a cluster. Therefore, for linear polarization applications, it is advantageous to use square or rectangular horns, either as individual feed elements or as clusters.

As shown in Figure 12, the cluster design using square horns consists of nine elements with the same aperture size and overlapping clusters. Four

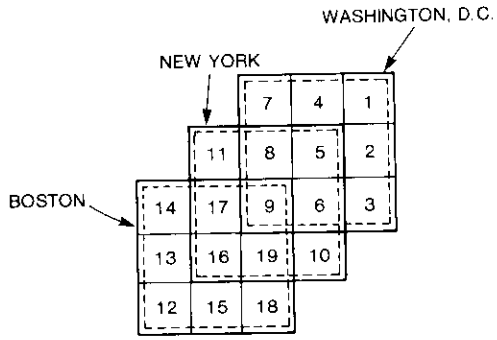

Figure 12. *Feed Cluster Design for Boston, New York City, and Washington, D.C., Fixed Spot Beams*

horns are shared by two adjacent clusters and one horn by all three clusters, maximizing the horn aperture size and consequently improving both gain and beam isolation. Since the New York beam uses orthogonal polarization, the horn shared by these three clusters must transmit one signal with one polarization and two signals with the orthogonal polarization.

Antenna performance

To demonstrate the validity of the antenna design, the contour patterns of certain cities are calculated. In computing these scanned beams, the boresight of the antenna is located at Oklahoma, or more precisely, 0.99° east and 5.65° north of the subsatellite point of a satellite at 105° west longitude. The boresight was chosen to minimize the amount of scanning for these beams while ensuring that the spot beams on the West Coast achieve the same level of isolation. Consequently, the San Francisco beam was also calculated, in addition to the three most critical beams on the East Coast, to demonstrate the antenna performance on the West Coast. All patterns are calculated at the midband frequency of 18.95 GHz.

Figure 13 shows the co-polarization patterns for the Boston, New York City, and Washington, D.C., coverages. As seen from the contour patterns, all three beams meet or exceed 30-dB isolation from the adjacent cities employing the same sense of polarization. The coefficients used to optimize these beams are quantized in accordance with the gain level specification of the VPA module and the phase-step increment of the VPS. Table 6 lists the coefficients for these three beams, and Table 7 shows the performance achieved by this design for the three East Coast cities, as well as for San Francisco.

Prototype array element

To demonstrate the feasibility of the phased-array design mentioned in previous sections, the phased-array element shown in Figure 14 was built and tested. The element comprises several key components, including the radiating element (a square horn), an OMT, and a rectangular-waveguide-to-MMIC transition. Array performance was demonstrated using a scaled K_u-band version upon which extensive measurements were made [5].

Square-horn radiating element

As pointed out, the square aperture dimensions of the horn are limited by the phase-shifter increment and the grating lobe locations in the array pattern. An aperture dimension of 2λ at band center (18.95 GHz) satisfies these requirements. The horn taper is determined by the mode content requirements and allowable phase errors at the horn aperture. The mode content contributes

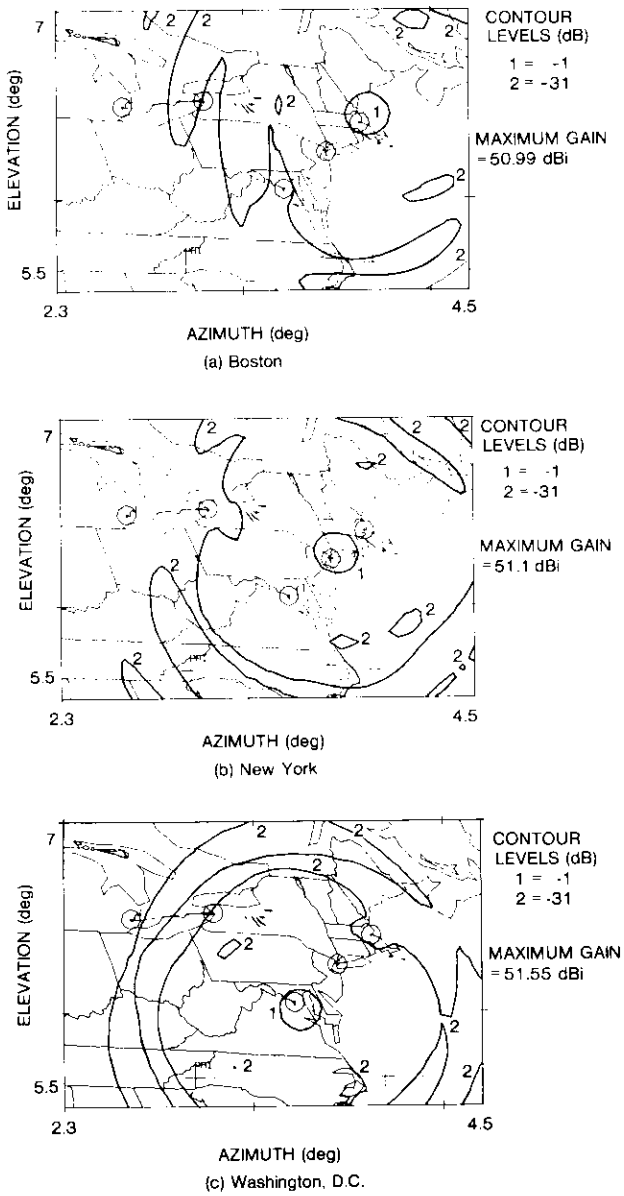

Figure 13. *Fixed Spot Beam Over Boston, New York City, and Washington, D.C. (satellite position = longitude 105°W)*

TABLE 6. COEFFICIENTS FOR WASHINGTON, D.C., NEW YORK CITY, AND BOSTON BEAMS

COMPONENT BEAM NUMBER	WASHINGTON, D.C.		NEW YORK CITY		BOSTON	
	AMPLITUDE	PHASE	AMPLITUDE	PHASE	AMPLITUDE	PHASE
1	0	0				
2	0.32	56.25				
3	0.16	33.75				
4	0.5	0				
5	1.0	0	0.32	180		
6	0	0	0.32	67.5		
7	0.32	0				
8	0.32	−56.25	0.32	90		
9	0.32	−45	1.0	0	0.32	−135
10			0.32	22.5		
11			0.32	0		
12					0	0
13					0	0
14					0.16	0
15					0.32	45
16			0.5	−11.25	1.0	45
17			0.5	−11.25	0.5	11.25
18					0.5	−101.25
19			0.32	22.5	0.32	−78.75

TABLE 7. ANTENNA PERFORMANCE AT SELECTED CITIES

CITY	e.i.r.p.	EDGE GAIN	CROSS-POLARIZATION	ISOLATION*
Washington, D.C.	50.33	50.6	37	30
New York	50.02	50.2	37	32
Boston	49.91	50.1	36	30
San Francisco	48.96	49.2	44	32

* Sidelobe level at the closest co-polarization city.

to the existence of blind spots in the array pattern, but these can be eliminated if the horn taper and length are chosen to effectively short-circuit the TM_{12} mode at the aperture [6].

Orthomode transducer

An OMT is used to feed the radiating element with dual polarization. The two perpendicularly polarized signals are fed through the shunt and the back (or through) ports of the OMT. Both input ports have standard rectangular

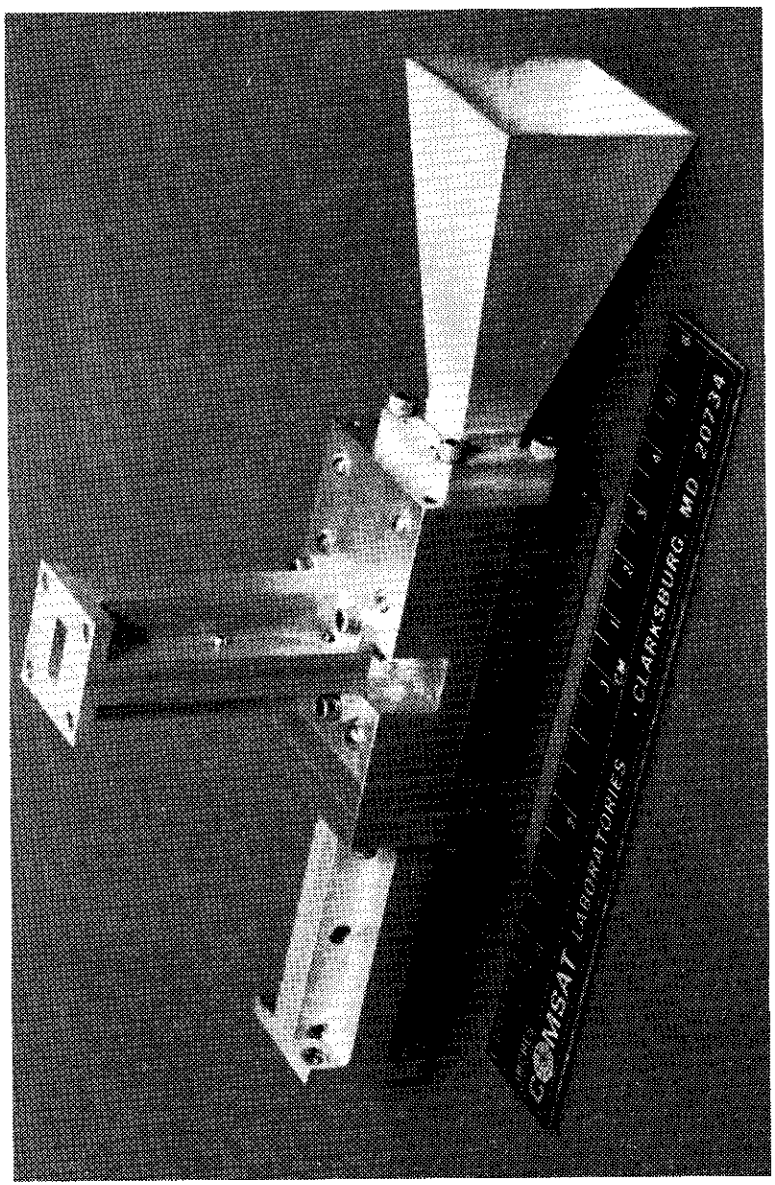

Figure 14. *Complete Breadboard Model of Array Element*

waveguide cross sections. The back port is matched to the square cross section of the OMT through a two-section, quarter-wavelength transformer. The measured performance of the fabricated OMT shows a return loss of more than 20 dB, port-to-port isolation exceeding 45 dB, and an insertion loss of about 0.08 dB across the full band of 17.7 to 20.2 GHz.

MMIC-to-waveguide transition

The MMIC-to-waveguide transition is a critical element in systems that use distributed power and phase control, since energy must be efficiently transitioned in and out of the MMIC circuit. Two techniques for such transitions exist in the literature: one using a ridged waveguide transformer [7] and the other an antipodal finline transition [8]. The ridged waveguide technique has the advantages of low loss and broad bandwidth but suffers from a complex mechanical structure and difficult assembly. The antipodal finline structure is also broadband and low loss but does not allow easy access to ground. Both have the additional drawback of allowing transmission in only one of the two possible orthogonal modes.

In the new MMIC-to-waveguide transition designed for the present application, the MMIC circuit is mounted on a dielectric (beryllia) substrate which includes matching and bias circuits. The substrate assembly is mounted in the E-plane of the rectangular waveguide section. Two orthogonal transition circuits can be mounted in a square waveguide to provide dual polarization operation. Mode isolation in this case depends on control of the mechanical and physical parameters of the structure.

The printed circuit on the dielectric substrate is divided into three subcircuits, as shown in Figure 15: a unilateral finline transition from waveguide to slot line delineated by the sections labeled 1 through 4 in the figure, a balun to convert the balanced slot-line mode to the unbalanced microstrip or coplanar waveguide (CPW) on the MMIC, and the MMIC circuit which is either soldered or epoxied onto the surface of the substrate.

Figure 16 shows a disassembled rectangular waveguide transition. The measured performance of this transition is shown in Figure 17. The insertion loss is approximately 1 dB over the 18.5- to 19.5-GHz range. This includes 0.4 dB for the 50-Ω line which is inserted to simulate the MMIC module, plus the input and output transitions which are 0.3 dB each. The return loss over this same range is better than 15 dB and is about 25 dB at 19 GHz. The isolation between input and output was measured by removing the input and output ribbons. The resulting coupling, −30 dB, is caused primarily by leakage through the waveguide beyond cutoff in the vicinity of the 50-Ω microstrip line. It should be mentioned that the bandwidth restrictions of the

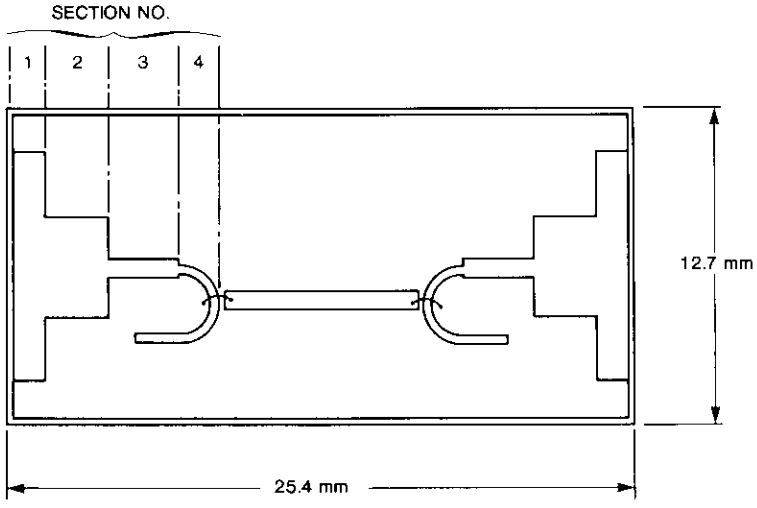

Figure 15. *Circuit of MMIC/Waveguide Transition*

transition are dictated by the stepped transformer sections in the circuit used to match the 50-Ω line to the waveguide impedance. A continuously tapered transformer design may increase the bandwidth to nearly the full 2.5 GHz.

Phased-array element

The complete phased-array element consists of the radiating horn fed by the OMT, which in turn is fed through the two orthogonal ports via waveguide sections containing the MMIC amplifier modules. Assembly of the horn, the OMT, and two transitions results in the phased-array element shown in Figure 14.

The overall performance of this breadboard element was measured. The return losses, port-to-port isolation, and insertion losses are shown in Figure 18. Because of the limitations of the MMIC/waveguide transitions, the bandwidth of the whole phased-array element is reduced to about 1 GHz for a return loss of better than 15 dB. The port-to-port isolation is higher than 47 dB across the full band. However, the insertion loss without the radiating horn is about 1.1 dB across a 1-GHz bandwidth. This loss reflects mainly the 50-Ω line loss inside the transition, as pointed out earlier.

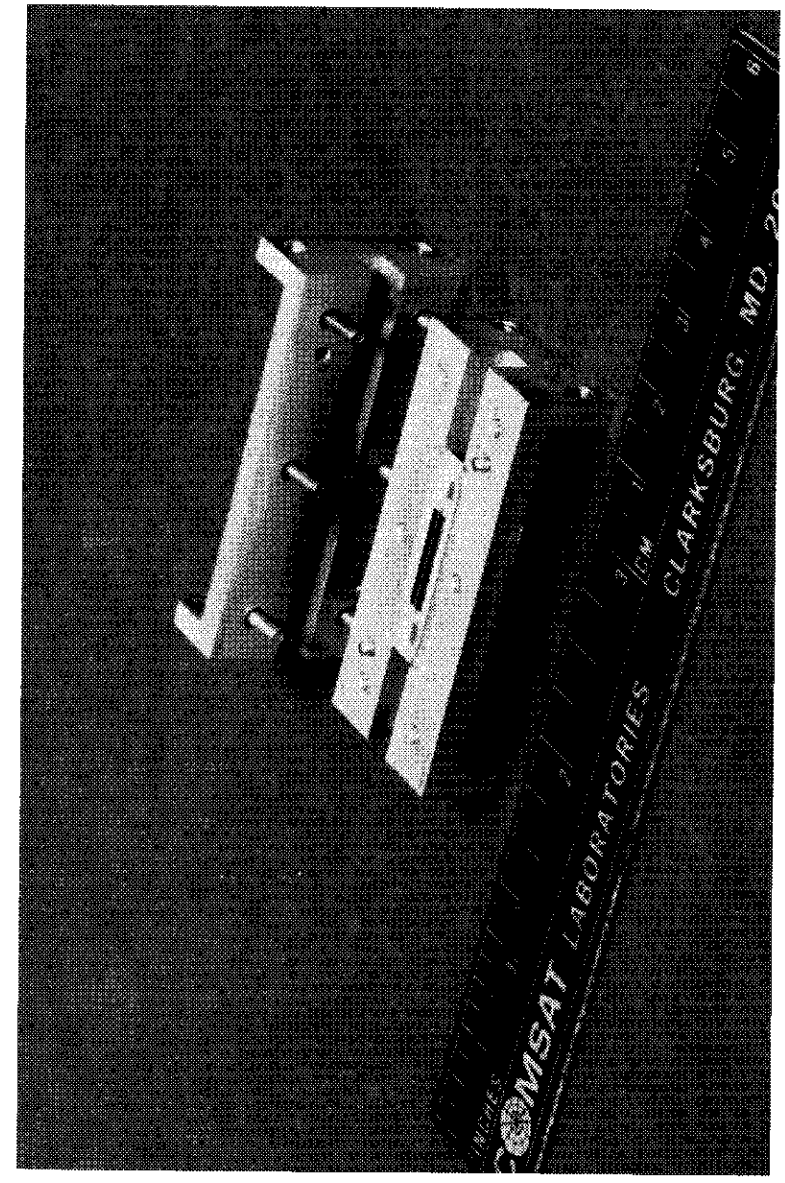

Figure 16. *MMIC/Waveguide Transition (disassembled)*

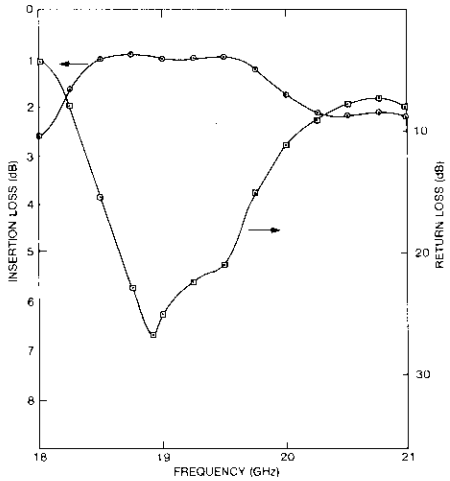

(a) Insertion Loss and Return Loss

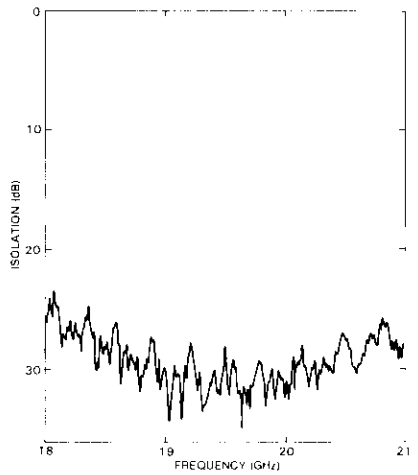

(b) Isolation

Figure 17. *Measured Performance of MMIC/Waveguide Transition*

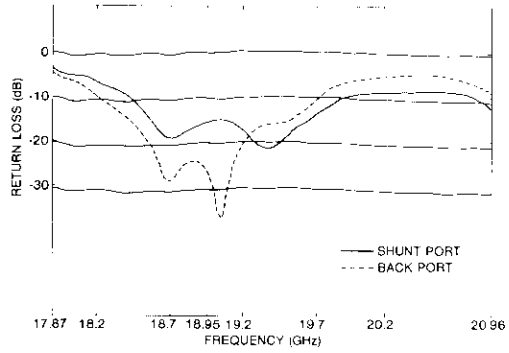

(a) Return Loss

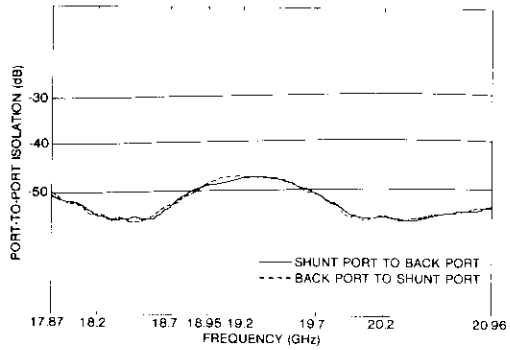

(b) Port-to-Port Isolation

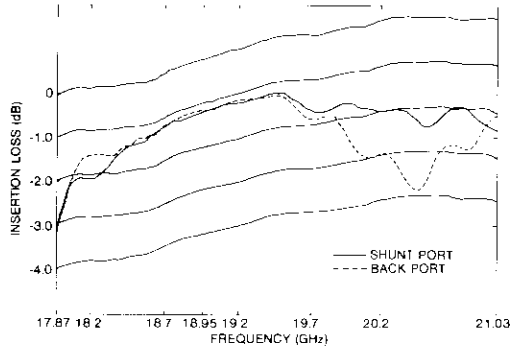

(c) Insertion Loss of OMT-MMIC/Waveguide Transition

Figure 18. *Measured Performance of Breadboard Array Element*

Conclusions

The results presented in this paper substantiate, both by analysis and hardware demonstration, the feasibility of phased-array-fed dual-reflector systems with distributed power and phase control. The conclusions drawn from this study are based on a detailed examination of multiple scanning spot-beam and multiple fixed spot-beam designs.

The multiple scanning beam antenna design that was developed utilizes a 576-element phased array. It provides six simultaneous scanning beams and, with an appropriately sized main reflector, is capable of meeting high isolation and e.i.r.p. requirements.

For multiple fixed spot-beam configurations, the 576-element phased-array-fed design was considered in addition to a more conventional focal-region-fed Cassegrain system which utilized nine-horn clusters to generate the fixed beams. With an appropriately sized main reflector, both designs were capable of meeting the isolation and e.i.r.p. requirements. The Cassegrain design, which used an undersized 2.76-m (9-ft) reflector, was preferred for the multiple fixed spot-beam configuration and was still able to achieve 30 dB of co-polarization and cross-polarization isolation between Boston and Washington, D.C., by optimizing the feed element, feed locations, and excitations. This configuration also used a relatively simple BFN compared to the complexity of the corporate-fed configuration for 18 fixed beams.

Several key hardware elements were designed, built, and tested during this study. One was a waveguide-to-MMIC transition, a critical element in systems that use distributed power and phase control since energy must be transitioned into and out of the MMIC circuit efficiently. The new design showed good performance over a 1-GHz bandwidth with a maximum insertion loss of 0.3 dB.

A phased-array element incorporating the waveguide-to-MMIC transition was also fabricated. It consisted of a square pyramidal horn, an OMT, and two rectangular waveguide-to-MMIC transitions. For the dual-polarized element, the rectangular waveguide transitions are connected to the two arms of an OMT that feeds the radiating horn. Cross-polarization isolation is also provided through the OMT. Measurements of return loss, insertion loss, and isolation all showed good results.

In conclusion, this study has demonstrated the performance achievable using an array-fed, multibeam, dual-reflector system. The results obtained reveal the advantages of using distributed power and phase control via MMIC modules, as compared to conventional systems, when high efficiency, high e.i.r.p., and rapidly scanned multiple beams are required.

Acknowledgments

The work presented in this paper was performed under Contract NAS3-23250 with NASA Lewis Research Center, Cleveland, Ohio. The authors would like to acknowledge the efforts of J. Smetana of NASA, with whom they had many helpful discussions.

References

[1] "30/20 GHz Spacecraft Multiple Beam Antenna System," Ford Aerospace Report for NASA Contract NAS3-22498, 1982.

[2] "30/20 GHz Spacecraft Multiple Beam Antenna System," TRW Report for NASA Contract NAS3-22499, 1982.

[3] D. F. DiFonzo, "The Evolution of Communications Satellite Antennas," IEEE International Symposium on Antennas and Propagation, Albuquerque, New Mexico, May 1982, *Digest*, Vol. 1, pp. 358–361.

[4] C. Dragone and M. J. Gans, "Imaging Reflector Arrangements to Form a Scanning Beam Using a Small Array," *Bell System Technical Journal*, Vol. 58, No. 2, February 1979, pp. 501–515.

[5] R. Sorbello *et al.*, "Phased-Array-Fed Antenna Configuration Study, Volume II: Final Report," COMSAT Laboratories Report for NASA Contract NAS3-23250, Report CR 168232, October 1983.

[6] N. Amitay and M. J. Gans, "Design of Rectangular Horn Arrays With Oversized Aperture Elements," *IEEE Transactions on Antennas and Propagation*, Vol. AP-29, No. 6, November 1981, pp. 871–884.

[7] M. V. Schneider, B. Glance, and W. F. Bodtmann, "Microwave and Millimeter Wave Hybrid Integrated Circuits for Radio Systems," *Bell Systems Technical Journal*, Vol. 46, No. 6, July–August 1967, pp. 1703–1726.

[8] J. H. C. Van Heuven, "A New Integrated Waveguide-Microstrip Transition," *IEEE Transactions on Microwave Theory and Techniques*, Vol. MTT-24, No. 3, March 1976, pp. 144–146.

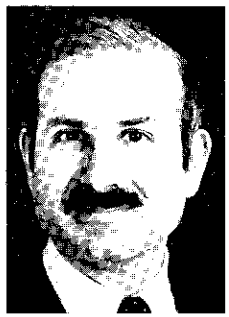

Robert M. Sorbello received a B.E.E. from Manhattan College in 1969 and an S.M. and Ph.D. in Applied Physics from Harvard University in 1973 and 1976, respectively. From 1976 to 1978 he was with Hughes Aircraft Company, where he worked on phased-array and frequency-scanning antennas for airborne radar systems. He also developed X-band MIC PIN-diode-controlled switching circuits. In 1978, he joined COMSAT Laboratories as a Member of the Technical Staff in the Antennas Department of the Microwave Laboratory, and subsequently in 1981 became Manager of the Satellite Antennas Department of the Microwave Technology Division. At COMSAT, he has worked on the design of multibeam and reconfigurable satellite antenna systems and has developed K_a-band MIC phase shifters and VPDs, a high-power C-band contiguous channel multiplexer for earth station applications, space-qualified 12/17-GHz feeds for DBS, and broadband printed-circuit elements and arrays. In his present managerial role, he directs and carries out research and development in the areas of reflector optics, phased arrays, beam-forming networks, feed elements, and associated technologies for communications satellites. Dr. Sorbello is a member of IEEE, Tau Beta Pi, and Eta Kappa Nu.

Amir I. Zaghloul received a B.Sc. from Cairo University, Egypt, in 1965, and an M.A.Sc. and Ph.D. from the University of Waterloo, Canada, in 1970 and 1973, respectively, all in Electrical Engineering. Prior to joining COMSAT Laboratories in 1978, he held faculty positions at the Universities of Waterloo and Toronto, in Canada, and at Aalborg University in Denmark. At COMSAT Laboratories, he has been a member of the Microwave Systems Department and the Satellite Antennas Department, where he is presently a Staff Scientist. His responsibilities have included design and development of microwave integrated circuits, microwave switch matrixes for SS-TDMA systems, multibeam antennas, phased-array systems, microstrip antennas, and reflector antenna systems. He has also been involved in study and support efforts for several satellite programs, including INTELSAT, INMARSAT, ARABSAT, PALAPA, and SATCOL. Dr. Zaghloul is a Senior Member of IEEE, and Chairman of the Washington, D.C., Chapter of the Antennas and Propagation Society for 1985–1986. He is the recipient of the 1986 H. A. Wheeler Applications Prize Award for best applications paper in IEEE Transactions on Antennas and Propagation.

Shu Hong (Bryan) Lee received a B.S. in Electrical Engineering from National Taiwan University, Taipei, in 1973 and an M.S. and Ph.D. in Electrical Engineering from Ohio State University in 1977 and 1980, respectively. While at Ohio State, he was a graduate research assistant in the Electroscience Laboratory. In 1980 he joined COMSAT Laboratories, where he has been involved in the design and analysis of reflector antenna systems for satellite applications. Since September 1986, Dr. Lee has been with INTELSAT, El Segundo, California.

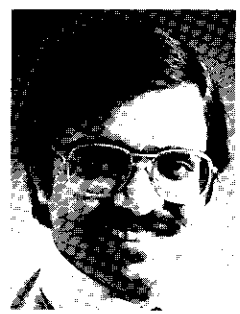

Shakeel Siddiqi received a B. Tech. from the Indian Institute of Technology, Kanpur, an M.S.E.E. from the Polytechnic Institute of New York, and has completed his Ph.D. course requirements. He is a Member of the Technical Staff in the Satellite Antennas Department at COMSAT Laboratories, where his principal activities involve the analysis, design, and implementation of satellite antennas and related components. He has been involved in such satellite programs as DBS and INTELSAT VI. He was also involved in the NASA 20/30-GHz antenna study. Currently, he is developing an MMIC phase shifter for an active phased-array antenna. Prior to joining COMSAT in 1981, Mr. Siddiqi was with the Government Systems Division of General Instrument Corporation, where his work on ESM and ECM systems culminated in the invention of a reduced-size spiral and an extremely low-backlobe spiral antenna. He is a member of IEEE.

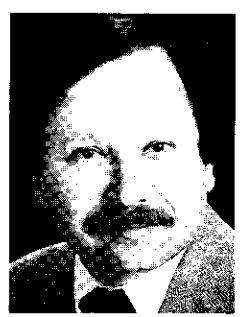

Bernard D. Geller received a B.S. in Electrical Engineering from the Johns Hopkins University in 1967, and an M.S.E.E. from the University of Maryland in 1974. From 1967 to 1979, he was involved in the development of both passive and active microwave and millimeter-wave circuits at the Westinghouse Advanced Technology Laboratory in Baltimore, Maryland. After a short period at Fairchild Space and Electronics Company during which he designed satellite earth station components, he joined COMSAT Laboratories in November 1979. He is currently Manager of the Microwave Circuits Department, and has been involved with the design of monolithic microwave integrated circuits (MMICs) and other advanced MICs. He is a Senior Member of IEEE.

A comparison of three MAC TV transmission formats

L. C. PALMER

(Manuscript received June 5, 1985)

Abstract

Three multiplexed analog component (MAC) television formats are compared by analysis and computer simulation to evaluate FM TV transmission performance over satellite channels. The three formats use different luminance/chrominance compression ratios of 5:4/3.75:1, 4:3/4:1, and 3:2/3:1. Analytical models are developed to predict luminance, color-difference, and color-component signal-to-noise ratios (*S/N*s) in the presence of thermal noise. Distortion due to filter truncation is predicted on the basis of simulated RF spectral distributions for different values of the peak-frequency deviation. Full-channel simulations resulted in reasonable agreement between the predicted and simulated *S/N* values.

Predicted differences between systems are small and within the accuracy range of laboratory measurements. Although final conclusions must be based on subjective testing, the work was useful in identifying the sources of transmission impairments and the tradeoffs among various transmission parameters.

Introduction

The multiplexed analog component (MAC) transmission format has been a candidate for use in television transmission by satellite since the concept was proposed in the early 1980s [1]–[5]. This technique offers the potential of higher picture quality—primarily due to freedom from the artifacts inherent in the National Television System Committee (NTSC) format with its color

subcarrier—as well as the possibility of improved performance at or near threshold and increased tolerance to the over-deviation as routinely utilized for transmission of TV signals by satellite. The intermediate digital stage of signal processing makes the format well suited to secure scrambling techniques and permits the inclusion of multiple high-quality audio and data channels. In addition, this technique fits easily into a variety of enhanced TV transmission formats, including those which increase the perceived definition and/or allow for changes in the aspect ratio of the TV picture. For these reasons, the MAC format remains of considerable interest for TV transmission by satellite; hardware development, testing and experimentation, and standards formulation continue to be active areas of investigation [6]–[22].

This paper compares the relative performance of three MAC [4] formats for conventional 525-line, 60-Hz TV transmission via satellite. The three formats are similar in that luminance and alternate R-Y and B-Y color-difference signals are compressed and inserted into a time-multiplexed format during each scan line. The formats differ in the choice of compression ratios for the luminance and color-difference signals (luminance compression ratios of 5:4, 4:3, and 3:2 with corresponding chrominance ratios of 3.75:1, 4:1, and 3:1).* Analysis and simulation are used to compare the relative performance of the luminance and chrominance channels of the three systems, which trade off signal-to-noise ratios (S/Ns) between components through the selection of compression ratios.

Estimates are obtained for output S/Ns or signal-to-noise-plus-distortion [$S/(N + D)$] ratios based on the transmission of relatively simple color-bar and multiburst test patterns. Output signal-to-thermal-noise ratios are derived using an analytical model and other sources of impairment are investigated using a software simulation model [23]. Although limited in their applicability to actual picture information, the results give insight into the sources of performance degradation experienced when the MAC format is transmitted over the bandwidth-limited satellite channel. The results also allow the three systems to be compared on a relative basis, although final conclusions must await side-by-side subjective testing.

* These choices of compression ratios correspond generically to systems considered by several organizations during 1983–1984. The 4:3/4:1 system is an N-MAC prototype developed at COMSAT Laboratories for Satellite Television Corporation during that period. The 5:4/3.75:1 system corresponds to the time-multiplexed components system developed by CBS [6]. The 3:2/3:1 system embodies the compression ratios used in the C-MAC [2], D/2-MAC [21], and B-MAC [10] systems, developed respectively by the Independent Broadcasting Authority, Telediffusion de France and others, and Scientific Atlanta/DVS.

This work indicates that the objective (calculated or simulated) S/Ns of the three systems examined differ very little, and all are highly dependent on the parameters and assumptions used in the models. These variables include: the luminance filter, the chrominance filter used at the transmitter and the receiver, the pre-emphasis/de-emphasis network used, the definition used for 75-percent color bars, and the scaling of transmitted luminance and color-difference signals used prior to selecting the peak frequency deviation of the transmitter.

Analytical model for TV transmission

One measurement used to evaluate television transmission formats is output S/N, which represents the relative amount of noise and distortion in the received picture. For high-quality television transmission, weighted output S/N in the region of 40, 50, or even 60 dB is required, depending on the disposition of the material (for example, if it is intended for direct viewing or for rebroadcasting).

Output S/N is also an important measure in evaluating different MAC formats and in comparing MAC to the conventional NTSC format. Some of the definitions and conventions established for composite signal NTSC performance can be applied to the MAC format. However, new definitions and standards are needed in certain areas. For example, because the MAC luminance and color-difference components are easily separable, it is straightforward to compute separate luminance and chrominance S/Ns. This separation is not made with the NTSC format, and evaluation is based on a composite S/N. For the MAC format, separate luminance and chrominance S/N calculations illustrate the tradeoffs available in MAC by using different compression ratios and post-detection filtering for the two components, hence achieving different output S/Ns for the luminance and chrominance.

With component systems, the trend is to decompose the signal still further into its three primary colors, red, green, and blue (R, G, and B) as monitors become available to accept such inputs. This decomposition leads to a more basic input/output transmission model resulting in three output S/Ns, one for each of the primary colors. These three ratios are used here only for relative comparison. The use of R, G, and B S/Ns is somewhat controversial, and new standards, test procedures, facilities, and particularly subjective testing are needed in this area.

A review of S/N definitions for NTSC

Definitions for output S/N of the NTSC format are reviewed briefly, first without pre-emphasis/de-emphasis and subjective weighting and then with these two modifications.

OUTPUT S/N WITHOUT PRE/DE-EMPHASIS AND SUBJECTIVE WEIGHTING

For the conventional NTSC format, output S/N is defined as [24]

$$S/N = \frac{1}{2}\frac{[V_{pk-pk}]^2}{\text{mean square error}} \quad . \tag{1}$$

The NTSC peak-to-peak voltage includes the synchronization pulse at a level of -40 IRE units so that $V_{pk\text{-}pk} = 140/100\ V_{pk\text{-}pk}$ (luminance only) $\approx \sqrt{2}\ V_{pk\text{-}pk}$ (luminance only) and

$$S/N = \frac{[V_{pk-pk}\,(\text{luminance})]^2}{\text{mean square error}} \quad . \tag{2}$$

Similar definitions remain to be established for the MAC format.

Output S/N for the NTSC format is defined in terms of the peak-to-peak luminance voltage divided by the mean square noise at the output of the cascade of FM demodulator, de-emphasis network, and subjective weighting filter. The back-to-back TV transmission channel can be modeled, as shown in Figure 1, by ideal voltage-to-frequency conversion at the transmitter, thermal noise addition, and ideal frequency-to-voltage conversion at the receiver. The black-to-white luminance transition at the output of the demodulator can be equated directly to $\sqrt{2}\Delta F_{pk}$, where ΔF_{pk} is the peak frequency deviation of the transmitter, so that the "signal" term in equation (2) is $[V_{pk\text{-}pk}\,(\text{luminance})]^2 = 2\Delta F_{pk}^2$.

The power spectral density of the noise out of the ideal FM demodulator is shown at the right of Figure 1. The noise power at the output of the FM demodulator with bandwidth f_m [equivalent to mean square error, $\overline{\epsilon^2}$, in equation (2)] is $\overline{\epsilon^2} = (N_o/C)(f_m^3/3)$, whereby

$$S/N = 6\left(\frac{\Delta F_{pk}}{f_m}\right)^2 \frac{C}{N_o}\frac{1}{f_m} \tag{3}$$

where $(\Delta F_{pk}/f_m)$ = ratio of peak frequency deviation to highest baseband frequency (usually referred to as the modulation index)

C/N_o = carrier power-to-noise density ratio at the input to the FM demodulator

f_m = maximum baseband frequency of the modulating signal.

OUTPUT S/N WITH PRE/DE-EMPHASIS AND SUBJECTIVE WEIGHTING

Pre-emphasis introduces variable gain vs frequency, which is compensated for at the receiver with a matching de-emphasis network. Received noise is

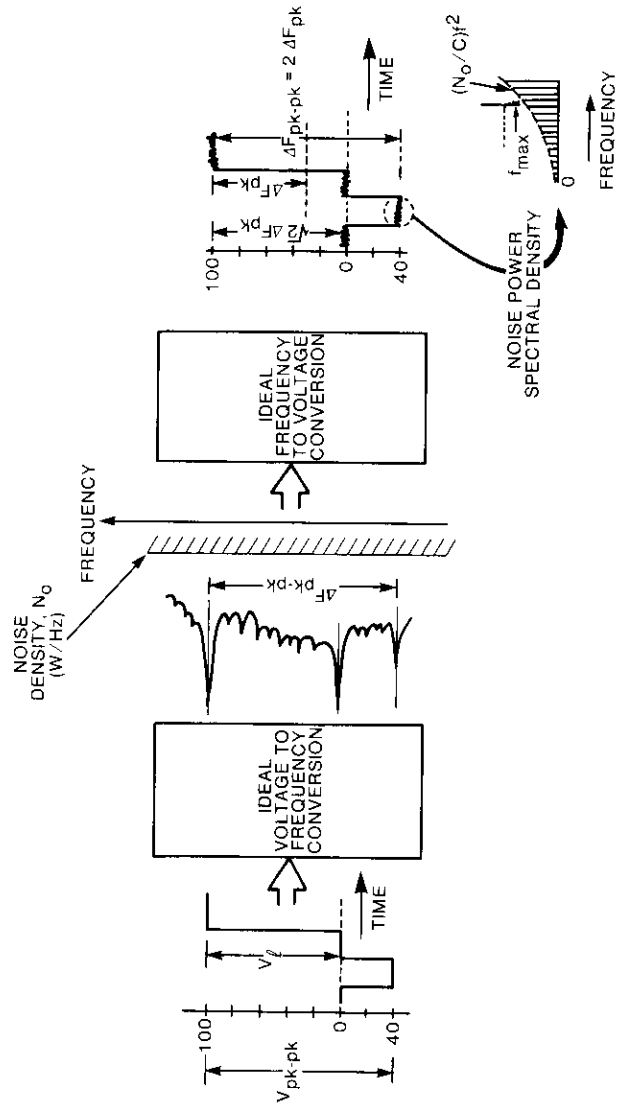

Figure 1. *Definitions for NTSC Output S/N (no pre/de-emphasis or subjective weighting)*

also operated on by this de-emphasis network, reducing its mean square value. To account for the de-emphasis function with transfer function* $D(f)$, the mean square error calculation is modified to give

$$\overline{\epsilon_D^2} = \frac{N_o}{C}\int_0^{f_m} f^2 D(f)\, df \quad . \tag{4}$$

Additional weighting can be applied to the integration of the noise power to account for the subjective effect of noise in different frequency bands on human observers [25]. Applying the subjective weighting curve, $W(f)$, yields the weighted noise

$$\overline{\epsilon_{DW}^2} = \frac{N_o}{C}\int_0^{f_m} f^2 D(f)\, W(f)\, df \quad . \tag{5}$$

Comparing the mean square error $\overline{\epsilon^2}$ to $\overline{\epsilon_{DW}^2}$ gives a de-emphasis plus subjective weighting improvement, 10 $\log_{10}$ $(\overline{\epsilon^2}/\overline{\epsilon_{DW}^2})$, of almost 13 dB for the NTSC format. In the following, the monochrome NTSC subjective weighting curve in Figure 2 is applied, with suitable frequency scaling, to both the

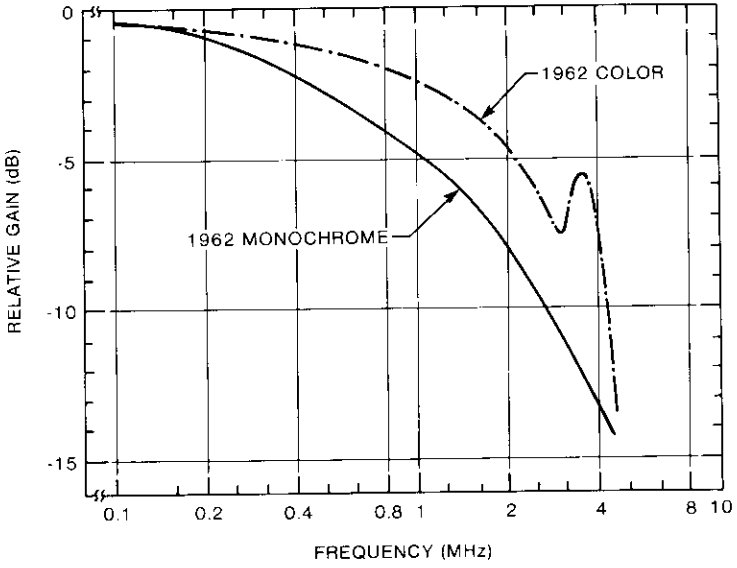

Figure 2. *Subjective Noise Weighting*

* Throughout, power transfer functions $D(f) = |D'(f)|^2$ are used, where $D'(f)$ is the voltage transfer function of the network.

luminance and chrominance components of the MAC format. This assumption was made because of the lack of subjective weighting curves for MAC systems.

S/N calculations for the MAC format

In the following subsections, *S/N*s are derived for the components transmitted in the MAC format.

MAC LUMINANCE AND COMPOSITE CHROMINANCE OUTPUT *S/N*

The review of standard NTSC conventions in the previous section provided the definitions needed to determine *S/N* for the MAC transmission format. Figure 3 shows the equivalent MAC 1-V peak-to-peak luminance transition for a color-bar-type pattern. This time waveform identifies the time intervals T_L and T_C allocated for luminance and chrominance, respectively, and the corresponding voltage levels.

Assuming basic 0- to 1-V R, G, and B inputs resulting from the scanning of a color bar pattern, the luminance signal is

$$Y = 0.299R + 0.587G + 0.114B \tag{6}$$

which has a minimum value of 0 V for black and a maximum value of 1 V. For the conventional color-bar pattern, the luminance waveform would resemble a descending staircase, as shown at the left of Figure 3. The luminance information collected during the approximately 52 μs of active video would be output in a shorter time, T_ℓ, for a compression ratio of $52/T_\ell$. For example, if T_ℓ is 39 μs, the luminance compression ratio is $\gamma_\ell = 4{:}3$.

Chrominance information is conveyed in MAC by two color-difference components transmitted on alternate scan lines. These color-difference signals (for 100-percent color bars) are [26]

$$V = R - Y \tag{7a}$$

$$U = B - Y \tag{7b}$$

or

$$V = 0.7R - 0.59G - 0.11B \tag{8a}$$

$$U = -0.3R - 0.59G + 0.89B \quad . \tag{8b}$$

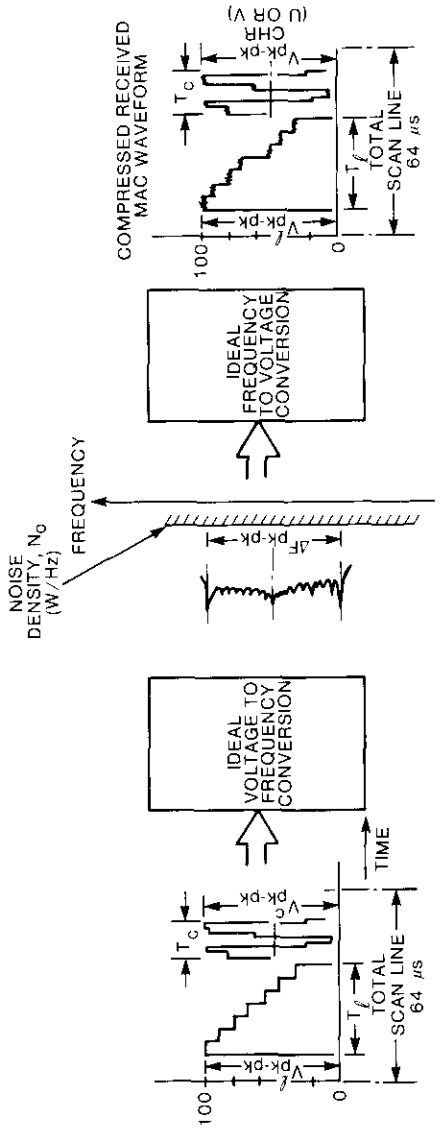

Figure 3. *MAC Transmission With No Pre-Emphasis*

From equation (8), the V signal ranges between ± 0.7 V and the U signal between ± 0.89 V for peak-to-peak values of 1.4 and 1.78 V, respectively. For these signals to produce the same peak frequency deviation as the luminance signal, an additional scaling is required to give

$$V' = \frac{V}{1.4} + 0.5 \tag{9a}$$

$$U' = \frac{U}{1.78} + 0.5 \quad . \tag{9b}$$

At the demodulator output at the right of Figure 3, the luminance output S/N in the compressed domain can be obtained by using the definition given in equation (2), as

$$S/N = \frac{(V_{pk\text{-}pk})^2}{\text{mean square error}} = \frac{(2\Delta F_{pk})^2}{(N_o/C)(f_m'^3/3)} = 12\left(\frac{\Delta F_{pk}}{f_m'}\right)^2 \frac{C}{N_o}\frac{1}{f_m'} \tag{10}$$

which is similar to the expression for NTSC, except that maximum baseband frequency, f_m', applies to the compressed signal and is equal to $\gamma_t f_m$. For example, for a luminance compression $\gamma_t = 4{:}3$ and $f_m = 4.2$ MHz, the maximum baseband frequency for compressed MAC is 5.6 MHz. Because of this wider baseband bandwidth, the peak frequency deviation, ΔF_{pk}, cannot be as large for MAC if the degree of overdeviation is unchanged and if the channel bandwidth is the same. For a 24-MHz channel bandwidth, for example, 0-dB overdeviation (*i.e.*, Carson's-rule deviation) would be 7.8 MHz for NTSC and 6.4 MHz for MAC with 4:3 luminance compression.

A final step in the MAC processing of the luminance waveform is time expansion and low-pass filtering to the final 4.2-MHz luminance bandwidth, f_m. This expansion process will not improve S/N further unless the expanded waveform is filtered with a noise bandwidth narrower than f_m. Also, application of the assumed subjective noise-weighting function to the compressed noise results in less subjective noise improvement, as noted below. The S/N in the compressed time domain applies to either the luminance or the color-difference voltage levels, provided that the U' and V' signals produce the same peak-to-peak frequency deviation of the transmitter. With the scaling of the color-difference signals given by equation (9), the chrominance and luminance waveforms produce the same peak frequency deviation.

De-emphasis and subjective weighting can be applied to the luminance *S/N* calculation, noting the following:

a. the de-emphasis curves are assumed to be defined in the compressed time domain;

b. the Barstow-Christopher (B-C) subjective weighting curve is defined in the expanded-time domain; and

c. to expand time, Δt is replaced by $\gamma\Delta t$ ($\gamma > 1$) so that time samples are output with a larger spacing. Equivalently, frequency functions are compressed by a similar factor, Δf being replaced by $\Delta f/\gamma$.

Therefore, to apply de-emphasis and subjective weighting to the luminance noise, equation (10) is replaced by

$$S/N = \left\{ \int_0^{f'_m} \frac{f^2 D(f)\ W(f/\gamma_\ell)}{(2\Delta F_{pk})^2 \cdot C/N_o}\, df \right\}^{-1} . \qquad (11)$$

This process integrates the noise in the compressed-time domain, where the noise out of the demodulator and the de-emphasis function are defined. Because the subjective-weighting relative power gain vs frequency function is defined in the expanded (final output) domain, this function must be mapped into the compressed-time domain in order to perform the integration, as indicated in Figure 4.

Beyond the de-emphasis network shown in Figure 4, the luminance and chrominance components can be considered to follow separate paths. In the upper path of the figure, in anticipation of the eventual time expansion by γ_ℓ, both the B-C subjective weighting curve and the final luminance filter can be expanded in frequency to operate on the compressed waveform. Similar operations are shown for the chrominance channel in the lower branch of Figure 4, where the scaling factor is f/γ_c.

To summarize the process shown in Figure 4, mean square errors are calculated as*

$$\overline{\epsilon_\ell^2} = \int_0^{f'_m} \frac{N_o}{C} f^2 D(f)\ W(f/\gamma_\ell)\ df \qquad (12a)$$

$$\overline{\epsilon_c^2} = \int_0^{\infty} \frac{N_o}{C} f^2 D(f)\ W(f/\gamma_c)\ C(f/\gamma_c)\ df \qquad (12b)$$

* Integrating to f'_m in equation (12a) assumes an ideal rectangular post-expansion luminance filter with bandwidth f'_m/γ_ℓ.

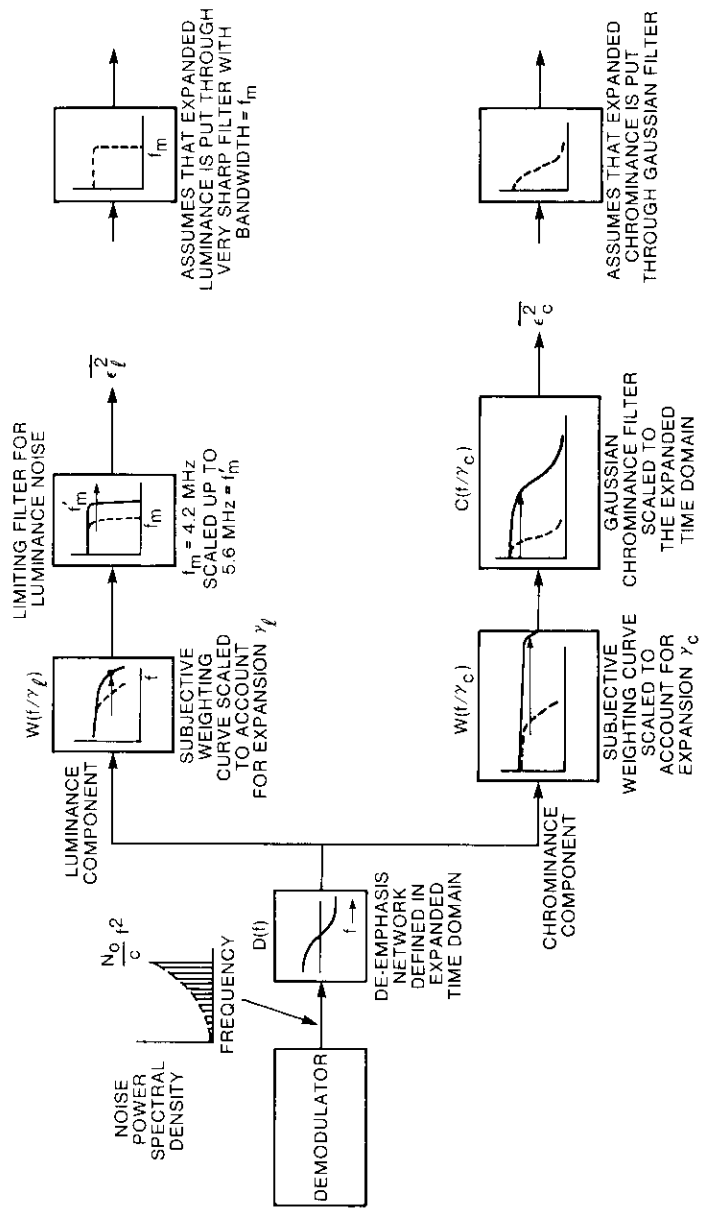

Figure 4. *Conceptual Model for Separating MAC Chrominance and Luminance and Applying De-Emphasis, Post-Expansion Filtering, and Subjective Weighting*

where $W(f)$ = B-C subjective weighting curve (as noted earlier, it is strictly an assumption to apply this function to MAC luminance and chrominance)

$D(f)$ = MAC de-emphasis curve (+3 dB, f_{co} MHz, −3 dB), where the crossover frequency, f_{co}, is defined in the compressed domain

$C(f)$ = power transfer function $[C(f) \doteq |C'(f)|^2]$ of the Gaussian chrominance filter

γ_c = chrominance compression factor (*i.e.*, $\gamma_c = 4$ for N-MAC)

γ_ℓ = luminance compression factor (*i.e.*, 4/3 for N-MAC)

f'_m = upper limit in the integration of luminance noise assuming a rectangular post-expansion luminance filter where, for example, $f'_m = \gamma_\ell \cdot 4.2$ MHz = 5.6 MHz.

MAC CHROMINANCE (U, V, AND COMPOSITE) OUTPUT S/N FOR THE N-MAC IMPLEMENTATION

For MAC, additional implementation details will impact the S/N on the chrominance channels. The following three items will affect chrominance output S/N:

a. vertical prefiltering of chrominance information at the transmitter;
b. transmission of color-difference information (the U' and V' signals) on alternate scan lines, with regeneration of the missing lines by interpolation at the receiver; and
c. scaling of U and V signals before they are applied to the modulator.

The scaling in item (c) is in addition to that given by equation (9) and determines the chrominance level sent over the channel. When related to the color-bar test pattern, this scaling is referred to as the *percent color-bars* factor (*i.e.*, 75- or 100-percent color bars), and determines the peak frequency deviation produced by the U' and V' signals. This scaling could result in a different peak frequency deviation for U' and V' than that produced by the luminance waveform.

Vertical Prefiltering. Figure 5 shows details of the sampling of typical scene material in the N-MAC format. In the upper part of this figure, a small portion of the sampling is shown for one video field where luminance (Y) and chrominance (U and V) samples are taken. Chrominance channels are sampled at a rate f_{sc} which is one-third the rate at which the luminance is sampled.

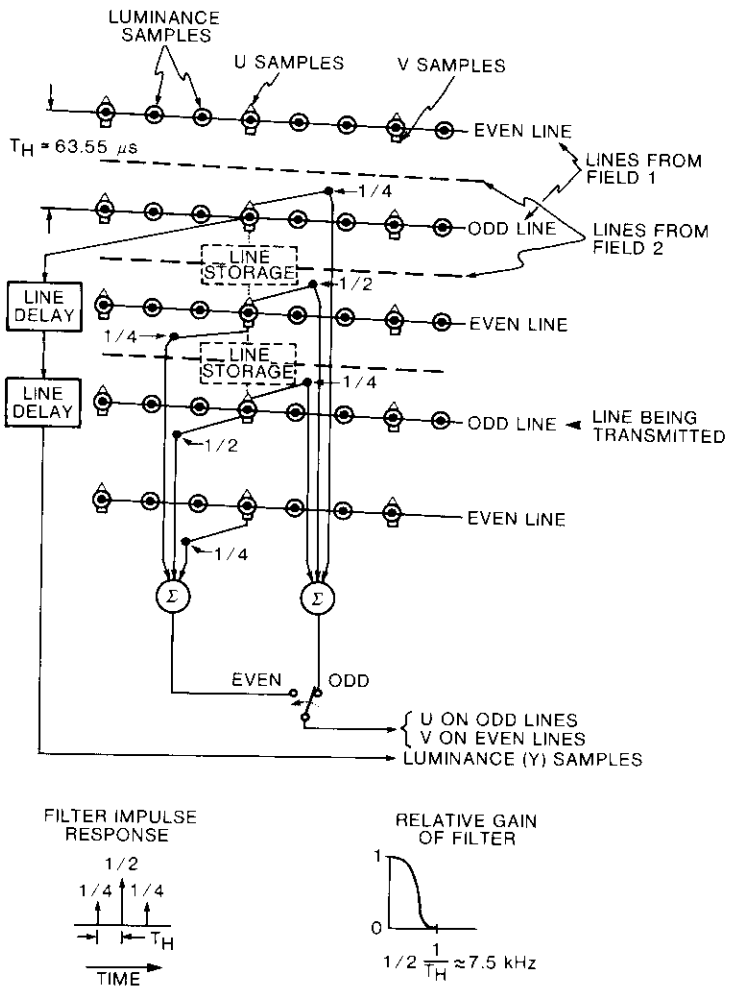

Figure 5. *Vertical Prefiltering of Chrominance Samples*

The scaled U and V samples are transmitted on alternate scan lines, U on the odd lines and V on the even lines. At the receiver, the missing line is filled in by interpolation.

Because information is eliminated (samples are skipped), vertical prefiltering is implemented at the transmitter with the effect of reducing the bandwidth of the chrominance information in the vertical direction. This prefiltering typically would use weights 1/4, 1/2, 1/4, as shown in Figure 5.

The discrete Fourier transform of the prefilter impulse response H_k, is

$$A_r \doteq \sum_{k=0}^{N-1} H_k \exp\left\{-j2\pi \frac{kr}{N}\right\}$$
$$= \frac{1}{4} + \frac{1}{2}\exp\left\{-j2\pi \frac{r}{N}\right\} + \frac{1}{4}\exp\left\{-j2\pi \frac{2r}{N}\right\} \quad . \qquad (13)$$

Replacing the frequency variable r/N by fT_H, where T_H is the horizontal line interval of 63.55 μs (the sampling rate in this case), the filter function can be obtained as $F(f) \doteq A_r A_r^*$ (where * denotes complex conjugate), giving

$$F(f) = \frac{3}{8} + \frac{1}{2}\cos(2\pi f T_H) + \frac{1}{8}\cos(2\pi 2 f T_H) \quad . \qquad (14)$$

As shown in the sketch at the bottom of Figure 5, the relative gain of the vertical prefilter goes to zero at one-half the horizontal line rate, or at about 7.5 kHz.

Alternate-Line Transmission of Color-Difference Information. Vertical prefiltering and the skipping of samples produces some distortion (filtering) of the original picture information; however, this error is usually not classified as noise. As shown in Figure 6, prefiltering will reduce the resolution of vertical chrominance detail. Sharp vertical chrominance transitions, as shown in Figure 6a, will be smoothed out as indicated in Figure 6b. Figures 6c and 6d indicate the alternate samples that are actually sent over the channel and the interpolated samples that are filled in at the receiver for two cases: where the abrupt transition ends on a transmitted sample, and where the abrupt transition begins on a transmitted sample. Simple interpolation is seen to be quite effective in reconstructing the original filtered waveform in Figure 6b. Relative distortion (the difference between Figure 6a and either 6c or 6d) is shown in Figure 6e.

Chrominance Level. An important factor in determining chrominance output *S/N* is the absolute level that is used to transmit the color difference signals over the channel. As noted earlier, application of the standard matrix equation to give the basic color difference signals U and V results in peak-to-peak values for 100-percent color bars of 1.4 V for V and 1.78 V for U. In these waveforms are not scaled further, the voltage waveforms shown in Figure 7 will result for the standard 75- and 100-percent color-bar patterns. Unless additional scaling is applied, these larger voltage levels will result in

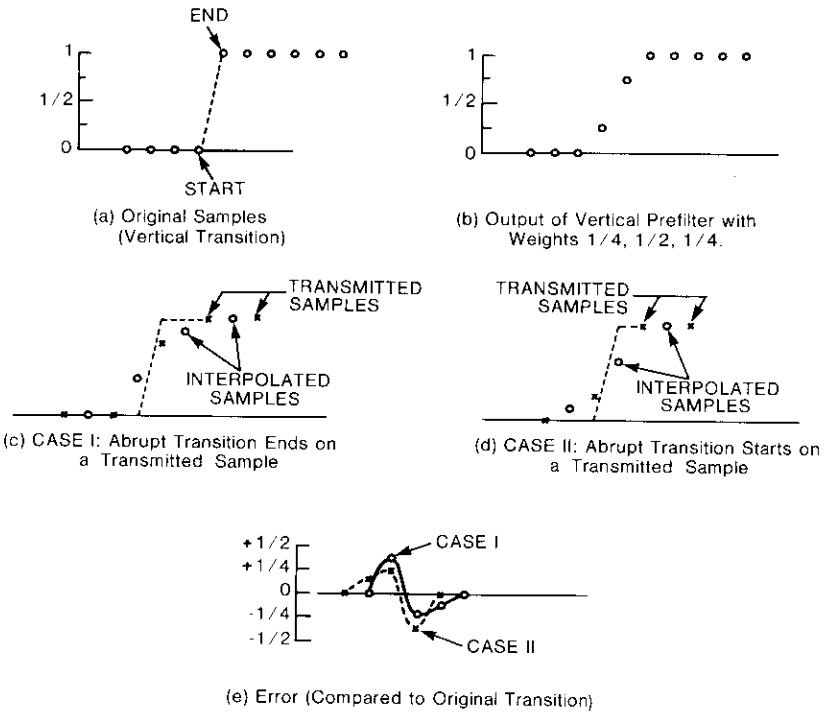

Figure 6. *Effect of Vertical Prefiltering, Alternate Sample Deletion, and Reconstruction by Interpolation (1/2, 1/2) on an Abrupt Transition*

larger peak-to-peak frequency deviations ($\Delta F^U_{pk\text{-}pk}$ and $\Delta F^V_{pk\text{-}pk}$) than those generated by the luminance waveform. If Carson's rule were not violated for the band-limited channel, equation (11) would indicate larger output *S/N*s due to the larger deviations produced by the color-difference signals.

For N-MAC transmission with 4/3 luminance compression, Carson's rule bandwidth for luminance is

$$B_c^\ell = 2(\Delta F_{pk}^\ell + \gamma_\ell \cdot 4.2\ \text{MHz}) = 24\ \text{MHz} \qquad (15)$$

giving $\Delta F^\ell_{pk} = 6.4$ MHz, or $\Delta F^\ell_{pk\text{-}pk} = 12.8$ MHz. Typical peak-to-peak deviations of 17.5 MHz might be used for luminance, giving an overdeviation of 2.7 dB.

For the color-difference signals, the waveforms in Figure 7 without additional scaling would produce the peak-to-peak deviations shown in Table 1. If both color-difference waveforms are scaled to produce the same

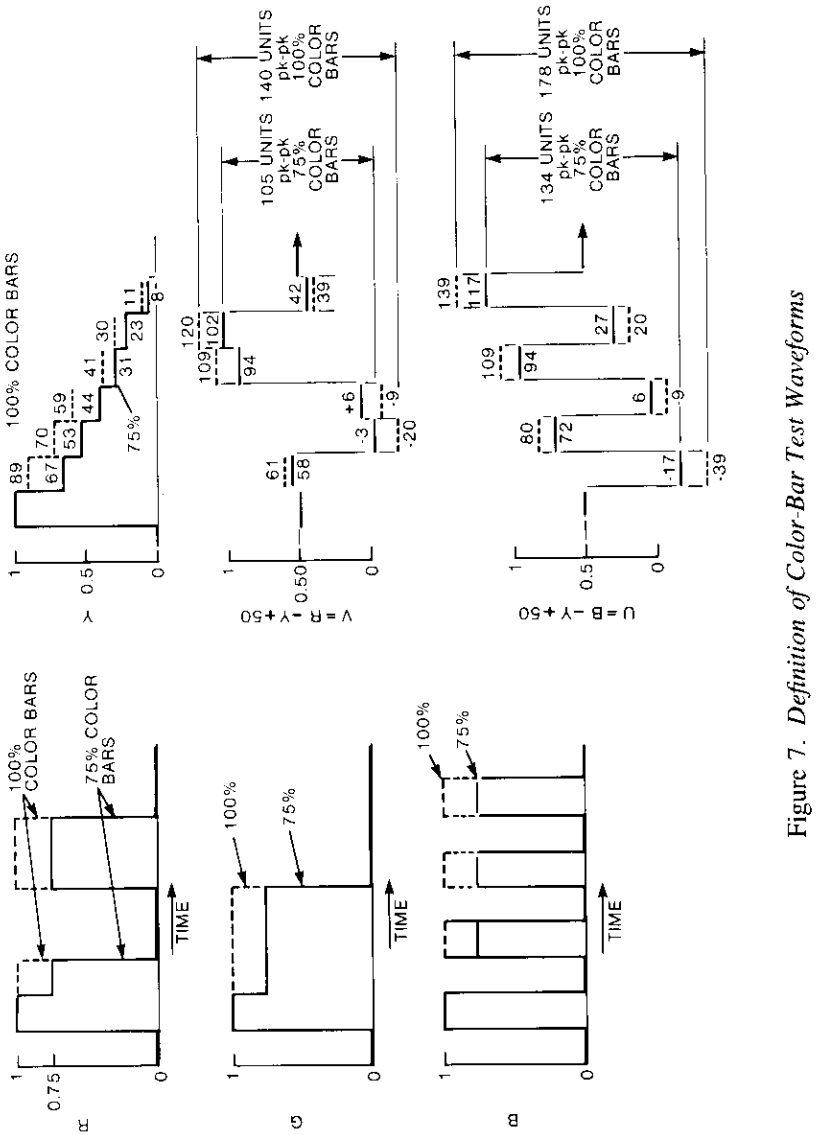

Figure 7. *Definition of Color-Bar Test Waveforms*

TABLE 1. FREQUENCY MODULATION PARAMETERS FOR COLOR-DIFFERENCE WAVEFORMS

COLOR BARS	$V_{pk\,pk}$	$\Delta F_{pk\,pk}$* (MHz)	OVERDEVIATION (dB) OF CHROMINANCE γ_c = 4:1 BW = 1 MHz	BW = 1.3 MHz
100%				
$V \doteq R - Y$	1.40	24.5	3.7	5.1
$U \doteq B - Y$	1.78	31.1	5.7	7.2
75%				
$V = R - Y$	1.05	18.3	1.2	2.6
$U = B - Y$	1.34	23.4	3.3	4.7
75% With Additional Scaling to Produce 1 $V_{pk\text{-}pk}$**				
$V = R - Y$	1.00	17.5	−0.77	2.2
$U = B - Y$	1.00	17.5	−0.77	2.2

* Luminance $\Delta F_{pk\,pk}$ = 17.5 MHz, giving 2.7-dB luminance overdeviation.

** Achieving these peak-to-peak values requires additional scaling of the U and V waveforms by factors of 0.749 and 0.952, respectively.

peak-to-peak level as the luminance level for 75-percent color bars, the resulting color-difference signals would be

$$U' = 0.75\,(0.749)\,U + 0.5 \tag{16a}$$

$$V' = 0.75\,(0.952)\,V + 0.5 \quad . \tag{16b}$$

Output S/Ns for the received U and V signals are related to the peak luminance level of 1 V. From equations (11) and (12)

$$(S/N)_U = \left\{ \frac{\int_0^\infty (N_o/C)\, f^2 D(f)\; W(f/\gamma_c)\; C(f/\gamma_c)\; df}{(\Delta F^U_{pk\text{-}pk})^2} \right\}^{-1} \tag{17a}$$

$$(S/N)_V = \left\{ \frac{\int_0^\infty (N_o/C)\, f^2 D(f)\; W(f/\gamma_c)\; C(f/\gamma_c)\; df}{(\Delta F^V_{pk\text{-}pk})^2} \right\}^{-1} \quad . \tag{17b}$$

To summarize, the direct generation of color-difference signals U and V produces signals with peak-to-peak values that are much larger than the peak-to-peak luminance voltage for a black-to-white transition. This results in a

larger peak-to-peak frequency deviation for the U and V signals than for Y. Additional scaling can be used to nearly equalize the frequency deviations produced by the components, but this will result in the U and V signals having lower output S/Ns.

Effect of Interpolation at the Receiver. The effect of sending U and V on alternate lines is that the missing U (or V) lines must be reconstructed at the receiver by interpolation. The interpolator with weights (1/2, 1/2) has a noise bandwidth (the square of its impulse response) of $(1/2)^2 + (1/2)^2 = 1/2$, so that independent noise numbers into the interpolator result in a 3-dB reduction in the mean square value of the noise out of the interpolator. The signal is not affected except that, as noted in Figure 6, the combined processes of prefiltering and interpolation act as a filter which distorts the signal.

Noise reduction due to interpolation on alternate lines only reduces noise on every other vertical line for U (or V); on the uninterpolated line, U (or V) noise is unaffected. Therefore, on the average, the interpolation reduces noise by only 1.25 dB.* Equations (17a) and (17b) can thus be modified by adding 1.25 dB to account for the improvement due to interpolation. For comparison, a composite chrominance S/N can be defined as

$$\left(\frac{S}{N}\right)_c = \left\{\left(\frac{S}{N}\right)_U^{-1} + \left(\frac{S}{N}\right)_V^{-1}\right\}^{-1} . \qquad (18)$$

SUMMARY OF Y, U, AND V S/N RELATIONSHIPS

Expressions for MAC luminance S/N were determined above as the ratio of squared peak-to-peak luminance signal to mean square noise. Mean square noise is determined by numerically integrating the product of four functions: the f^2 noise out of the FM demodulator, the de-emphasis characteristic which acts on the time-compressed waveform, the frequency-mapped B-C subjective weighting curve, and the luminance post-expansion filter which is also mapped to the time-compressed domain.

The MAC chrominance channels were treated in a similar manner, assuming that both the U' and V' signals were scaled at the transmitter to produce a specified peak-to-peak deviation of the transmitter. A similar procedure was used to determine the S/N of the two color-difference signals, again requiring the numerical integration of the product of four functions: the f^2 noise, the

* This averaging is an approximation. Measurements [27] have shown that S/N levels on the interpolated lines are indeed 3 dB higher than on the uninterpolated lines.

de-emphasis curve, the subjective weighting curve, and the post-expansion chrominance filter $C(f)$.

Because the post-expansion chrominance filter has an important effect on the S/Ns in the color-difference channels, it must be carefully chosen and accurately represented in the calculation. Chrominance filters yielding no overshoot or ringing on transients are necessary for acceptable color TV performance. Candidates would include Bessel and Gaussian types. For convenience in modeling, the Gaussian shape $C(f) = e^{-af^2}$ was used in this study. In terms of noise performance, this filter is much more gradual than the ideal rectangular filter that is assumed for the luminance channel.

Following this process, three output S/Ns can be calculated: $(S/N)_Y$ for luminance, $(S/N)_{U'}$ for scaled B-Y, and $(S/N)_{V'}$ for scaled R-Y. A composite chrominance S/N was also determined from equation (18) which serves as a useful single measure of overall chrominance S/N.

MAC R, G, AND B OUTPUT S/N

The conversion from Y, U, and V to R, G, and B is performed as shown conceptually in Figure 8. Conversion to the three primary color components uses the relationships [27]

$$R = Y + b^{-1}(\hat{V}' - 0.5) \qquad (19a)$$

$$B = Y + a^{-1}(\hat{U}' - 0.5) \qquad (19b)$$

$$G = Y - b^{-1}(0.508)(\hat{V}' - 0.5) - a^{-1}(0.186)(\hat{U}' - 0.5) \qquad (19c)$$

where a^{-1} and b^{-1} are the inverses of the scale factors applied to U and V, respectively, at the transmitter.

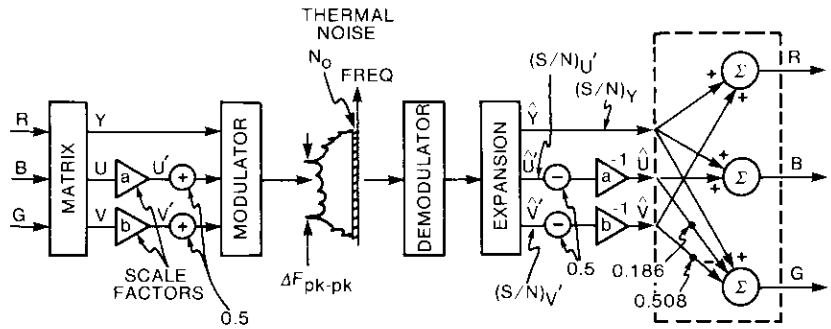

Figure 8. *Conceptual Model for Generating Three Primary Color Outputs*

To produce the proper R, G, B outputs, any scaling of the U and V components at the transmitter must be compensated for at the receiver so that the received U and V are correct on the same scale as the Y signal. When this is done, the noise that appears on U' and V' is also amplified so that, although $(S/N)_U$ and $(S/N)_V$ are not altered, the R, G, and B S/N outputs are degraded. This is because these components pick up more noise, relatively, than they would if they had been sent over the channel at full strength. Noise enhancement also occurs because the R, G, and B values are rederived by subtracting components [for example, $R = Y + (R - Y)$] having uncorrelated noise voltages that add on an rms basis.

The operations in equation (19) add the output luminance and color-difference voltages, each of which contains noise, to produce R, G, and B voltages. The voltage scale factors a and b increase both the signal and the noise, and the independent noise voltages on the three components ($\hat{Y}$, $\hat{U}'$, and $\hat{V}'$) add on an rms basis with variance scaled up by the square of the scale factors, giving

$$\left(\frac{S}{N}\right)_R = \left[\left(\frac{N}{S}\right)_Y + (1/b)^2\left(\frac{N}{S}\right)_{V'}\right]^{-1} \tag{20a}$$

$$\left(\frac{S}{N}\right)_B = \left[\left(\frac{N}{S}\right)_Y + (1/a)^2\left(\frac{N}{S}\right)_{U'}\right]^{-1} \tag{20b}$$

$$\left(\frac{S}{N}\right)_G = \left[\left(\frac{N}{S}\right)_Y + (1/b)^2(0.508)^2\left(\frac{N}{S}\right)_{V'} + (1/a)^2(0.186)^2\left(\frac{N}{S}\right)_{U'}\right]^{-1} \tag{20c}$$

If the chrominance level reduction by factors a and b is not restored at the receiver, the noise enhancement in equation (20) is not experienced. For example, to transmit 75-percent color bars over the channel, a would be selected as 0.75 (0.749) and b would be selected as 0.75 (0.952), as indicated by equation (16). These scalings would be only partially restored, with received U multiplied by (1/0.749) and received V multiplied by (1/0.952) to produce the R, G, and B outputs for 75-percent color bars.

Numerical results

The relationships derived in the previous section have been used first to compute unweighted S/N with no de-emphasis. Additional filters were then added individually, and finally together, to determine the improvement

experienced. For all calculations, B-C subjective weighting is used with a -3 dB, f_{co}, $+3$ dB de-emphasis function [23], where the crossover frequency, f_{co}, is 1.76 MHz in the uncompressed domain. (Equivalent, for example, to 2.64 MHz in the 3:2 compressed domain.)

Results for luminance S/N are given in Table 2. The unweighted, unde-emphasized results in the first column are simply

$$S/N = 12(\Delta F_{pk}/f'_m)^2 \cdot C/N_o \cdot 1/f'_m$$

where ΔF_{pk} = 8.75 MHz, C/N_o = 84.6 dB, and f_m = 4.2 MHz times the luminance compression ratio. The weighted de-emphasized results are 11 dB higher, giving the numbers in the last column.

TABLE 2. LUMINANCE S/N (C/N_o = 84.6 dB-Hz, 75% COLOR BARS, ΔF_{pk} = 8.75 MHz)

			IMPROVEMENT (dB)			
SYSTEM NO.	γ_ϵ	S/N (dB)	DUE TO DE-EMPHASIS	DUE TO SUBJECTIVE WEIGHTING	DUE TO DE-EMPHASIS AND SUBJECTIVE WEIGHTING	S/N (dB)
1	4:3	31.8	1.3	10.3	11	42.8
2	5:4	32.6	1.3	10.3	11	43.6
3	3:2	30.2	1.3	10.4	11	41.2

Chrominance S/Ns are obtained by combining the chrominance filter functions with the de-emphasis and subjective weighting functions to give the overall equivalent noise bandwidth of the chrominance channel. Results are sensitive to the assumed shape and bandwidth of the chrominance filter. An assumed Gaussian filter that is 3 dB down at bandwidth B_c = 1.2 MHz, with a very sharp attenuation characteristic beyond the 6-dB point, produces the results given in Table 3. The improvement in composite chrominance S/N—defined as the combined $(S/N)_U$ and $(S/N)_V$ according to equation (18) increased by 1.25 dB to account for interpolation—varies with chrominance bandwidth. The S/Ns in Table 3 apply to U, V, and combined chrominance, and to the separate R, G, and B components. Composite chrominance S/Ns is plotted in Figure 9 as a function of chrominance bandwidth B_c.

Figure 10 summarizes the overall (subjective weighting plus de-emphasis) R, G, and B S/N outputs as a function of B_c. Note that the individual color

TABLE 3. TYPICAL CHROMINANCE OUTPUT S/N (dB) (C/N_o = 84.6 dB-Hz, 75% COLOR BARS, ΔF_{pk} = 8.75 MHz, 3-dB BW OF GAUSSIAN CHROMINANCE FILTER = 1.2 MHz)

	SYSTEM 1 (γ_c = 4:1)				SYSTEM 2 (γ_c = 3.75:1)				SYSTEM 3 (γ_c = 3:1)			
	F^*+ $S+$ $D+$	F^*+ $S+$	F^*+	F^*	F^*+ $S+$ $D+$	F^*+ $S+$	F^*+	F^*	F^*+ $S+$ $D+$	F^*+ $S+$	F^*+	F^*
COMPONENT	C	C	C		C	C	C		C	C	C	
$(S/N)_U$	39.8	38.8	33.8	26.0	40.1	39.7	34.7	26.9	42.6	42.6	37.6	29.8
$(S/N)_V$	39.8	38.8	33.8	26.0	40.1	39.7	34.7	26.9	42.6	42.6	37.6	29.8
$(S/N)_{composite}$	36.8	35.8	30.8	23.0	37.7	36.7	31.7	23.8	39.6	39.6	34.6	26.8
$(S/N)_R$	37.8	36.9	30.2	24.7	38.6	37.7	31.1	25.5	38.7	38.3	30.5	26.8
$(S/N)_G$	40.5	39.7	32.0	28.1	41.4	40.6	32.8	29.0	40.3	39.7	31.2	28.8
$(S/N)_B$	36.2	35.3	29.1	22.9	37.1	36.1	29.9	23.7	37.6	37.3	29.9	25.5

$F^* = f^2$ noise
S = subjective weighting
D = de-emphasis
C = chrominance filter

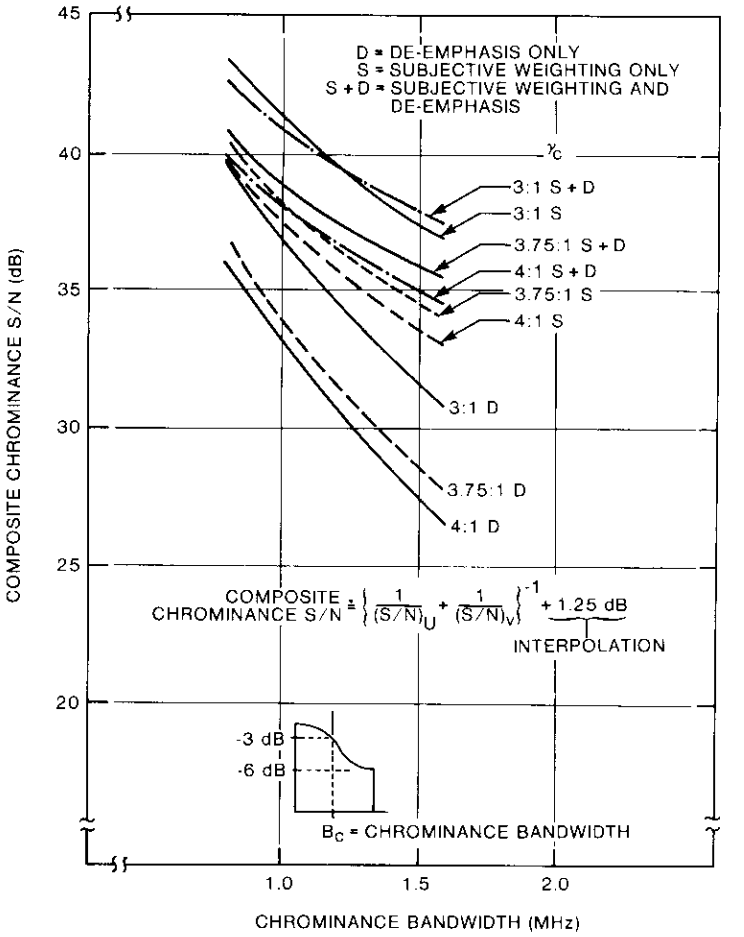

Figure 9. *Composite Chrominance S/N vs Chrominance Bandwidth, B_c*

component S/Ns generally decrease in the order green (highest), then red, and then blue. Differences between the three systems are small (within a decibel), with no system consistently giving higher values.

The analytical model predicts S/Ns for MAC transmission that agree closely with measurements made in the laboratory for N-MAC [26]. These comparisons are summarized in Table 4 for conditions of 9-MHz peak frequency deviation, no pre-emphasis/de-emphasis, a 1-MHz chrominance bandwidth, and C/N_o = 84 dB-Hz. The results are within the expected measurement accuracy.

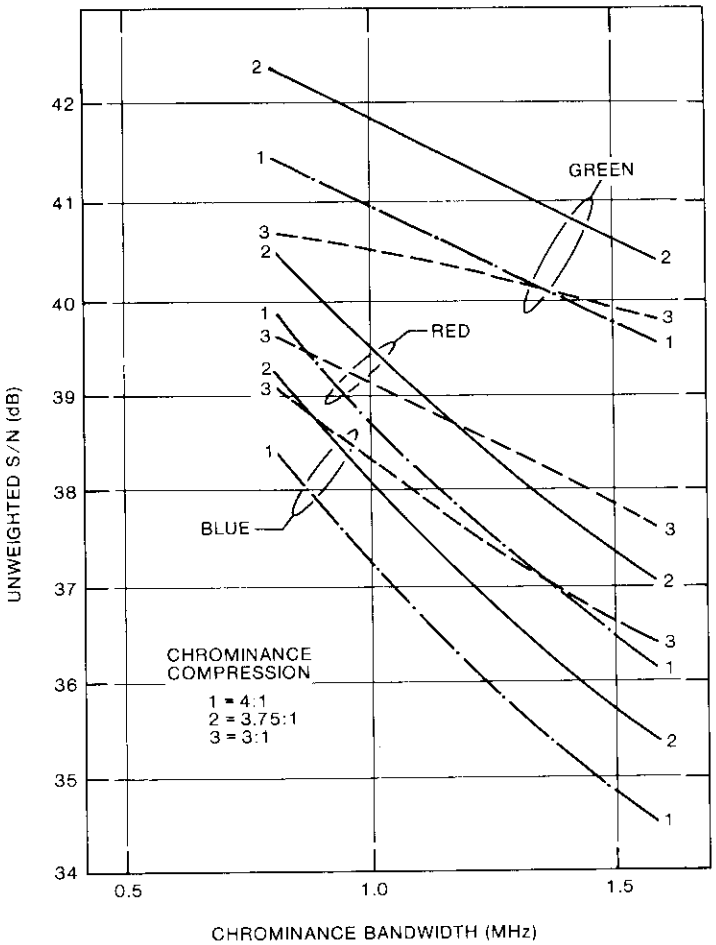

Figure 10. *$(S/N)_R$, $(S/N)_G$, and $(S/N)_B$ for the Three Systems (weighted, with de-emphasis)*

Simulation results

Simulation results for the three systems have been obtained by modifying a software simulation program [23] that uses two scan lines of either color-bar or multiburst test patterns.

The simulation model

Figure 11 shows an overall conceptual model for simulation of the three MAC formats. The simulation model generates 8,192 samples corresponding to two scan lines in the compressed time domain. Portions of these scan

TABLE 4. 9-MHz PEAK FREQUENCY DEVIATION COMPARISONS

COMPONENT	MEASUREMENTS ON N-MAC FROM [27]	PREDICTED FROM MODEL
$(S/N)_L$	41.1	41.8
$(S/N)_C$ $(U + V)_{avg}$	43.6	43.5*
$(S/N)_R$	39.0	39.3
$(S/N)_G$	40.0	40.8
$(S/N)_B$	37.9	38.3

*This "composite chrominance" *S/N* is obtained by increasing the *S/N* of both the *U* and *V* components by 1.25 dB to account for the noise reduction due to interpolation of alternate lines, and then combining *U* and *V* into a composite chrominance signal where noises add on an rms basis. This addition effectively doubles the noise or reduces *S/N* by 3 dB. Thus, the *S/N* of composite chrominance, which is actually a hypothetical quantity that cannot be measured, is approximately 1.75 dB lower than the *S/N* of the individual, uninterpolated *U* and *V* components.

lines are filtered by individual chrominance and luminance filters (scaled to apply to the compressed time domain) before the segments are again combined into a composite modulating waveform. The composite waveform is then pre-emphasized before being scaled and applied to the FM modulator. For some simulations, the pre-emphasis/de-emphasis (PE/DE) steps were omitted. Note also in Figure 11 that the options for either AC or DC coupling* to the modulator are included in the model.

After the video waveform is used to modulate the transmitter with a specified peak frequency deviation, ΔF_{pk}, the signal is passed through the satellite channel. A more detailed model of this channel, shown in Figure 12, includes the transmit IF filter, the satellite input filter, the traveling wave tube amplifier (TWTA), the satellite output filter, and the IF receive filter. Prior to the IF receive filter, Gaussian random numbers are added to simulate the effect of thermal noise. When thermal noise is omitted, the simulation program measures the effect of distortion alone.

The output of the simulated demodulator is de-emphasized (if included), and the luminance and chrominance components are separated and individually filtered. *S/N*s are computed by comparing the received components to the ideal noise-and-distortion-free replicas which were generated and saved at the transmitter. The *S/N* is then computed as peak-to-peak video, squared, divided by mean square noise plus distortion. By eliminating the noise at the input to the receiver, the distortion contribution can be isolated.

*With AC coupling, the mean is removed from the video waveform and the peak voltage value is found (+ or −). This voltage is then set to produce the desired ΔF_{pk}. With DC coupling, full-scale values of the video waveform produce $\pm\Delta F_{pk}$, regardless of the symmetry of the waveform.

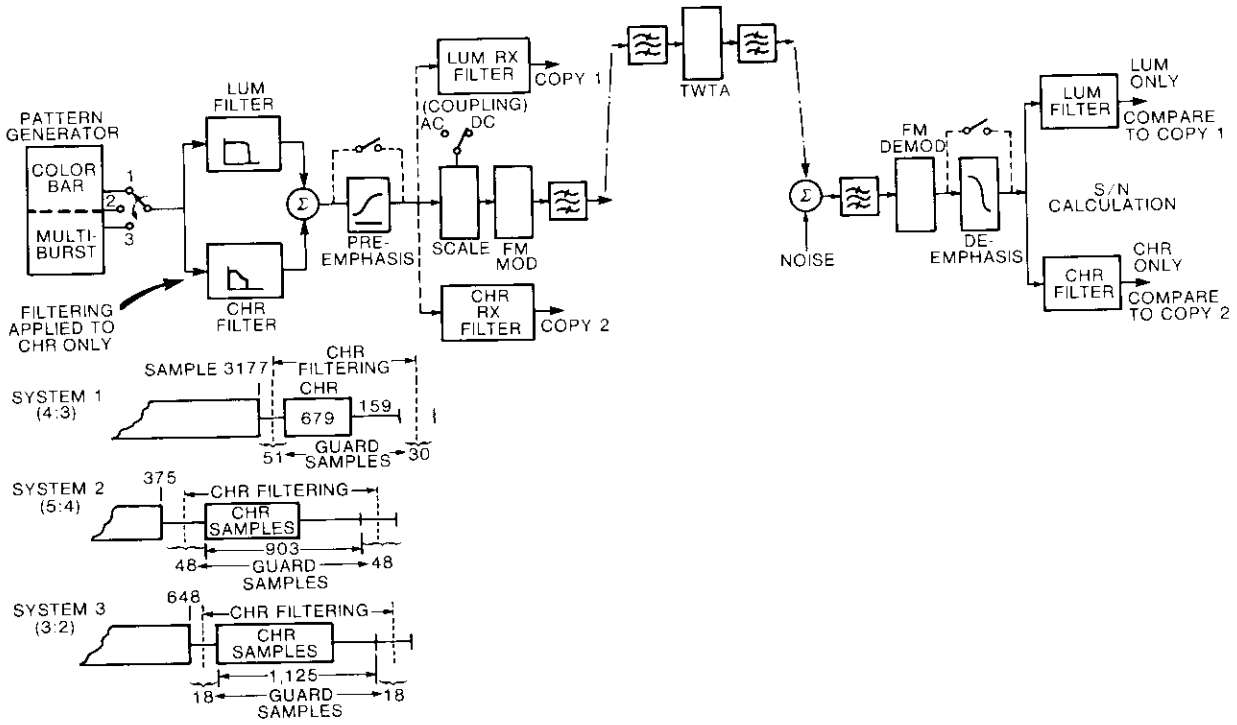

Figure 11. *Simulation Model*

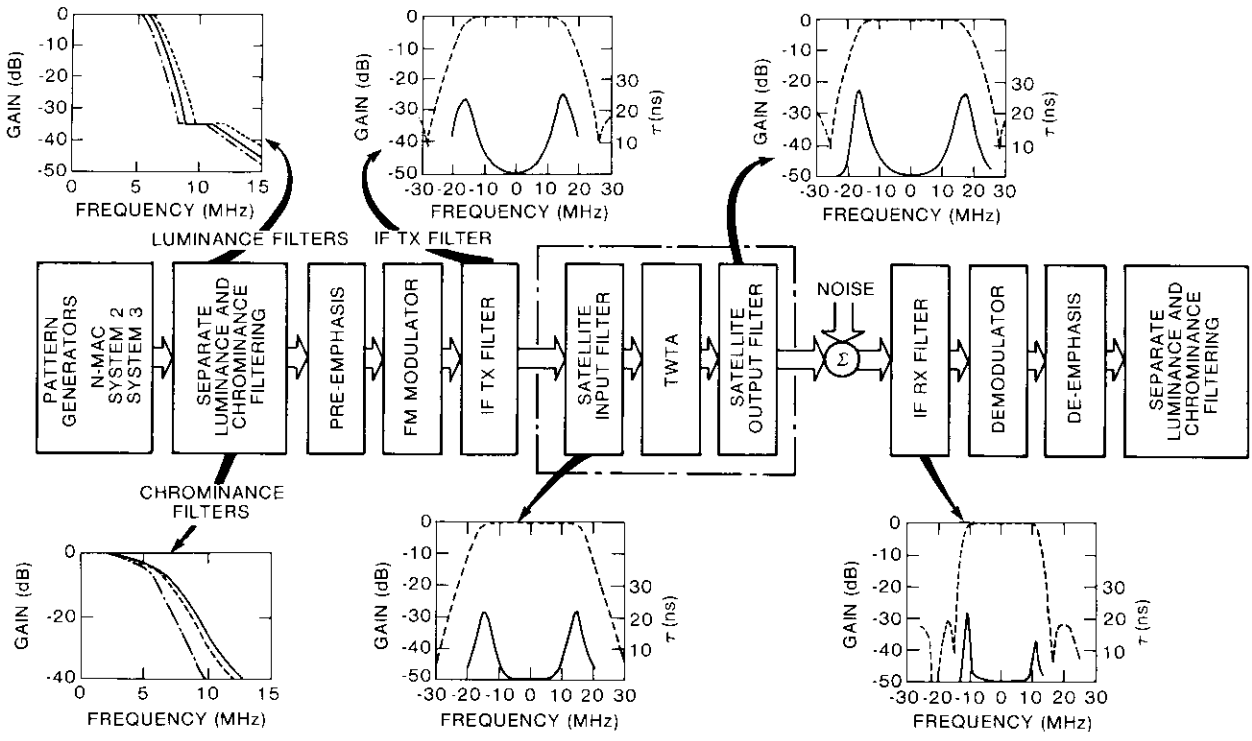

Figure 12. *Detailed Channel Model*

Simulated RF spectra for MAC transmission

Initial calibration results were obtained for the three transmission formats. Figure 13a shows the unpre-emphasized color-bar waveforms for the three formats. With a -3 dB, f_{co}, $+3$ dB pre-emphasis function, the color-bar waveform appears as shown in Figure 13b. The pre-emphasis crossover frequencies for the MAC formats with 5:4, 4:3, and 3:2 luminance compression ratios are 2.2, 2.35, and 2.64 MHz, respectively, in the compressed domain.

Additional results were obtained for the power density spectra of a color bar for the three formats, both with and without pre-emphasis, for different values of peak frequency deviation, ΔF_{pk}, as shown in Figures 14 through 17.

For similar conditions, differences in the spectral densities of the three systems are difficult to determine from the spectral plots themselves. However, slight differences do appear if the spectra are integrated to determine the fraction of power outside bandwidth B for different values of ΔF_{pk}. These results are shown in Figures 18 through 20.

Simulated output S/N values

Simulation experiments were conducted to obtain output S/Ns for the three transmission formats.

CALIBRATION AND CONFIDENCE INTERVALS

Several calibration runs were made to test the absolute accuracy of the simulation model. When output S/N is measured by processing only two scan lines in the program, a question arises about statistical variation in the results and the confidence intervals that can be assigned to the answers. Assuming that the noise on the output video signal is Gaussian (which is valid for operation well above threshold) with a true population variance σ^2, then a simulation experiment that produces an estimate s^2 of this variance would expect a variance in this sample variance of [28]

$$\text{Var}\{s^2\} = \frac{2\sigma^4(n-1)}{n^2} \approx \frac{2\sigma^4}{n}$$

where n is the number of independent samples of the output noise that are collected over two scan lines. The number of independent samples collected in the simulation can be estimated as

$$n = N \cdot f_s/(\gamma_i BB_i)$$

where N = block size used in the simulation
f_s = sampling rate used in the simulation
γ_i = compression ratio for system luminance or chrominance
BB_i = output baseband bandwidth of luminance or chrominance.

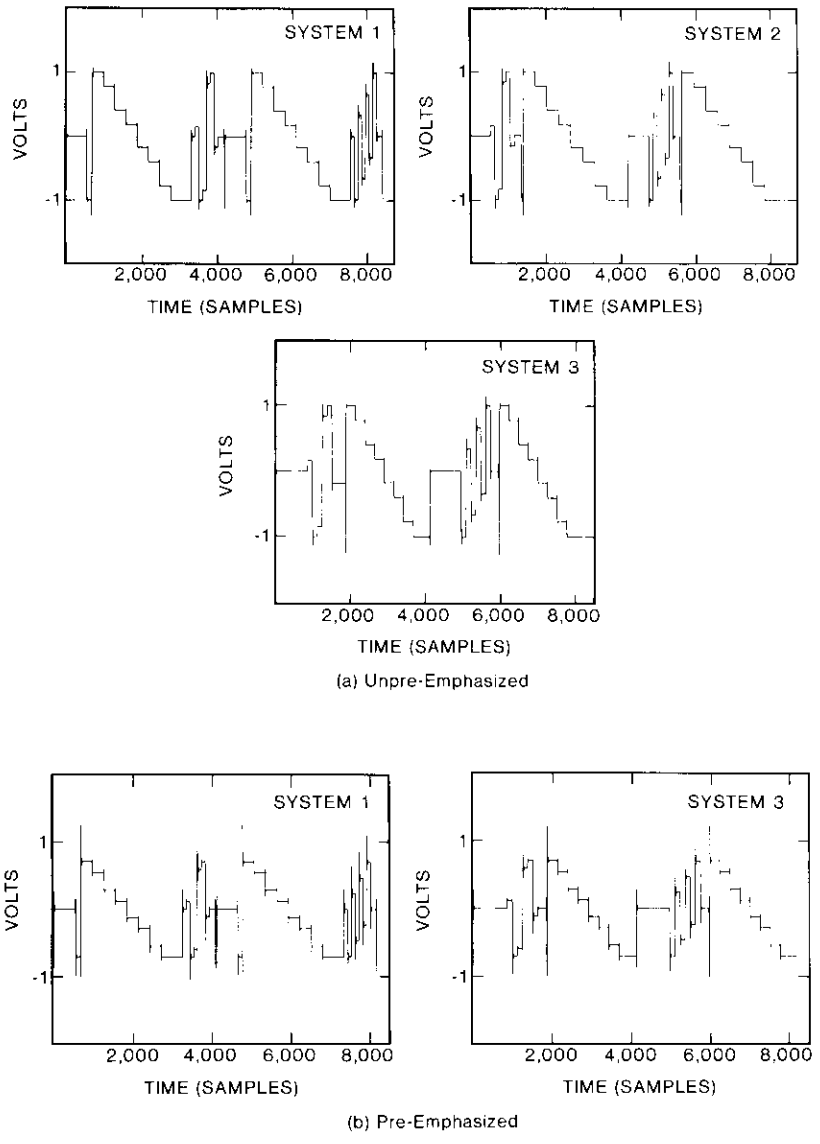

Figure 13. *Color-Bar Waveforms*

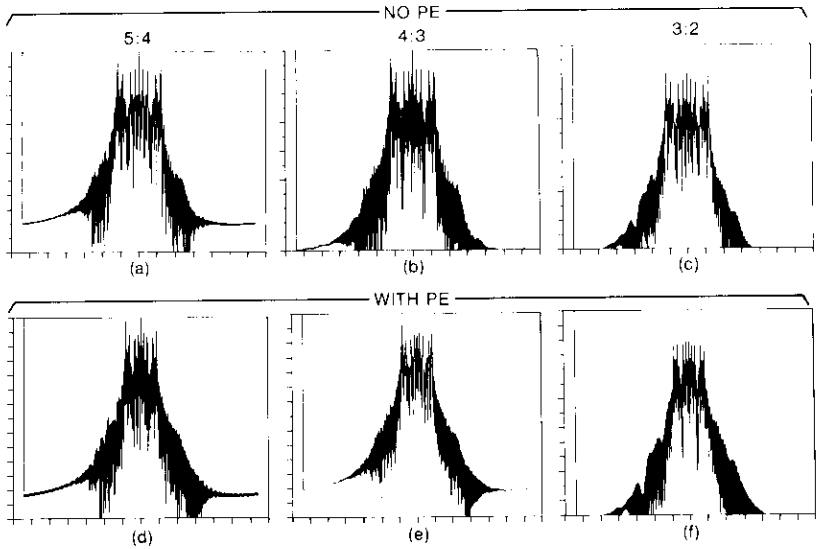

HORIZONTAL SCALE: -35 TO +35 MHz, 5 MHz/DIV
VERTICAL SCALE: 0-70 dB, 5 dB/DIV

Figure 14. *Power Spectra:* $\Delta F_{pk} = 6$ *MHz*

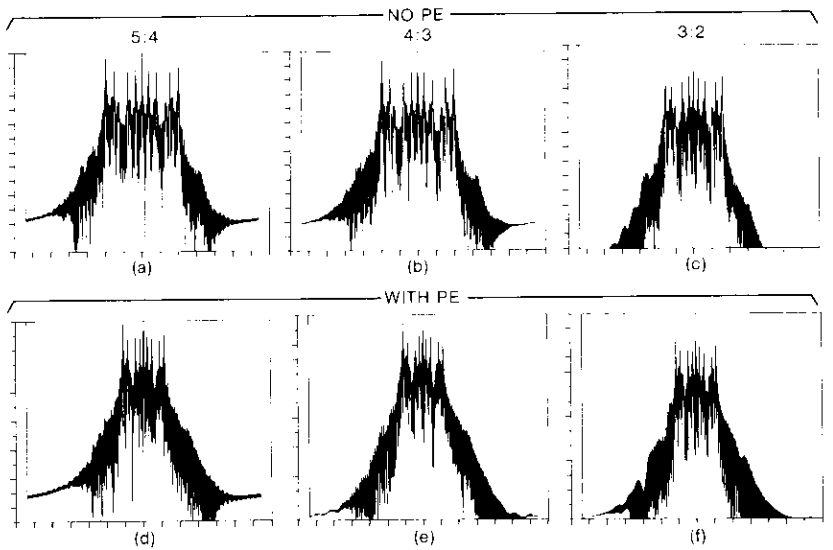

Figure 15. *Power Spectra:* $\Delta F_{pk} = 8$ *MHz*

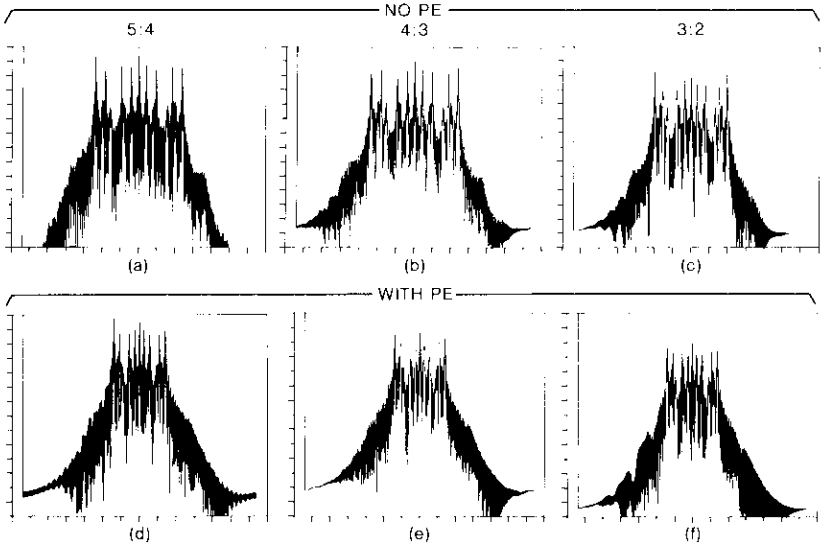

Figure 16. *Power Spectra:* $\Delta F_{pk} = 10$ *MHz*

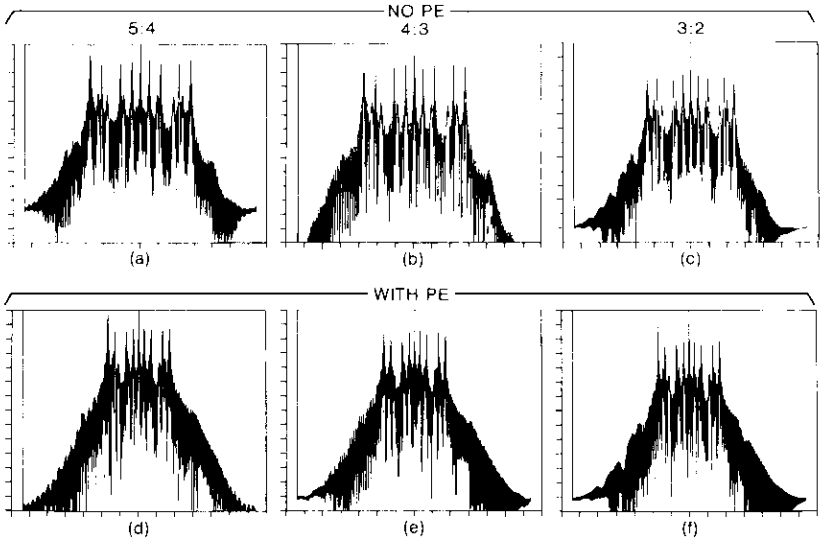

Figure 17. *Power Spectra:* $\Delta F_{pk} = 12$ *MHz*

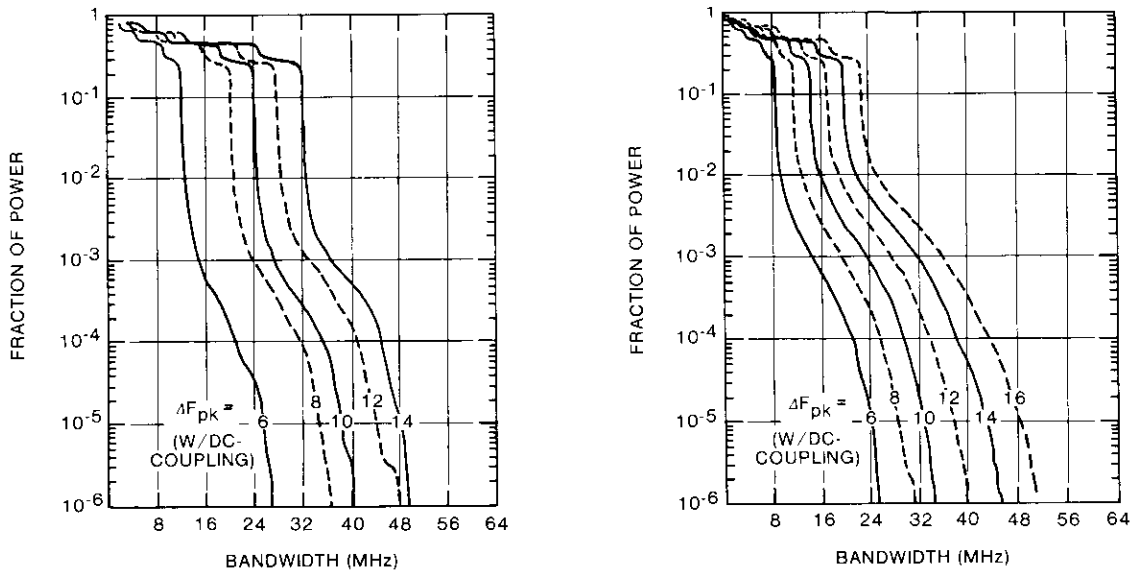

Figure 18. *Cumulative Power Density Spectra vs Bandwidth,* γ_ℓ = 5:4

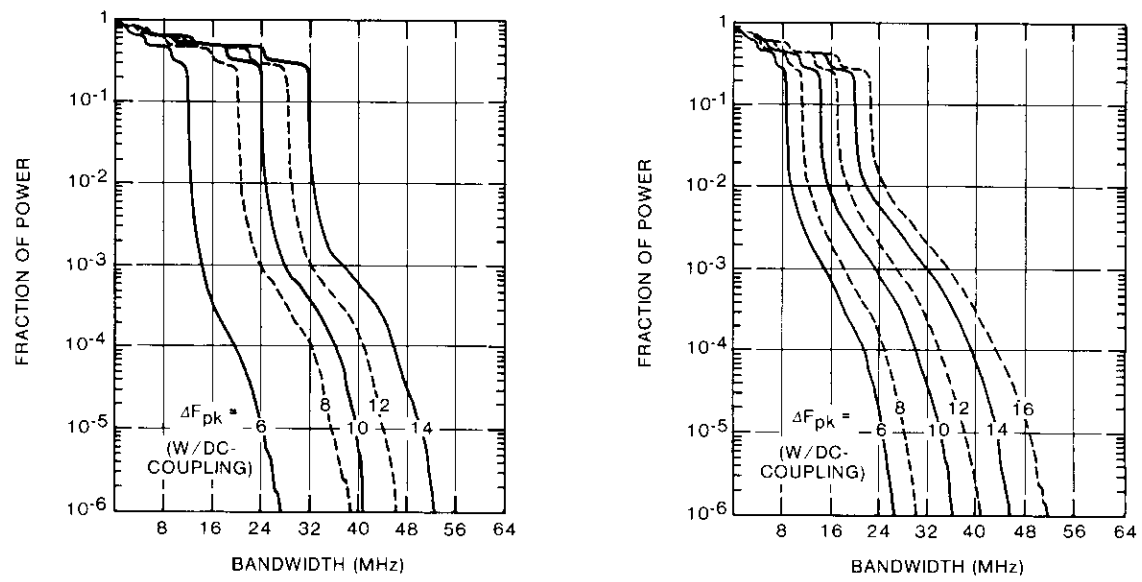

Figure 19. *Cumulative Power Density Spectra vs Bandwidth,* γ_ℓ = 4:3

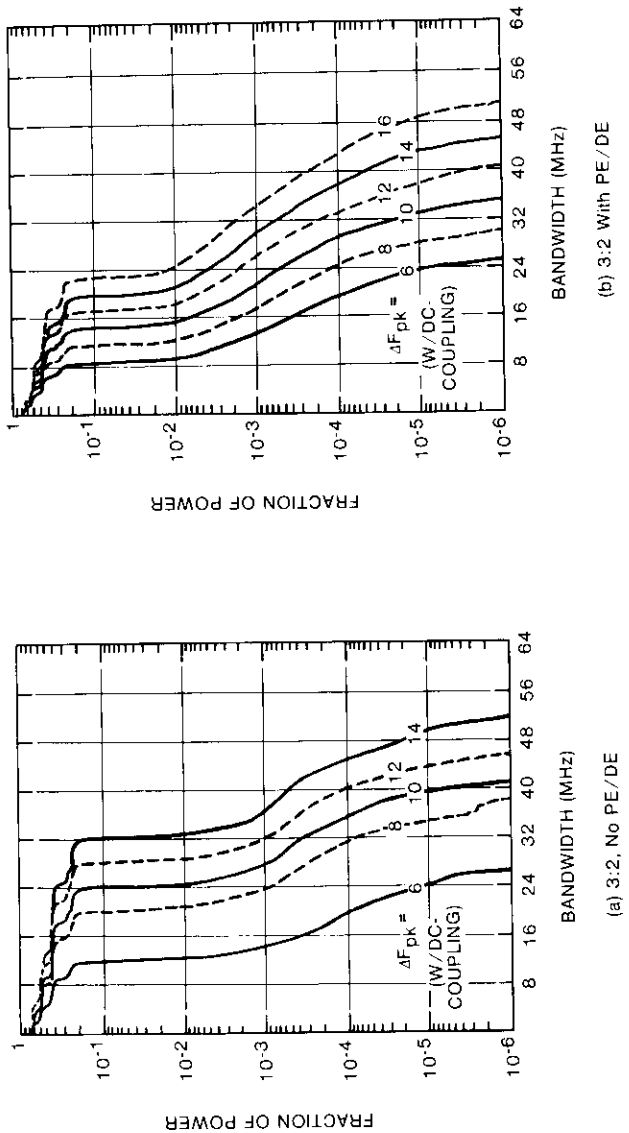

Figure 20. *Cumulative Power Density Spectra vs Bandwidth,* $\gamma_\ell = 3:2$

For the three systems being simulated, approximately 6,000 luminance and 2,000 chrominance samples are included in the simulation of two scan lines. Considering the filtering applied to the demodulator outputs, approximately 500 to 600 independent luminance samples and 130 independent chrominance samples are available from each simulation. Estimates of $\pm 2\sigma$ (95 percent) confidence intervals depend only slightly on the system, and result in expected accuracies of ± 0.5 dB for luminance and ± 1 dB for chrominance.

A short series of calibration tests was made to compare the simulation results to the results predicted by the analytical model that was described previously. The results, given in Table 5, generally show agreement to within the confidence intervals that would be expected in the simulation.

TABLE 5. COMPARISON OF SIMULATION RESULTS TO ANALYTICAL RESULTS (THERMAL NOISE ONLY)

COMPONENT	SIMULATION* (ΔF_{pk} = 9 MHz)	ANALYTICAL MODEL* (ΔF_{pk} = 8.75 MHz)
N-MAC		
$(S/N)_\ell$	30.1	31.8
$(S/N)_{U,V}$	26.7	28.0
5:4 Luminance		
$(S/N)_\ell$	32.8	32.6
$(S/N)_{U,V}$	28.1	29.0
3:2 Luminance		
$(S/N)_\ell$	30.1	30.2
$(S/N)_{U,V}$	30.4	31.8

* Chrominance filter: 1.5 dB at 1.2 MHz C/N = 10.8 dB; no PE/DE, no weighting.

GENERAL APPROACH TO COMBINED *S/N* DUE TO THERMAL NOISE AND DISTORTION DUE TO SPECTRAL TRUNCATION

The simulations measure the total mean square error, $\overline{\epsilon_T^2}$, on the composite output video waveform and compute an output S/N as the reciprocal of this quantity. The unweighted output S/N is then considered to be a combination of thermal noise and distortion, as

$$(S/N)_T = \{(S/N)_{TH}^{-1} + (S/N)_{FT}^{-1}\}^{-1} \quad . \tag{21}$$

It is postulated that $(S/N)_{FT}$ can be estimated as the fraction of the transmitted RF spectrum lost due to truncation by the channel filters. This fraction is a

function of the transmission format, the test pattern, the pre-emphasis function, the convention for modulating the transmitter (AC or DC coupling), the peak frequency deviation utilized, and the bandwidth of the transmission channel.

The impact of AC *vs* DC coupling is illustrated in Figure 21, which shows the waveforms into the FM modulator and the approximate power density spectra when a black-to-white transition varies around the symmetrical situation in the center, where the picture is 50-percent white and 50-percent black. With AC coupling, the mean is in effect removed from the video waveform, and the peak voltage value (in either the positive or the negative direction) is selected and scaled to produce the correct peak frequency deviation, ΔF_{pk}, of the modulator. With DC coupling, the 0-V video (black) produces $-\Delta F_{pk}$, and 1-V video (white) produces $+\Delta F_{pk}$ without regard to average picture content. For symmetrical picture information, as shown in the center of Figure 21, the mean is 0.5 and both AC and DC coupling give the same waveform into the modulator, and therefore the same transmitted spectrum. For picture information with an average video level different than 0.5, the two formats will give different modulating waveforms and different spectra when scaled to give the same ΔF_{pk}. The DC-coupled format could be more vulnerable to the effects of filter truncation for full-scale asymmetrical video waveforms because this format tends to keep the RF channel filled by the transmitted spectrum.

As peak frequency deviation is increased for TV transmission over the band-limited channel, the output signal-to-thermal noise ratio increases because of an increased FM-improvement factor $(\Delta F_{pk}/\gamma_i f_m)^2$. However, this improvement would be accompanied by a decrease in $(S/N)_{FT}$ as more of the transmitted spectrum is truncated by the channel filters. Since this filter truncation distortion depends on the picture content, it is only partly correct to classify it as independent "noise" and combine it with thermal noise, as in equation (21).

Figure 22 shows the general tradeoff of *S/N vs* ΔF_{pk} for N-MAC. The example illustrates the procedure that has been used to examine the tradeoff between noise and distortion as ΔF_{pk} is varied. For the luminance portion of the output N-MAC waveform, output *S/N* increases with ΔF_{pk}, as shown by the solid curve in the figure. Two other curves are plotted for the case where *S/N* decreases rapidly with ΔF_{pk}. These curves indicate that more of the transmitted spectrum (from Figure 19) falls outside of the assumed channel bandwidth of 24 MHz as ΔF_{pk} increases. When pre-emphasis is used, the transmitted spectrum is more constrained so that filter truncation loss is expected to be less severe.

Combining thermal noise and filter truncation distortion into a combined *S/N* using equation (21) gives the tradeoff curves shown in Figure 22. These

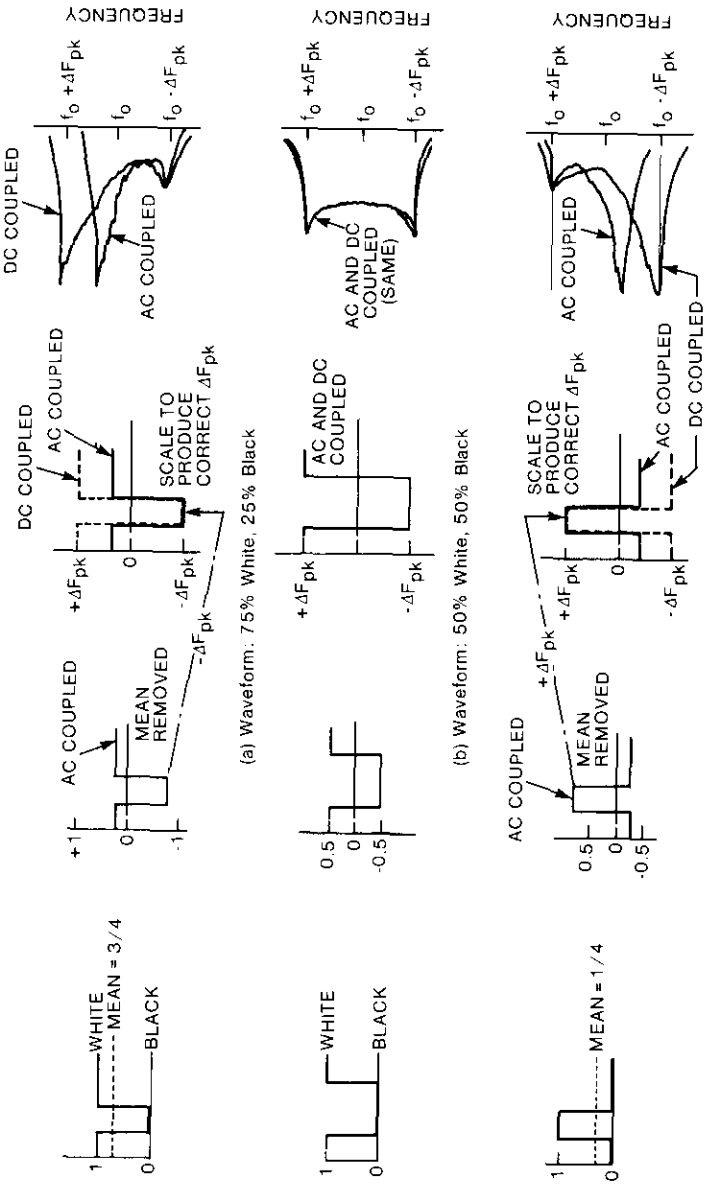

Figure 21. *Examples of Spectra Produced With AC- and DC-Coupled Waveforms*

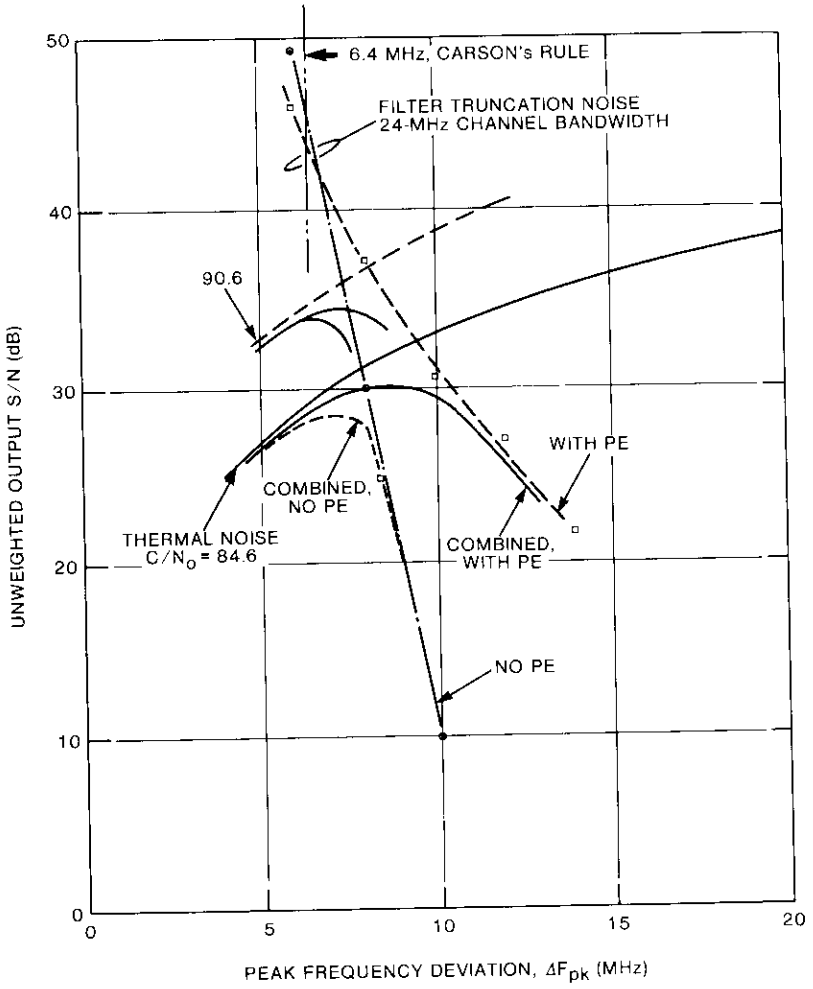

Figure 22. *Combination of S/N Thermal Noise and Filter Truncation Distortion (color bar with DC coupling)*

curves indicate a rather abrupt optimum with no pre-emphasis, giving peak frequency deviation of approximately 7 MHz. With pre-emphasis, combined performance is less sensitive to ΔF_{pk} and an optimum occurs at about 8.5 to 9 MHz.

The tradeoff obtained will depend on the design-point value of C/N_o; the example in Figure 22 uses C/N_o = 84.6 dB-Hz. If C/N_o is higher (for example, by 6 dB), the "optimum" value of ΔF_{pk} is lower to allow less filter-truncation distortion to be combined with the less-noisy picture.

SIMULATED *S/N* RESULTS

The general procedure outlined in the previous section was applied to the three transmission formats, first using luminance *S/N* estimates. Both color-bar and multiburst test patterns were used.

A series of simulations were made to exercise the program with the new test pattern routines. The color-bar patterns and the multiburst patterns were used to modulate the transmitter, with AC coupling and with peak frequency deviations of 6.4, 7.8, 10, 12, 14, and 16 MHz. Power density spectra were obtained which were then integrated to obtain the fraction of power outside of a particular band that is lost due to filter truncation. These results are shown in Figure 23, which plots the quantity $10 \log_{10} (\eta^{-1})$, where η is the fraction of power outside of a bandwidth of 23.9 MHz. The results are sensitive to the assumed channel bandwidth, as shown in Figures 24 and 25, which plot the same results for channel bandwidths of 25.8 and 27.7 MHz, respectively.

Note in Figure 23 that because the color-bar spectra are tightly constrained, they yield small values of η (high values of *S/N*) at a channel bandwidth of 24 MHz. As ΔF_{pk} is increased, more power falls outside of the 24-MHz band, as indicated by the downward slope of the curves. For the unpre-emphasized color-bar pattern, the MAC power density spectra tends to be a rectangle with a width of $\Delta F_{pk\text{-}pk}$, so that the fraction of power lost outside of a rectangular bandwidth, B, can be approximated very roughly as

$$\eta = 0 \qquad , \Delta F_{pk\text{-}pk} < B$$

$$\eta = 1 - B/\Delta F_{pk\text{-}pk}, \ \Delta F_{pk\text{-}pk} \geq B \quad .$$

For example, if B = 24 MHz and $\Delta F_{pk\text{-}pk}$ = 26 MHz, then a fraction 1 − (24/26) = 1/13 of the power density is truncated by the channel. In this case, the fraction 1/13 gives an approximate signal-to-truncation-noise ratio of $10 \log_{10}(\eta^{-1}) \approx 11$ dB.

In Figure 23, this general behavior is noted for peak frequency deviations of 15 or 16 MHz. Signal-to-truncation-distortion ratios are less than 10 dB and correspond to the fraction of power that falls outside of bandwidth B, based on the simple model that the spectral density has a rectangular shape. With this model, η decreases rapidly as ΔF_{pk} decreases through 12 MHz for the color-bar waveform. For the multiburst modulating waveform, the RF spectrum is spread much more so that distortion is less sensitive to ΔF_{pk} although it has a much higher initial level.

In each of these three figures, curves are drawn for *S/N* due to thermal noise (C/N_o = 84.6 dB-Hz), indicating the improvement to be expected as

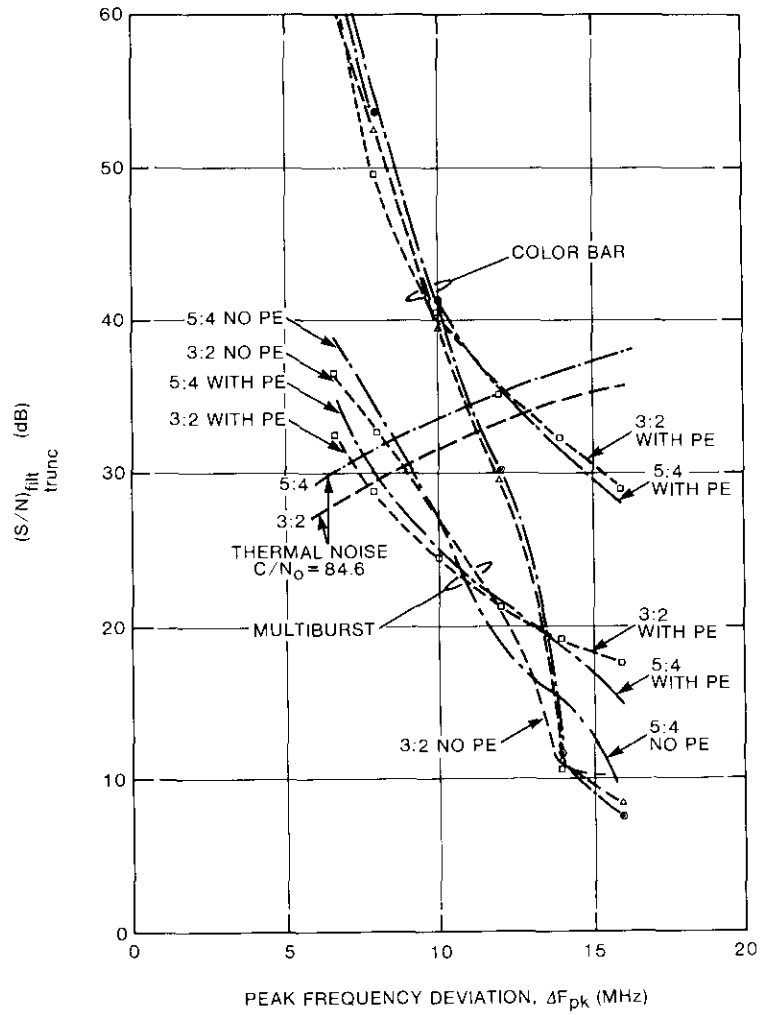

Figure 23. $(S/N)_{filt\ trunc}$ *vs Peak Frequency Deviation: 23.9-MHz Channel Bandwidth With AC Coupling*

ΔF_{pk} is increased. Although the combinations of the two *S/N*s are not drawn, the intersections of the thermal-noise curves with the filter-truncation-distortion curves give a good indication of the tradeoff as ΔF_{pk} is varied.

In all of the figures, differences in filter-truncation distortion between the two compression ratios of 5:4 and 3:2 are extremely small. However, large differences are noted in the sensitivity to ΔF_{pk} for the unpre-emphasized *vs*

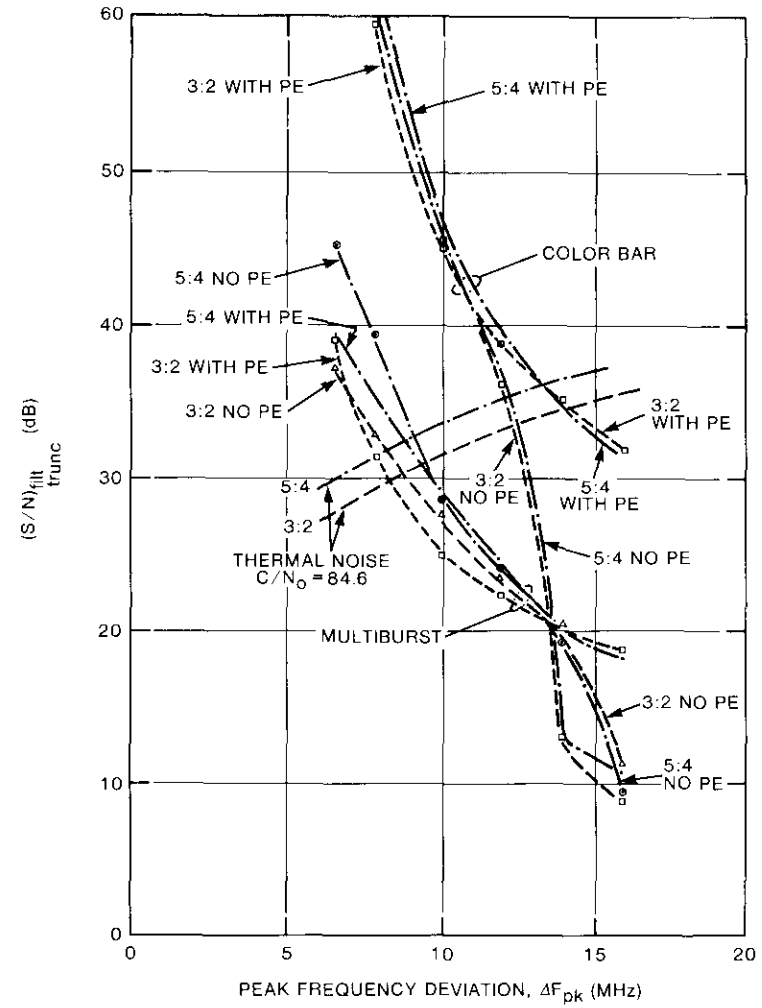

Figure 24. $(S/N)_{filt\ trunc}$ *vs Peak Frequency Deviation: 25.8-MHz Channel Bandwidth With AC Coupling*

the pre-emphasized color bar and, as expected, between the multiburst pattern and color bar. At a channel bandwidth of 24 MHz, crossover peak deviations occur at about 7 to 7.5 MHz peak for the pre-emphasized multiburst and at 8.5 to 9 MHz peak without pre-emphasis. For the color-bar pattern, a sharp peak in performance occurs in the region ΔF_{pk} = 10 to 11 MHz, which is the same for both systems when pre-emphasis is not used. With pre-emphasis, the crossover point moves to 12 to 13 MHz for the color-bar.

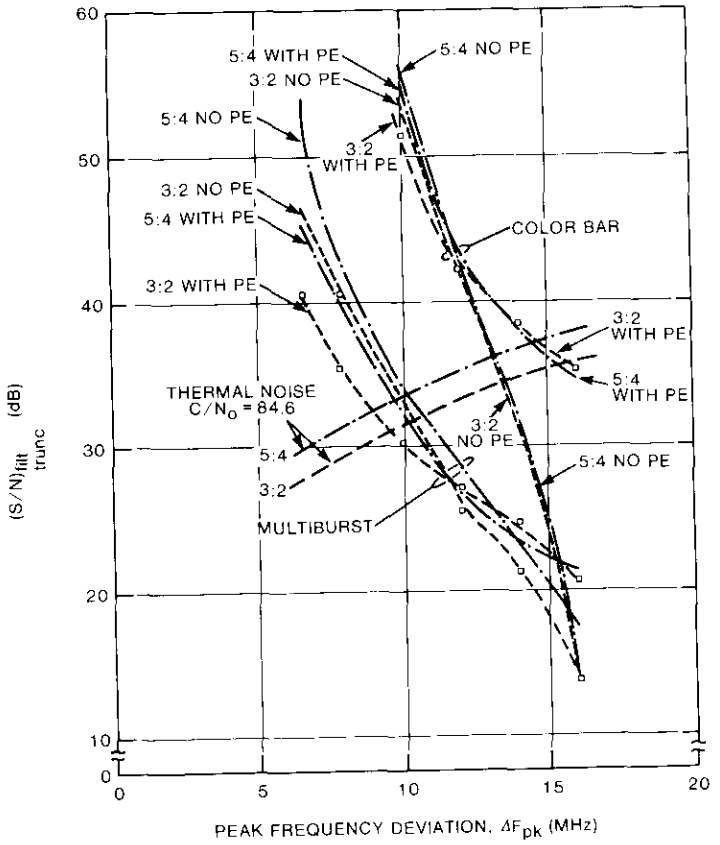

Figure 25. $(S/N)_{filt\ trunc}$ *vs Peak Frequency Deviation: 27.7-MHz Channel Bandwidth With AC Coupling*

As indicated by Figures 24 and 25, these results are somewhat dependent upon assumed channel bandwidth. The assumption that equivalent channel rectangular bandwidth is 24 MHz may be overly conservative. Increasing this bandwidth to 25.8 MHz moves all of the crossover deviations to higher values. A still larger channel bandwidth of 27.7 MHz in Figure 25 produces crossover deviations of 9 to 10 MHz peak for the multiburst pattern, 13 MHz peak for the unpre-emphasized color bar, and approximately 15 MHz peak for the pre-emphasized color bar.

These results are for AC coupling which, as noted earlier, may be slightly less sensitive to overdeviation for the color-bar modulating waveform, which

is slightly asymmetrical. The combining of thermal noise and filter-truncation distortion to arrive at optimum peak frequency deviation values can define general operating regions and allow relative performance comparisons to be made. Such a final summary is shown in Figure 26, which compares 5:4 and 3:2 systems for color-bar modulation. The combined performance is more sensitive to overdeviation when no pre-emphasis is used. With de-emphasis, broad optima are predicted. At the larger values of ΔF_{pk}, it is likely that performance degradation will be dominated by the impulsing that begins to occur at transitions due to signal envelope collapse [23].

Figure 27 shows preliminary results with DC coupling, and with filter truncation distortion estimates taken from Figures 18 through 20. Comparing

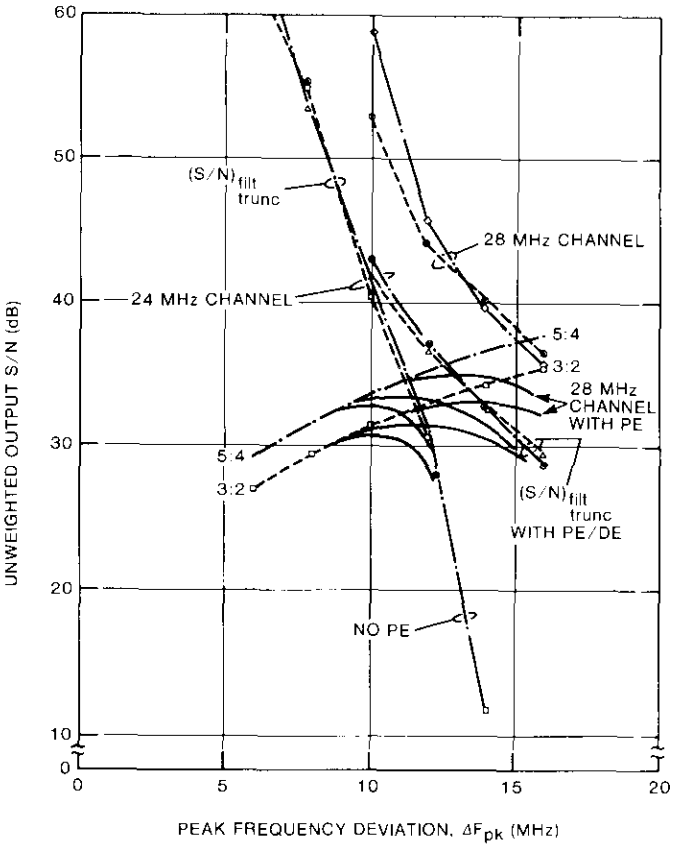

Figure 26. *Combined S/N for Color Bar (C/N_o = 84.6 dB-Hz)*

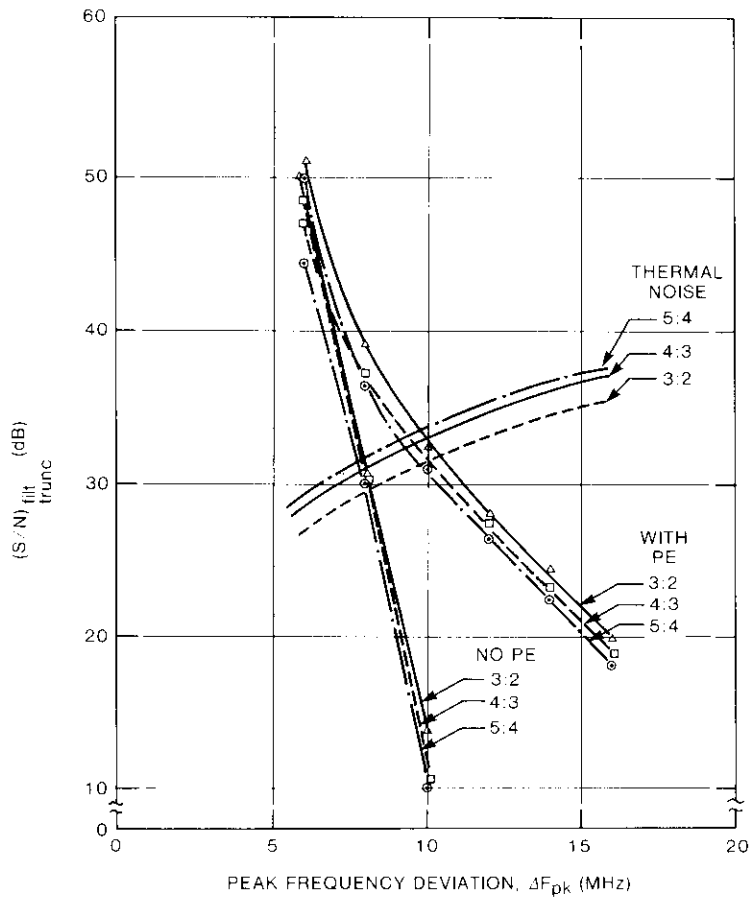

Figure 27. $(S/N)_{\substack{filt \\ trunc}}$ *vs Peak Frequency Deviation: 23.9-MHz Channel Bandwidth With DC Coupling*

these results with the AC-coupled results in Figure 23 reveals an increase in the sensitivity to overdeviation, as expected.

With these initial simulation results establishing the trends to be expected, a final set of simulation runs were made to test the ability of the simulation program to isolate filter truncation noise from thermal noise and to compute separate overall luminance and chrominance *S/N*s. For these experiments, both color-bar and monochrome multiburst test patterns were used with peak frequency deviations, ΔF_{pk}, varied from 7 to 11 MHz. The modulator was AC-coupled for these experiments. The results are given in Table 6 and are

TABLE 6. ADDITIONAL SIMULATION RESULTS WITH THE COMPLETE MODEL INCLUDING GAUSSIAN CHROMINANCE FILTER: *S/N* (dB) UWEIGHTED FOR ΔF_{pk} = 7, 9, AND 11 MHz

	System 1 4:3; 4:1			System 2 5:4; 3.75:1			System 3 3:2; 3:1		
Component	7 MHz	9 MHz	11 MHz	7 MHz	9 MHz	11 MHz	7 MHz	9 MHz	11 MHz
Color Bar									
$(S/N)_{\substack{filt \\ trunc}}$	41.0	38.8	37.7	41.5	39.3	38.2	46.5	43.4	41.1
C/N = 40.9									
$(S/N)_Y$	58.6	61.1	63.1	60.0	62.6	64.4	58.2	60.7	62.5
$(S/N)_U$	54.9	57.1	59.5	55.8	58.3	60.4	58.8	61.5	63.3
C/N = 10.8									
$(S/N)_Y$	28.4	30.1	32.1	30.1	32.8	34.1	27.8	30.1	32.5
$(S/N)_U$	24.5	26.7	29.3	25.7	28.1	29.7	28.1	30.4	32.8
Multiburst									
$(S/N)_{\substack{filt \\ trunc}}$	42.1	38.2	35.2	40.8	36.6	33.3	39.3	35.2	32.2
C/N = 40.9									
$(S/N)_Y$	56.9	59.3	60.9	60.5	62.6	64.0	58.0	60.7	61.5
C/N = 10.8									
$(S/N)_Y$	27.0	28.8	30.6	29.9	31.9	33.4	27.9	29.7	32.1

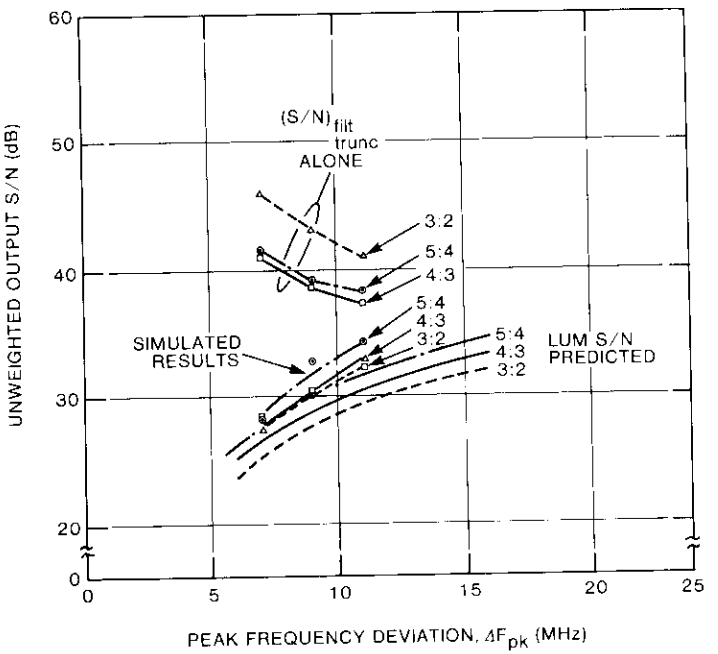

Figure 28. *Comparison of Simulated Results to Predicted Results*

plotted in Figure 28 to compare luminance output *S/N* with the predicted results for C/N = 10.8 dB. Agreement is reasonably good on a relative basis compared to the theoretical predictions.

Summary and conclusions

The analytical results presented show that luminance output *S/N*s are inversely proportional to the third power of luminance compression ratio. For compression ratios of 5:4, 4:3, and 3:2, weighted, de-emphasized luminance *S/N*s of 43.6, 42.8, and 41.2 dB, respectively, are estimated for 75-percent color bars, with ΔF_{pk} = 8.75 MHz for all three systems and C/N_o = 84.6 dB-Hz (the design point used for all calculations). Improvement due to de-emphasis and subjective weighting combined is 11 dB for the three systems. Alternatively, if the three systems are overdeviated by 3 dB relative to Carson's-rule bandwidths, yielding ΔF_{pk} values of 9.55, 9.05, and 8.06 MHz peak, luminance *S/N*s are 44.4, 43.1, and 40.5 dB, respectively.

Output *S/N*s for the individual *U* and *V* output channels depend on the bandwidth assumed for the Gaussian chrominance-channel filter. For a filter with a 3-dB bandwidth of 1.2 MHz at the receiver, *S/N*s for the individual

U and *V* output channels are estimated as 42.6, 40.1, and 39.8 dB for compression ratios of 3:1, 3.75:1, and 4:1, respectively, with de-emphasis and subjective weighting. The improvement due to weighting and de-emphasis varies with the compression ratio (and chrominance bandwidth), but is between 5 and 6 dB for the three values cited above.

The overall conclusions from this comparison can be summarized as follows. The luminance output *S/N* for MAC can be predicted accurately from FM equation (10).

The *S/N* on the *U* and *V* color-difference channels can likewise be accurately predicted using the procedure outlined. Because alternate *U/V* lines are reconstructed by interpolation at the receiver, the interpolated line will have a 3-dB higher *S/N* than the uninterpolated line. This difference was confirmed by laboratory measurements [26]. On average, this interpolation of alternate lines gives approximately a 1.25-dB improvement in the *S/N* of the individual *U* and *V* components. Thus, the formation of a hypothetical composite chrominance *S/N* as $[(S/N_U)^{-1} + (S/N)_V^{-1}]^{-1}$ gives an *S/N* that is approximately 1.75 dB less than the average *S/N* of the individual, uninterpolated *U* and *V* components. This composite chrominance *S/N* is not measurable in an actual system.

The calculation of individual color-component *S/N* values, using the procedure presented, gives *R, G, B S/N* values that are a function of luminance and *U* and *V S/N*s. Again, these results agreed closely with the laboratory measurements presented in Reference 26.

A model has been hypothesized that overall transmission *S/N* can be characterized as a combination of thermal noise and filter truncation distortion. This simplified model gives the general trend in output quality as peak frequency deviation is increased for the bandwidth-limited channel. The relationship approximately illustrates the tradeoff between improved thermal noise performance with increasing ΔF_{pk} and increased waveform distortion. This hypothesized model does not account for the subjective differences between thermal noise and filter truncation distortion.

Acknowledgments

The author wishes to thank many of his colleagues for their support and help during this work. First, R. Gibbons and D. Wells supported the work and provided useful inputs and suggestions. Discussions with A. Gatfield, R. Garlow, and N. Becker were helpful in developing the noise model. The assistance of A. Shenoy, who developed the television simulation program, made modification of the program to handle different compression ratios and independent luminance/chrominance filtering easier. Finally, L. Mikisits and L. White obtained the simulation results.

References

[1] K. Lucas and M. D. Windram, "Direct Television Broadcasts by Satellite, Desirability of a New Transmission Standard," Independent Broadcasting Authority, Report 116/81, September 1981.

[2] "MAC—An Enhanced Television Signal Format for Satellite Broadcasting," Independent Broadcasting Authority, *Technical Review*, November 1981.

[3] K. Lucas and M. D. Windram, "Standards for Broadcasting Satellite Services," Independent Broadcasting Authority, *Technical Review*, No. 18, March 1982.

[4] M. D. Windram, G. Tonge, and R. Morcom, "MAC—A Television System for High Quality Satellite Broadcasting," IBA Experimental Development Report 118/82, August 1982.

[5] C. W. Rhodes, "Time Division Multiplex of Time Compressed Chrominance for a Compatible High-Definition Television System," *IEEE Transactions on Consumer Electronics*, Vol. CE-28, No. 4, November 1982, pp. 592–603.

[6] A. A. Goldberg, R. H. McMann, and J. P. Rossi, "A Two Channel Compatible HDTV Broadcast System," CBS Technology Center Report 8/83-A, July 1983.

[7] J. P. Rossi, A. A. Goldberg, and R. H. McMann, "A Compatible HDTV Broadcast System," NAB Engineering Conference, Las Vegas, Nevada, 1984, *Proceedings*, pp. 306–314.

[8] M. Bouchard and K. Lucas, "New Television Services on Broadcasting Satellites," AIAA 10th Communications Satellite Systems Conference 84-0665, Orlando, Florida, March 1984, *Collection of Technical Papers*, pp. 91–99.

[9] G. Chouinard and J. N. Barry, "NTSC and MAC Television Signals in Noise and Interference Environments," *SMPTE Journal*, Vol. 93, No. 10, October 1984, pp. 930–942.

[10] J. D. Lowry, "B-MAC: An Optimum Format for Satellite Television Transmission," *SMPTE Journal*, Vol. 93, No. 11, November 1984, pp. 1034–1043.

[11] C. W. Rhodes, "A Tutorial on Improved Systems for Color Television Transmission by Satellite," *IEEE Transactions on Broadcasting*, Vol. BC-31, No. 1, March 1985, pp. 1–9.

[12] "Satellite Transmission of Time Multiplexed Analog Component (MAC) Television Signals," CCIR Doc. USSG 10-115, and 85/21 85/23, May 1985.

[13] J. D. Lowry, "The Evolution of B-MAC into a Fully Compatible EDTV System," Second Annual HDTV Colloquium, Ottawa, Canada, May 1985.

[14] J. E. Kadish, "A Chip-Set for B-MAC," *International Broadcast Engineering*, Vol. 16, No. 202, May 1985, pp. 35–42.

[15] C. W. Rhodes, "The Further Evolution of the B-MAC Signal Format or HDTV Broadcasting," Second Annual HDTV Colloquium, Ottawa, Canada, May 1985.

[16] C. W. Rhodes and J. D. Lowry, "The B-MAC Signal Format as Applied to Enhanced 525-Line TV Systems and to HDTV," ICCE, Chicago and ATSC T3/91, June 1985.

[17] C. W. Rhodes, "Extensions of the B-MAC Format to HDTV," 20th International Electronics Convention, Melbourne, Australia, October 1985.

[18] K. Lucas, "B-MAC: A Transmission Standard for Pay DBS," *SMPTE Journal*, Vol. 94, No. 11, November 1985, pp. 1166–1172.

[19] "The Conclusion and Experiment of the S-A B-MAC Format, 'EURO 625'," FTZ No. 632-01, December 1985.

[20] "The Scientific Atlanta B-MAC Video System Tests," British Telecom International, Report BTI/SSZ.1.1, December 1985.

[21] CCIR, "Television Standards for the Broadcasting Satellite Service," Report AA/10-11(MOD F), XVIth Plenary Assembly, Geneva, 1986, Vol. XI.

[22] CCIR, "Satellite Transmission of Multiplexed Analogue Component (MAC) Vision Signals," Report AB/10-11(MOD-F), XVIth Plenary Assembly, Geneva, 1986, Vol. XI.

[23] L. C. Palmer and A. Shenoy, "Simulation of TV Transmission Over the Communications Satellite Channel," *IEEE Transactions on Communications*, Vol. COM-34, No. 2, February 1986, pp. 188–199.

[24] P. L. Bargellini, ed., "The INTELSAT IV Communications System," *COMSAT Technical Review*, Vol. 2, No. 2, Fall 1972, pp. 437–572.

[25] J. M. Barstow and H. N. Christopher, "The Measurement of Random Video Interference to Monochrome and Color Television Pictures," *AIEE Transactions*, Pt. 1: Communication and Electronics, Vol. 81, No. 63, November 1962, pp. 313–320.

[26] A. Gatfield, private communication.

[27] A. Gatfield, private communication.

[28] B. W. Lindgren, *Statistical Theory*, New York: MacMillan, 1962, p. 174.

Larry C. Palmer received a B.S. from Washington and Lee University and a B.E.E. from Rensselaer Polytechnic Institute, both in 1955, and an M.S. and Ph.D. in Electrical Engineering from the University of Maryland in 1963 and 1970, respectively. From 1955 to 1957, he served in the U.S. Army Signal Corps as an Electronics Officer. Following this, he spent 6 years with the Radcom-Emertron Division of Litton Systems, where he was engaged in the design and development of airborne electronics systems. In 1963, he joined ITT INTELCOM and worked on the military communications satellite system. After the acquisition of INTELCOM by Computer Sciences Corporation in 1965, he was involved in systems analysis, modeling, and simulation related to communications and navigation satellite systems.

Dr. Palmer joined COMSAT Laboratories in 1974 and is presently Principal Scientist in the Communications Techniques Division. During 1979 and 1980, he served as Program Manager for COMSAT's participation in the DARPA SATNET program, and during 1984 and 1985 he was Systems Engineering Project Manager for the NASA Advanced Communications Technology Satellite (ACTS) program under subcontract to RCA. He is a Senior Member of the IEEE, and a member of the IEEE Communications Society, the IEEE Information Theory Group, Tau Beta Pi, and Eta Kappa Nu.

Index: INTELSAT, communication satellites, digital transmission, modulation, coding

Low-complexity coding methods for high-data-rate channels

F. HEMMATI and R. J. F. FANG

(Manuscript received June 27, 1985)

Abstract

Bandwidth- and power-efficient, high-speed, coded octal phase-shift keying (8-PSK) systems are presented. It is shown that coded 8-PSK modulation systems having rates higher than 2/3 and based on a class of periodically time-varying trellis codes (PTVTCs) yield bandwidth efficiencies greater than 1.5 bit/s/Hz, with a power efficiency comparable to or better than that of QPSK systems. Viterbi decoder complexity is comparable to that of a rate 2/3 rather than a general rate k/n code. A construction method to generate a class of PTVTCs of rate $(2P + i)/3P$, where $P \geq 2$ and $1 \leq i < P$, for 8-PSK modulation is described. Optimum Euclidean distance codes of rates 7/9, 5/6, and 8/9 with 4, 8, and 16 trellis states are constructed. It is shown that the class of PTVTCs with a normalized Euclidean free distance $d_f \leq 2$ are maximum-likelihood decodable by using the trellis structure of rate 2/3 codes. Computer simulation results are presented for the performance of rate 7/9 and rate 8/9 codes with 16 states over specific channel environments.

Introduction

Quadrature phase-shift keying (QPSK) is the prevalent modulation technique for digital satellite communications because of its relative efficiency in both power and bandwidth utilization. Typically, the bandwidth efficiency of QPSK is 1.3 and 1.5 bit/s/Hz* in the INTELSAT time-division multiple-access

* Bandwidth efficiency is defined as the number of transmitted bits per second within the allocated bandwidth.

(TDMA) system with and without rate 7/8 Bose-Chaudhuri-Hocquenghem (BCH) coding, respectively. To increase bandwidth efficiency to 1.75 or 2 bit/s/Hz, higher alphabet modulation systems such as octal-PSK (8-PSK) could be used, where each 8-PSK symbol carries 3 bits of information. For a given power, the Euclidean distance between the nearest 8-PSK signal points is 2 sin $\pi/8$, whereas the Euclidean distance between the nearest QPSK signal points is 2 sin $\pi/4$. Consequently, 8-PSK requires more power to achieve the same noise immunity or bit error rate (BER) as QPSK.

To improve power efficiency, these higher alphabet modulation systems can signal at the same symbol rate as the QPSK system, thereby generating 50 percent more channel bits since each 8-PSK symbol contains three channel bits, while each QPSK symbol carries only two. For a given information bit rate to be transmitted, this 50-percent redundancy can be exploited for forward error correction (FEC) coding, thus improving BER *vs* E_b/N_o performance, or power efficiency.

In conventional coding systems, the code is designed to maximize the minimum Hamming distance between the generated codewords at the input of the modulator without taking advantage of the geometry of the modulation signal constellation. In coded modulation techniques, the code and the modulation are selected jointly rather than independently so that the minimum Euclidean distance between codewords at the output of the modulator is maximized, producing an improved overall power efficiency relative to conventional Hamming distance FEC coding techniques. The bandwidth efficiency of the original uncoded signaling is preserved by using the larger signaling alphabet for code redundancy rather than increasing the modulation symbol rate.

Coded modulation techniques have been proposed and extensively investigated for high-data-rate transmission over voiceband telephone channels [1] and over band-limited satellite channels with power constraints [2]-[4]. Although most studies on coded modulation techniques for nonlinear satellite channels have focused on constant-carrier envelope signaling formats such as 8-PSK and 16-ary PSK modulations [4],[5], the application of coded quadrature amplitude modulation to satellite communications has also been investigated [6],[7]. Coded 8-PSK modulation with its constant envelope and relative simplicity of high-speed modem implementation for nonlinear satellite channels is preferable to 16-ary PSK, which requires a fine resolution in order to distinguish among its signal points.

Decoder complexity

Three principal quantities determine the complexity of a rate k/n maximum-likelihood trellis decoder. First, the complexity of branch metric computation, N_b, depends on the number of channel symbols associated with each branch in the trellis. Second, complexity is affected by the number of path metric comparisons at each state, N_c, which are made in order to select the path with best metric value. For the standard Viterbi decoder with a rate k/n code, $N_c = 2^k - 1$, where 2^k is the number of branches out of or into each state. Third, complexity is affected by the number of encoder states, $N_s = 2^m$, where m is the number of binary memory elements in the encoder. Clearly, conventional implementation of a high-code-rate Viterbi decoder, even with a small number of states and operating at high channel symbol rates, is extremely complex. At rate 7/9, the conventional Viterbi decoder requires about $2^7 = 128$ path metric comparisons for each of the $2^m = 2^4 = 16$ states if $m = 4$.

In general, the number of encoder states, N_s, is a BER performance parameter: the larger the N_s, the better the BER performance. However, the number of path metric comparisons required at each state, N_c, depends on the encoder trellis structure. Hence, if the code trellis structure is confined to the simpler trellis structure of a low-rate code, the complexity of the decoder for high-rate codes can be significantly reduced. Punctured convolutional codes, a class of high-rate codes such as rate $(n-1)/n$, are decodable by using the simpler trellis structure of a low-rate code such as rate $1/n$ where only two branches terminate on each state. Punctured convolutional codes and their applications for high-speed decoding are discussed in References 8 and 9.

It would seem that high-rate punctured codes could be applied to coded modulation techniques as well; however, for a high-rate code, each 8-PSK symbol must be decoded by more than one step of the trellis diagram. Thus, computation of optimum metrics for this type of decoding becomes complicated. Although it is possible to devise suboptimum decoding schemes with a suboptimum branch metric computation, the performance degradation could be considerable. Moreover, the Viterbi decoder must operate at an extremely high speed.

Periodically time-varying trellis codes

A rate 2/3 coded 8-PSK modulation system achieves a bandwidth efficiency of 1.5 bit/s/Hz (120 Mbit/s over an 80-MHz allocated channel) and has been extensively studied and analyzed over various channel environments [4]. This paper presents high-rate ($k/n > 2/3$) coded 8-PSK modulation systems based on the class of periodically time-varying trellis codes (PTVTCs) which achieve a bandwidth efficiency greater than 1.5 bit/s/Hz. PTVTCs were investigated by Moser [10], who showed that their performance can be as

good or better than that of time-invariant convolutional codes. Punctured convolutional codes can be considered as a subclass of PTVTCs.

The following sections present a construction method for generating a class of PTVTCs of rate $(2P + i)/3P$, where $P \geq 2$ and $1 \leq i < P$. Optimum Euclidean free distance codes of rates 7/9, 5/6, and 8/9 with 4, 8, and 16 trellis states are generated. It is shown that this class of PTVTCs is maximum-likelihood decodable by using the simpler trellis structure of rate 2/3 codes, where four branches terminate on each state. This property is the major advantage of these codes for high-speed applications.

Potential INTELSAT applications for a 16-state coded 8-PSK system of rate 7/9 include transmission at a 140-Mbit/s information rate for restoration via satellite of the proposed transatlantic telephone (TAT-8) fiber optic cable system in case of failure, and for future trunking services via INTELSAT V 72-MHz transponders. Also, the 16-state coded 8-PSK system of rate 8/9 could be used for possible future high-speed, K_a-band, on-board demodulation/remodulation systems operating at a 200-Mbit/s information rate with a bandwidth efficiency of 2 bit/s/Hz.

Generation of high-rate codes

PTVTCs of rate $(2P + i)/3P$, where $P \geq 2$ and $1 \leq i < P$, are a class of high-rate trellis codes conveniently applicable to 8-PSK signal space coded modulations. This class of PTVTCs is constructed by using a periodically time-varying encoder with period P. One period of the trellis diagram of the generated codes consists of $P - i$ consecutive steps of trellis structure for a code of rate 2/3, followed by i steps of the trellis diagram of a rate 3/3 code.

Figure 1 is a functional block diagram of a periodically time-varying encoder of rate $(2P + i)/3P$. The information bits are input to the encoder two bits at a time (in parallel) through lines x_1 and x_3, with the input to x_2 set to logic zero, and the outputs are taken from lines y_1, y_2, and y_3. This

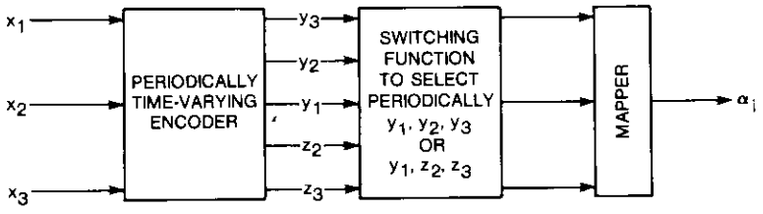

Figure 1. *Functional Block Diagram of a Rate (2P + 1)/3P Periodically Time-Varying Encoder*

process is repeated for $P - i$ consecutive clock periods, where it is assumed that the encoder remains fixed. (This assumption significantly reduces the search effort to find good codes with a large Euclidean free distance.) During the $P - i + 1$, $P - i + 2$, . . . , Pth clock period, three information bits are input to the encoder through lines x_1, x_2, and x_3, and the outputs are taken from y_1, z_2, and z_3. Again, it is assumed that the encoder of rate 3/3 code is fixed. The above encoding process is continued periodically with period P. Finally, the selected 3-tuple encoder output block is mapped into one of the 8-PSK channel symbols. As shown in Figure 2, either Gray mapping or straight binary mapping may be used at this stage because there are corresponding codes for these two mappings that yield an identical code trellis.

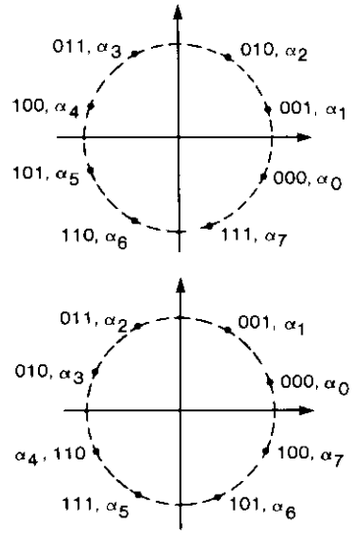

Figure 2. *Straight Binary and Gray Mapping*

For example, a rate 7/9 code is generated by a periodically time-varying encoder of period $P = 3$, where the first 3 input bits in a block of 7 information bits generate a block of 3 output bits. The remaining 4 input bits are divided into blocks of 2 bits and each block generates 3 output bits. Figure 3 shows the structure of one period of a possible trellis diagram for the rate 7/9 code with 16 states. The first step in this diagram corresponds to a rate 3/3 code, and the last two steps can be visualized as the trellis diagram for a rate 2/3 code. Note that for PTVTCs, the encoding rate and the encoder generators are both periodically varying.

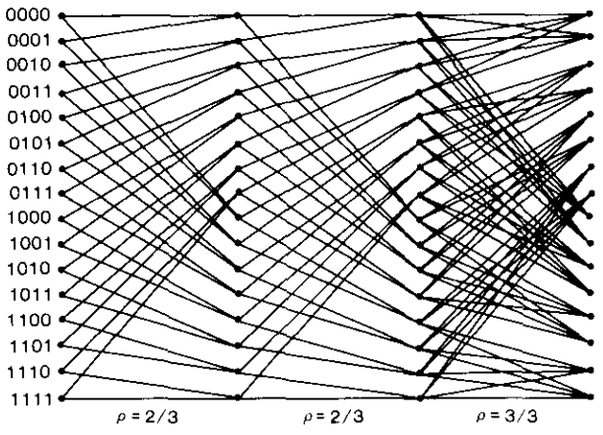

Figure 3. *Trellis Diagram of a 16-State PTVTC of Rate 7/9 With Double-Branch Transitions Between Trellis States*

For a given code rate and a fixed number of encoder states, various types of code trellis structures are possible. For high-speed applications and for simplicity of decoder hardware implementation, it is desired that the structure of the trellis diagram for the time varying code (and hence the decoder operations) remain fixed at every trellis step. In particular, to simplify the addressing process in the Viterbi decoder, the set of predecessor states to a given state must remain fixed at every trellis step. The following realization of encoders of a PTVTC by using a feed-forward shift register generates a code which satisfies this property.

Let $\underline{S}_t = (a_t, a_{t-1}, \ldots, a_{t-m+2}, a_{t-m+1})$ be a binary m-tuple representing the state of a periodically time-varying encoder at time t. Then let the encoder be realized so that $\underline{S}_{t+1}$, the next state of the encoder is

$$\underline{S}_{t+1} = (x^3_{t+1}, a_t, a_{t-1}, \ldots, a_{t-m+3}, a_{t-m+2} + x^2_{t+1}) \quad (1)$$

if the encoder is producing a code of rate 3/3, and

$$\underline{S}_{t+1} = (x^3_{t+1}, a_t, a_{t-1}, \ldots, a_{t-m+3}, a_{t-m+2}) \quad (2)$$

if the encoder is producing a code of rate 2/3 where, at encoding step $t+1$, the binary information input blocks for encoders of rates 3/3 and 2/3 are $(x^1_{t+1}, x^2_{t+1}, x^3_{t+1})$ and (x^1_{t+1}, x^3_{t+1}), respectively.

Equations (1) and (2) show that the set of predecessor states to a given state at rate 2/3 trellis step is a subset of the predecessor states to this state at rate 3/3 trellis step. Note that the trellis structure for PTVTCs represented in Figure 3 satisfies the above property. As an example, the set of predecessor states, α, to state $\underline{S}$ = (0000) at rate 3/3 trellis step is α = {(0000), (0001), (0010), (0011)}, while the two predecessor states to $\underline{S}$ at rate 2/3 trellis step are (0000) and (0001), which belong to α. This property significantly simplifies the hardware implementation complexity of the decoder operating at high speed.

Figure 4 shows a possible realization for the encoder of a 16-state code of rate 7/9. Observe that the most significant bit, y_1, in a block of 3 bits output by the encoder is an uncoded information symbol and specifies a pair of antipodal signals in the phase plane if straight binary mapping is used. In

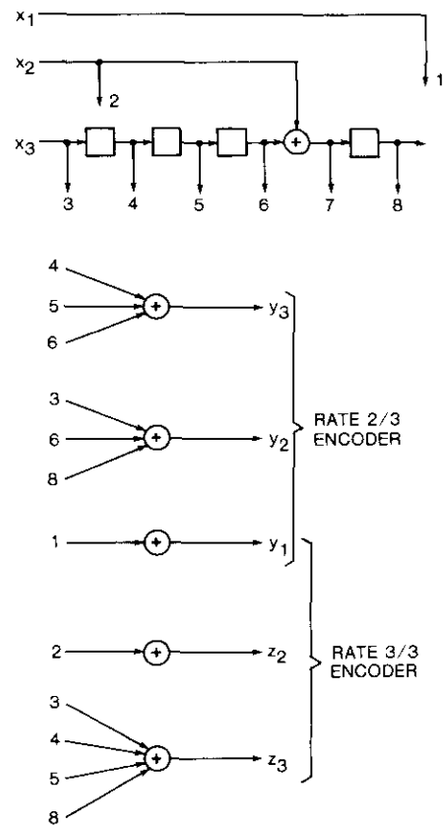

Figure 4. *Encoder for a 16-State Code of Rate 7/9*

terms of the trellis diagram for this class of codes, the transitions between trellis states are by double branches, which reduce the achievable normalized Euclidean free distance of the code to at most 2. However, this should not be a limiting factor, since for a trellis diagram of a high-rate code with a small number of states, codes with normalized free distance greater than 2 are not expected to exist. Moreover, because the double branches reduce trellis connectivity, a code might be generated with a higher free distance which is still less than 2.

Let $d(s_t, s_t')$ denote the Euclidean distance between channel symbols s_t and s_t'. Then, the minimum squared Euclidean free distance, d_f^2, of a code is defined as

$$d_f^2 = \min_{\{s_t\} \neq \{s_t'\}} \sum_t d^2(s_t, s_t')$$

where $\{s_t\}$ and $\{s_t'\}$ are all pairs of channel symbol sequences through the trellis diagram of the code. The normalized free distance of a code is the minimum Euclidean free distance of the code divided by E_s, the energy of a symbol on a circle of radius $\sqrt{E_s}$.

The probability of bit error, P_b, of a coded system with minimum Euclidean free distance, d_f, and soft-decision maximum-likelihood decoding can be approximated by the following asymptotic expression at high signal-to-noise ratios

$$P_b \approx NQ\left(\frac{d_f}{2\sigma}\right)$$

where σ is the noise standard deviation, N is known as the *error coefficient*, denoting the number of nonzero information bits in the set of error events with distance d_f from the correct path, and $Q(u) = (1/\sqrt{2\pi}) \int_u^\infty e^{-x^2/2}\, dx$ is the complementary error function. For a given number of encoder states, an optimum code maximizes d_f while having an error coefficient as small as possible.

Optimum codes of rates 7/9, 5/6, and 8/9

Optimum codes of rate $(2P + i)/3P$ with a small to moderate number of states are constructed by an exhaustive search over the set of all encoders. Note that the conditions for catastrophic error propagation, as stated by Massey and Sain [11], do not directly apply to periodically time-varying encoders. In fact, if the combination of two convolutional encoders yields a catastrophic code, then each component encoder is not necessarily catastrophic. Similarly, it is easy to show that the combination of two catastrophic

encoders might yield a noncatastrophic code. However, the minimum rate of distance growth, d_0, in the set of unmerged paths with the desired path can be readily computed. A code is catastrophic if and only if $d_0 = 0$ [12]. The latter condition is used to test whether a generated code was catastrophic.

The tap connections from different stages of the encoder shift register to output modulo-2 adders can be simply represented by binary $(m + 3)$-tuples $(C_{m+3}, \ldots, C_4, C_3, C_2)$, where $C_i = 1$, for $2 \leq i \leq m + 3$, represents a connection and $C_i = 0$ represents no connection. As an example, the encoder of Figure 4 is completely specified by $R_{23} = (122, 034)$ and $R_{33} = (001, 116)$, where the code generators R_{23} and R_{33} correspond to octal representation of tap connections for encoders of rates 2/3 and 3/3, respectively. The second term in R_{23} or R_{33} generates the least significant bit of the binary 3-tuple output of the encoder, while the uncoded information bit, shown by y_1 in Figure 4, is the most significant bit.

Code generators for the optimum codes of rates 7/9, 5/6, and 8/9 with 4, 8, and 16 states were constructed by exhaustive searching and are shown in Table 1. This table also includes the squared normalized Euclidean free distance and the error coefficient, N, for the obtained codes.

TABLE 1. GENERATOR SEQUENCES (IN OCTAL) FOR SHORT PTVTCs

m	R_{23}	R_{33}	d_f^2	N
		Rate 7/9		
2	22, 04	01, 22	2.32	48
3	46, 14	43, 12	2.90	118
4	122, 034	001, 116	3.48	76
		Rate 5/6		
2	22, 04	01, 26	1.74	18
3	42, 04	01, 46	2.32	96
4	122, 034	001, 136	2.90	158
		Rate 8/9		
2	22, 04	03, 25	1.16	6
3	52, 04	01, 52	1.74	63
4	122, 034	001, 116	1.74	11

Because of limitations on the acceptable hardware complexity of Viterbi decoders operating at high speed, codes with more than 16 states are not generated, even though for lower speed applications the same procedure can be used to generate codes with more than 16 states. Among the high-rate codes presented in Table 1, the 16-state code of rate 7/9 achieves the largest

free distance. While the 8- and 16-state codes of rate 8/9 have equivalent d_f, the error coefficient, N, for the 16-state code is smaller and thus this code is expected to outperform the 8-state code.

The decoding procedure

The high-rate codes constructed in the previous two sections can be maximum-likelihood decoded by using the Viterbi algorithm. Let R_I and R_Q be soft-detected quadrature components of a received symbol at trellis depth t. The metric increments corresponding to trellis branch B at this depth, M_B^t, are computed by correlating the received vector, $R = (R_I, R_Q)$, with the 8-phase signal vector (S_I, S_Q) associated with each trellis branch, as

$$M_B^t = S_I R_I + S_Q R_Q \tag{3}$$

where the quadrature components of the 8-PSK signal constellation, S_I and S_Q, can assume the following values:

$$S_I = \cos \frac{(2I - 1)\pi}{8}$$

$$S_Q = \sin \frac{(2I - 1)\pi}{8}$$

for $1 \leq I \leq 8$.

During each period of the periodically time-varying trellis diagram for the class of codes of rate $(2P + i)/3P$ presented in this paper, there are exactly i trellis steps with the trellis structure of a rate 3/3 code, where eight branches terminate on each state. In the trellis diagram of Figure 3, the eight branches are divided into four double branches. Let $M_{\underline{S}}^{t-1}$ be the path metric value corresponding to state $\underline{S}$ at decoding step $t - 1$. Then, the path metrics $m_{S_1'}^t$ and $m_{S_2'}^t$ for double branches B_1 and B_2, respectively, stemming from the state $\underline{S}$ and terminating on the state $\underline{S}'$, are

$$m_{S_1'}^t = m_{\underline{S}}^{t-1} + m_{B_1}^t \tag{4a}$$

$$m_{S_2'}^t = m_{\underline{S}}^{t-1} + m_{B_2}^t \quad . \tag{4b}$$

In the standard Viterbi algorithm for decoding trellis codes, the path metrics for every branch terminating on the state $\underline{S}'$ are computed according to the above procedure, and the path with the largest metric value is selected as the surviving path at this state. Therefore, the path with the last branch B_2 cannot be a surviving path if

$$m_{S_2'}^t < m_{S_1'}^t$$

or from equation (4)

$$m_{B_2}^t < m_{B_1}^t \quad .$$

For double-branch transitions, this suggests computing the branch metric increment and finding the path metric value of the branch with a corresponding signal symbol of shorter Euclidean distance to the received point. Hence, for updating the metric value of a state with four double branches terminating on it, it is sufficient to compute the metric increment corresponding to only the four branches closest to the received vector in the sense of Euclidean distance. This procedure reduces the number of branch metric computations and path metric comparisons for each state from eight to four. For codes with normalized Euclidean distance $d_f \leq 2$, this reduction in decoder complexity is achieved with no performance degradation if the decoder disregards the presence of intersymbol interference (ISI).

A state, $\underline{S}$, of a trellis with information-bit-to-channel bit rate 3/3 can be reached from four other states $\{\underline{S}_1, \underline{S}_2, \underline{S}_3, \underline{S}_4\}$, while at trellis steps of rate 2/3, the state $\underline{S}$ is reached from only two states $\{\underline{S}_1, \underline{S}_2\}$. In order to make the decoder operate uniformly at every trellis step, it can be assumed that $\underline{S}$ is also reached from $\underline{S}_3$ and $\underline{S}_4$, but at a Euclidean distance of infinity. Unlike the case for regular trellis diagrams for feed-forward encoders with no feedback connections, the information bits corresponding to the transitions from states $\{\underline{S}_1, \underline{S}_2, \underline{S}_3, \underline{S}_4\}$ to state $\underline{S}$ are not all the same. For example, assuming that the uncoded information is a zero, the information input blocks corresponding to the transitions from the set of predecessor states (0000), (0001), (0010), and (0011) to the state $\underline{S}$ = (0000) in Figure 3 are 000, 000, 010, and 010, respectively. For real-time decoders with finite path memory truncation, this nonregularity would not add to decoder complexity because the sequence of decoded trellis states is stored in the decoder output buffers and the decoded information bits can be readily computed.

Performance analysis

The effectiveness of a particular code and mapper for a coded system is conventionally measured in terms of the asymptotic coding gain

$$G_a = 10 \log (\rho d_f^2 / d^2)$$

where d^2 is the minimum squared Euclidean distance for an uncoded modulation signal set, and ρ for a given information source is the ratio of uncoded symbol rate to coded symbol rate. Table 2 summarizes the achievable asymptotic coding gain with respect to uncoded QPSK for optimum codes of rates 7/9 and 5/6 given in Table 1. For optimum codes of rate 8/9, G_a is computed with respect to uncoded 8-PSK.

TABLE 2. ASYMPTOTIC CODING GAIN (dB)

m	RATE 7/9*	RATE 5/6*	RATE 8/9**
2	1.3	0.35	2.50
3	2.3	1.50	4.26
4	3.0	2.60	4.26

* Coding gain over uncoded QPSK.
** Coding gain over uncoded 8-PSK.

The asymptotic coding gains presented in Table 2 are computed as a function of the free distance of the code and symbol rate, disregarding the error coefficient N. For optimum free distance codes of high rate, the parameter N is a rather large number and actual system performance might be inferior to the predicted asymptotic performance.

The 16-state code of rate 7/9 achieves an asymptotic coding gain of 3 dB over uncoded QPSK and is being implemented for possible restoration via satellite in case of failure of the proposed TAT-8 fiber optic cable system and for future trunking services via INTELSAT V 72-MHz transponders. While uncoded QPSK requires transmission at 70 Msymbol/s, rate 7/9 coded 8-PSK achieves transmission of 140-Mbit/s source information at a rate of 60 Msymbol/s. This coded modulation technique not only potentially achieves high power efficiency, as shown in Table 2, but also reduces the channel symbol rate, resulting in a considerable gain in required allocated bandwidth efficiency. The 16-state code of rate 8/9 has been proposed for future K_a-band on-board demodulation/remodulation applications, operating at an information rate of 200 Mbit/s over an allocated bandwidth of 100 MHz. At a channel symbol rate of 75 Msymbol/s, it can potentially achieve an asymptotic power advantage of 4.26 dB with respect to uncoded 8-PSK.

16-state code of rate 7/9

Performance of a coded 8-PSK system using the 16-state code of rate 7/9 on the additive white Gaussian noise (AWGN) channel and in the INTELSAT V environment was evaluated by means of Monte Carlo computer simulations. The simulations were carried out by using a 32-level (5-bit), soft-detection, real-time Viterbi decoder with a path memory truncated to length $T = 25$ trellis steps. For this path truncation, the length of the minimum Euclidean distance path in the set of unmerged paths with the transmitted path is equal to $d_t = 2.01$, which is greater than the Euclidean free distance of the code, $d_f = 1.86$. This unmerged path distance guarantees that, compared to ideal maximum-likelihood decoding, the additional BER due to truncated path memory will be negligible.

Perfect carrier phase symbol timing and code synchronization between the transmitter and receiver were assumed. In the real system, the out-of-synchronization status is detected by either of the following procedures. In the first, the difference between the maximum and minimum values of the path metric functions corresponding to the encoder states at consecutive decoding steps is observed. The difference becomes very small if the system is out of synchronization. In the second procedure, the channel BER for the received sequence is measured by re-encoding the estimated data sequence obtained from the decoder and comparing it with the received symbol sequence, as shown in Figure 5. The measured BER is larger than the expected channel BER if the decoder is not synchronized with the received sequence. Note that, in order to acquire code synchronization for the rate 7/9 code with a period of $P = 3$ 8-PSK symbols, a threefold ambiguity must be resolved.

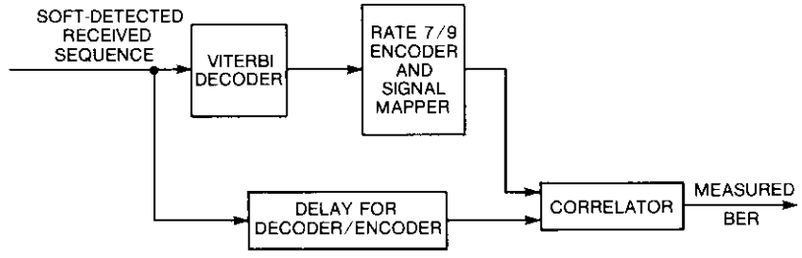

Figure 5. *Block Diagram of BER Measurement Network*

Figure 6 shows the decoded BER, P_b, of the rate 7/9 code on an AWGN channel as a function of E_b/N_o. The theoretical performance of uncoded QPSK on the AWGN channel is also presented as a reference. A coding gain of more than 1 dB over uncoded QPSK is observed at BER $= 10^{-4}$. Because of the excessive time required for the computer simulations to accumulate sufficient error events for statistical reliability, the simulation results were obtained only for BER $> 10^{-4}$. System performance at lower BERs can be estimated by extrapolation.

As an example of the capability of these codes, the channel model shown in Figure 7 was used to estimate the performance of the rate 7/9 code on INTELSAT V C-band transponders. The signal paths M, C, U, and L represent the main channel, co-channel, upper adjacent channel, and lower adjacent channel signal paths, respectively. Rectangular pulse-shape signaling with 16 samples per symbol was employed. The modem filters are square-root Nyquist with 40-percent rolloff, the same as those specified for the current INTELSAT TDMA/QPSK system. The transmit filter includes an aperture

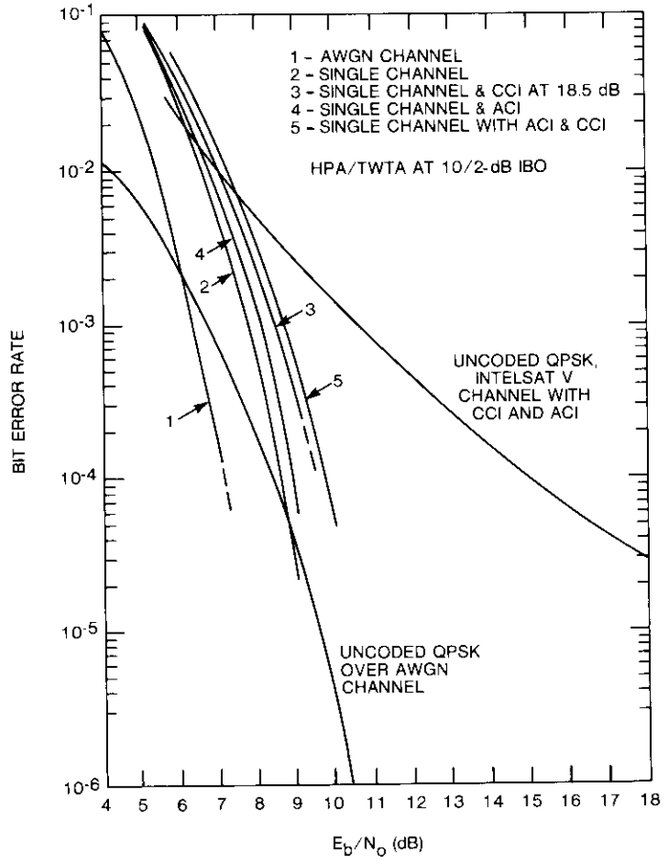

Figure 6. *BER Performance Curves for a 16-State Coded 8-PSK System of Rate 7/9 Over INTELSAT V Channel (Nyquist modem filter with 40% rolloff factor)*

compensation response of the form $(\pi f T_s)/\sin(\pi f T_s)$, where T_s is the duration of one channel symbol. Figure 8 shows the phase transfer characteristics and output power backoff of the high-power amplifiers (HPAs) and traveling wave tube amplifiers (TWTAs) as a function of input power backoff. The co-channel interference (CCI) caused by non-ideal isolation between polarization and the beam for frequency reuse can be modeled by the co-channel path (*C*) in Figure 7, and its strength can be adjusted by the multiplier at the output of the HPA. The upper and lower adjacent channel carrier frequencies are offset by 80 MHz with respect to the main channel.

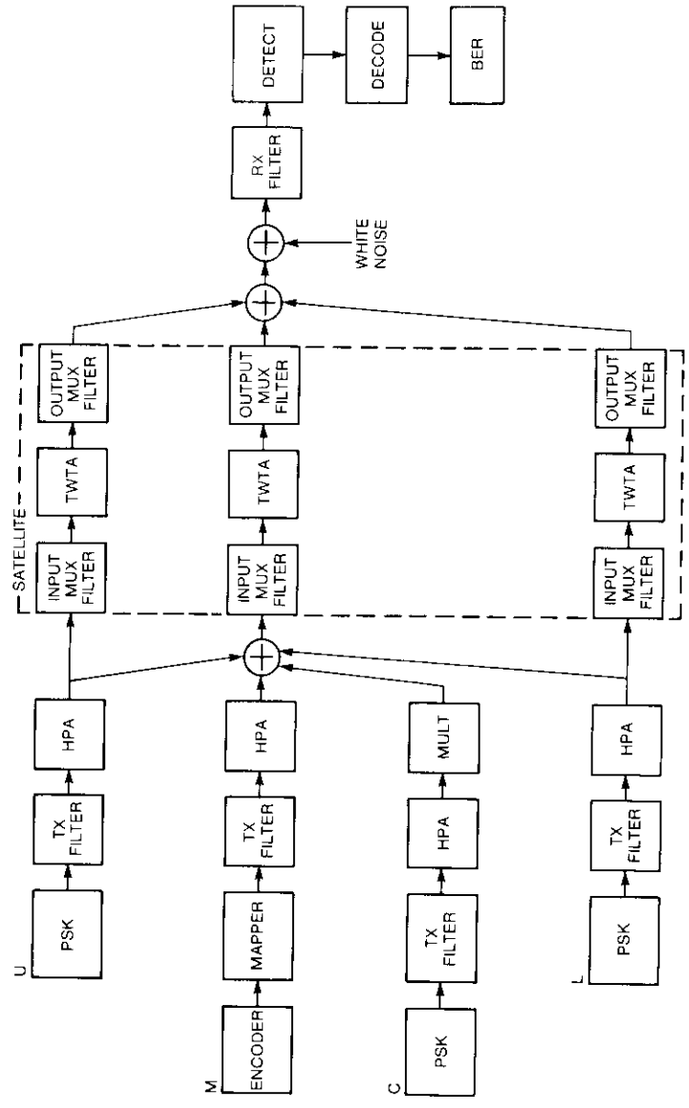

Figure 7. *Generic Model of a System Environment for System Simulations*

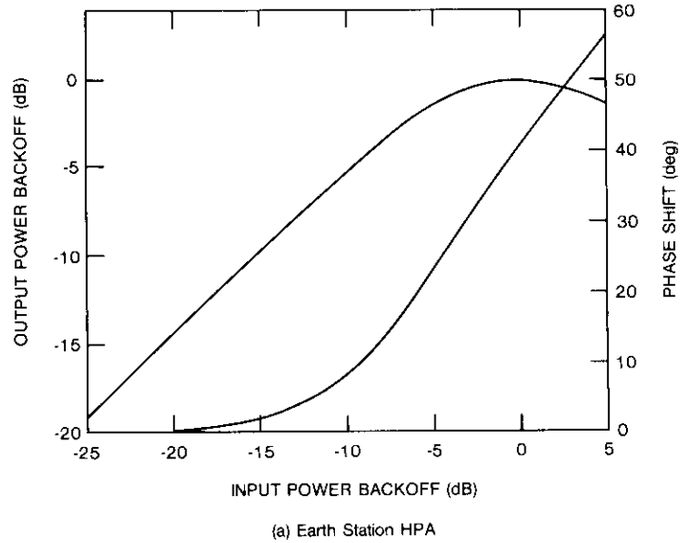

(a) Earth Station HPA

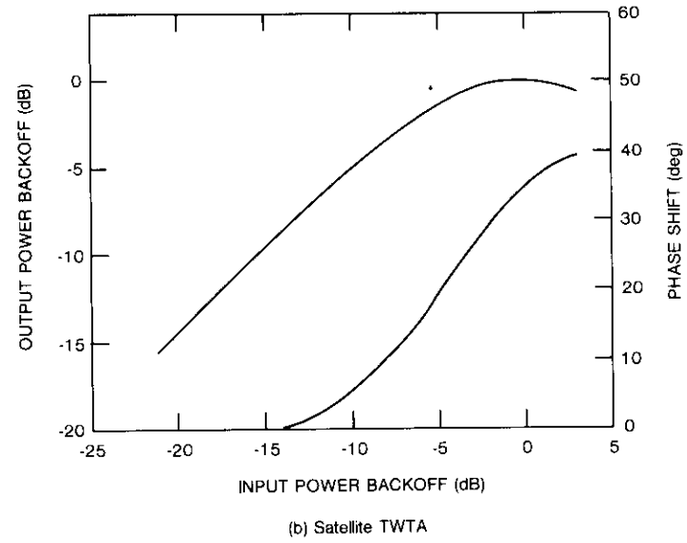

(b) Satellite TWTA

Figure 8. *Nonlinear Response Curves*

The nominal amplitude and group delay responses for the satellite input and output multiplexing filters are shown in Figure 9 and correspond to the typically measured characteristics of INTELSAT V transponder multiplexing filters.

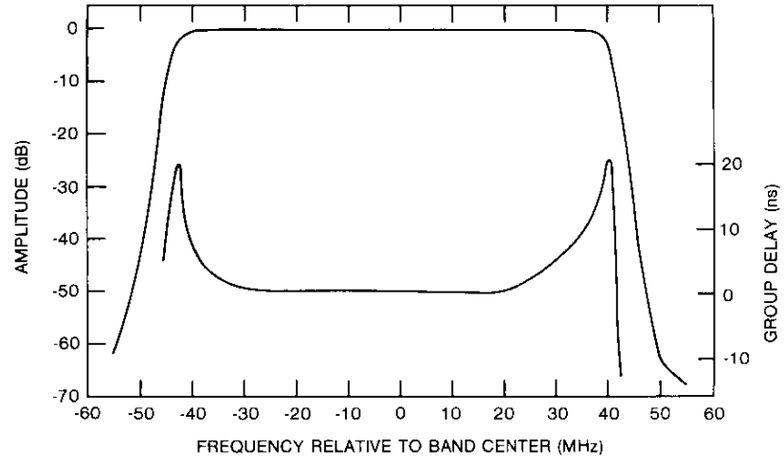

(a) Receive

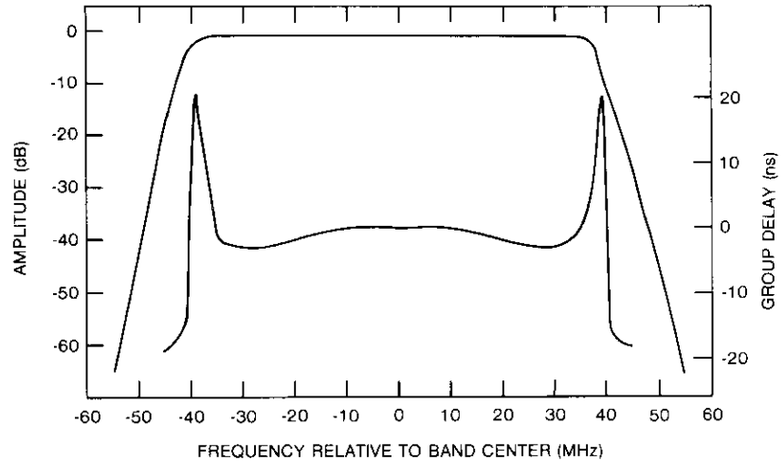

(b) Transmit

Figure 9. *Nominal Amplitude and Group Delay for Satellite Multiplexing Filters*

Monte Carlo computer simulations were carried out to evaluate the performance of the rate 7/9 coded 8-PSK system over the INTELSAT V transponder with CCI at −18.5 dB with respect to the desired carrier power. It was assumed that the HPAs and TWTAs were operating at 10-dB and 2-dB input backoff, respectively (*i.e.*, the same input backoffs specified for the current TDMA/QPSK system). To demonstrate the impact of TWTA nonlinearity and adjacent channel interference (ACI) on system performance, the simulations were also performed for a single-channel case with and without CCI.

From Figure 6, a performance loss of about 2.5 dB is observed for the rate 7/9 coded 8-PSK system over the INTELSAT V channel relative to system performance over the Gaussian channel at BER = 10^{-4}, where 1.2-dB loss is due to HPA and TWTA nonlinearities and intersymbol interference (ISI). The CCI causes about 0.8 dB further loss, and the two adjacent channels degrade system performance by about 0.4 dB.

The performance of the uncoded QPSK operating at 140 Mbit/s over the INTELSAT V channel environment, as shown in Figure 6 with two ACIs and one CCI at −18.5 dB, was also evaluated by computer simulation for comparison. The large performance difference (more than 5 dB) between the uncoded QPSK and rate 7/9 coded 8-PSK is partially due to the considerably more incremental ISI and ACI losses for the QPSK signaling at 70 Msymbol/s, and only partially due to the coding gain against additive noise for the rate 7/9 coded 8-PSK system operating at 60 Msymbol/s. Moreover, additional coding gain is obtainable on the nonlinear channel because the code memory averages the ISI and nonlinearity effects [4].

16-state code of rate 8/9

The BER performance of the 16-state coded 8-PSK system of rate 8/9 over the AWGN channel and over the up-link or down-link channel model (shown in Figure 10) was evaluated by means of Monte Carlo computer simulations. The decoder BER, P_b, over the AWGN channel as a function of E_b/N_o is shown in Figure 11. The theoretical performance curve for uncoded 8-PSK over the

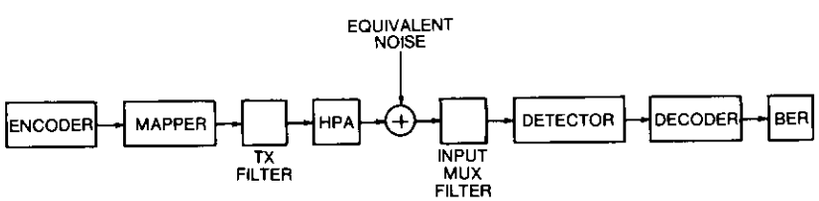

Figure 10. *Channel Model for Simulation of Rate 8/9 Coded Modulation System for On-Board Demodulation Applications*

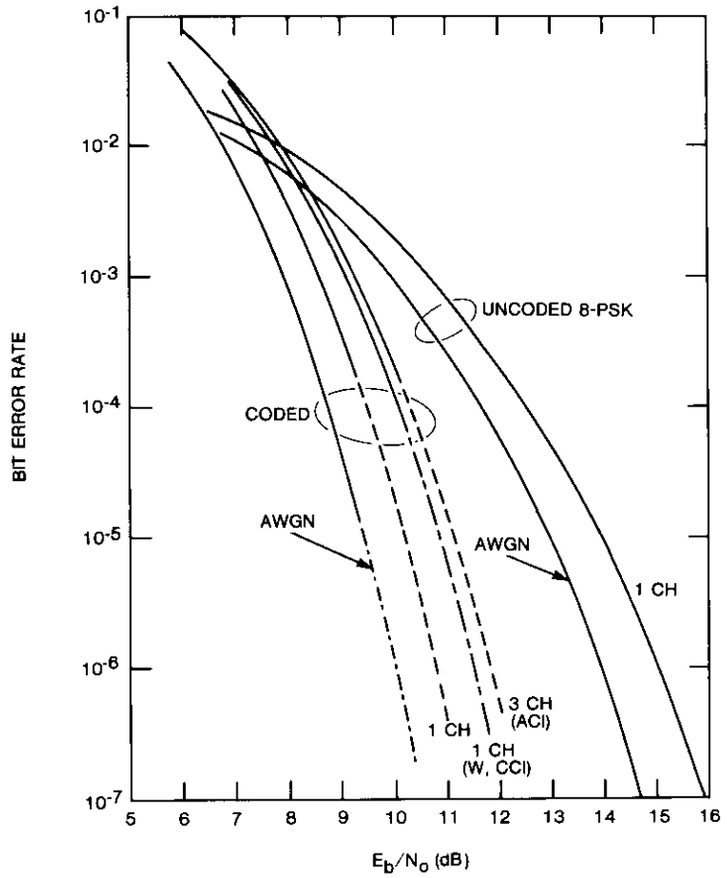

Figure 11. *BER Performance Curves of a 16-State Coded 8-PSK System of Rate 8/9 for On-Board Demodulation Applications*

AWGN channel is also depicted for comparison. Simulation results for low BER require excessive amounts of computer time; therefore, the performance curves shown as dashed lines are extrapolated in this region. Comparison of the two curves reveals an approximate 4-dB asymptotic power advantage, in agreement with the theoretical results shown in Table 2.

In addition to an encoder of rate 8/9 and a signal mapper, the channel model of Figure 10 contains a pulse-shaping Nyquist filter with 33-percent rolloff. Testing of several other rolloff factors showed this factor to be optimum for the transmission of 8-PSK signals at 75 Msymbol/s over the

channel model, with two adjacent channels located at 100-MHz spacing with respect to the center frequency of the main channel. Figure 12 shows the phase transfer characteristics and output power backoff of the considered HPA as a function of input power backoff.

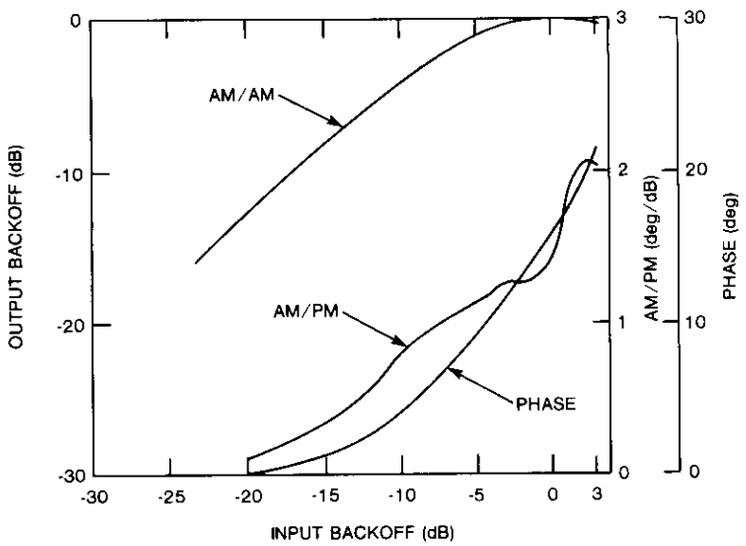

Figure 12. *Phase Transfer Characteristics and Output Power Backoff for HPA Used in the System Simulation Model of Figure 10*

Uncoded 8-PSK modulation achieves transmission of a 200-Mbit/s information source rate at 67 Msymbol/s, while the rate 8/9 coded system requires transmission of 75 Msymbol/s. Here, coding gain is conveniently traded off by increasing the channel symbol rate slightly. This increase is justifiable since, for an adjacent channel spacing of 100 MHz, no significant additional degradation due to ISI or ACI is expected. The channel model of Figure 10 was used to simulate the performance of coded 8-PSK with the rate 8/9 16-state code for the single nonlinear channel. Comparing the performance of coded 8-PSK with that of uncoded 8-PSK reveals a coding improvement of 4.3 dB at 5×10^{-7} BER (Figure 11). Compared to the AWGN channel, the simulated implementation loss for the single nonlinear channel, as given in Figure 11, is 0.8 dB at a BER of 10^{-4}.

In addition, Figure 11 shows the simulation results for the performance of the coded system when there are two adjacent carriers, each equal in power to the desired carrier. The performance degradation due to ACI is approximately 0.8 dB at a BER of 10^{-4}, indicating (by curve extrapolation) that the degradation is not more than 1 dB at a BER of 5×10^{-7}. HPA output filtering should be employed to limit the effect of ACI in a faded desired up-link channel. Computer simulations show that HPA filtering yields good results for the case where the desired channel is faded at K_a-band by about 20 dB with respect to the adjacent channel.

Figure 11 also presents simulation results for CCI with a power ratio of $C/I = 20$ dB for the case where there is less than 1-dB loss at a BER of 10^{-4}.

Conclusions

It has been shown that the class of PTVTCs of rate $(2P + i)/3P$, where $P \geq 2$ and $i < P$, can be applied to construct coded 8-PSK modulation systems that are maximum-likelihood decodable by using the trellis structure of a rate 2/3 code where only four branches terminate on each state. This compares to 2^k branches terminating on each state in the trellis diagram of a standard code of rate k/n. Therefore, decoder complexity can be significantly reduced and decoder speed can be significantly increased, particularly in high-speed implementations such as the 140- or 200-Mbit/s coded 8-PSK applications discussed in this paper.

Optimum coded 8-PSK systems of rates 7/9, 5/6, and 8/9 with 4, 8, and 16 states were constructed by exhaustive searching. The computer simulation results for the 16-state coded 8-PSK system of rate 7/9 over the INTELSAT V 72-MHz transponder operating at a 140-Mbit/s data rate (or at 1.75 bit/s/Hz) show a coding gain of more than 5 dB over uncoded QPSK at a BER of 10^{-4}. This coding gain is only partially attributable to the large Euclidean distance of the rate 7/9 code, and is primarily related to the significant reduction of the ISI and ACI effects associated with the channel symbol rate being lowered from 70 to 60 Msymbol/s.

Computer simulation results were also presented for the 16-state coded 8-PSK system of rate 8/9 over an on-board demodulation/remodulation link. BER performance was evaluated for various channel environments, including ACI and CCI. Significant coding improvement was achieved while realizing a 2-bit/s/Hz bandwidth efficiency.

References

[1] Special Issue on Voiceband Telephone Data Transmission. *IEEE Journal on Selected Areas in Communications*. Vol. SAC-2, No. 5, September 1984.

[2] G. Ungerboeck, "Channel Coding With Multilevel/Phase Signals," *IEEE Transactions on Information Theory*, Vol. IT-28, No. 1, January 1982, pp. 55–67.

[3] R. J. Fang, "A Bandwidth and Power-Efficient Modulation System," *Innovations in Telecommunications*, Part A, New York: Academic Press, 1982, pp. 29–57.

[4] S. A. Rhodes, R. J. Fang, and P. Y. Chang, "Coded Octal Phase Shift Keying in TDMA Satellite Communications," *COMSAT Technical Review*, Vol. 13, No. 2, Fall 1983, pp. 221–258.

[5] S. G. Wilson *et al.*, "Rate 3/4 Convolutional Coding of 16-PSK: Code Design and Performance Study," *IEEE Transactions on Communications*, Vol. COM-32, No. 12, December 1984, pp. 1308–1315.

[6] E. Biglieri, "High Level Modulation and Coding for Nonlinear Satellite Channels," *IEEE Transactions on Communications*, Vol. COM-32, No. 5, May 1984, pp. 616–626.

[7] S. A. Rhodes and P. Y. Chang, "Coded M-ary Modulation for FDMA Satellite Communications," IEEE Global Telecommunications Conference, Atlanta, Georgia, November 1984, *Conference Record*, pp. 726–734.

[8] J. B. Cain, G. C. Clark, and J. M. Geist, "Punctured Convolutional Codes of Rate $(n-1)/n$ and Simplified Maximum Likelihood Decoding," *IEEE Transactions on Information Theory*, Vol. IT-25, No. 1, January 1979, pp. 97–100.

[9] Y. Yasuda *et al.*, "High Rate Punctured Convolutional Codes for Soft Decision Viterbi Decoding," *IEEE Transactions on Communications*, Vol. COM-32, No. 3, March 1984, pp. 315–319.

[10] M. Mooser, "Some Periodic Convolutional Codes Better Than Any Fixed Code," *IEEE Transactions on Information Theory*, Vol. IT-29, No. 5, September 1983, pp. 750–751.

[11] J. L. Massey and M. K. Sain, "Inverses of Linear Sequential Circuits," *IEEE Transactions on Computers*, Vol. C-17, No. 4, April 1968, pp. 330–337.

[12] F. Hemmati and D. J. Costello, "Asymptotically Catastrophic Convolutional Codes," *IEEE Transactions on Information Theory*, Vol. IT-26, No. 3, May 1980, pp. 298–304.

Farhad Hemmati received an M.S.E.E. and Ph.D. from Illinois Institute of Technology in 1973 and 1977, respectively. Since joining COMSAT Laboratories in 1982, he has worked on coding techniques and various signal processing methods for satellite channels. He is currently a Staff Scientist in the Communications Systems Studies group, where his primary research interests are coding, spread spectrum, and multiple access.

Russell J. F. Fang received a B.S.E.E. from National Taiwan University, Taipei, China, in 1962, and an M.S.E.E. and Ph.D. from Stanford University in 1964 and 1968, respectively. From 1964 to 1966, he was a Research Engineer at Stanford Research Institute. Since joining COMSAT Laboratories in 1968, Dr. Fang has been a Member of the Technical Staff, Staff Scientist, and Department Manager, and is currently Associate Director of the Communications Techniques Division. He has authored or co-authored more than 20 papers in professional journals, as well as numerous conference papers. He is a Senior Member of IEEE.

Index: geosynchronous orbit, time division multiple access

A bound on diurnal error in predicted ranges of nearly geostationary satellites*

P. C. KAMMEYER

(Manuscript received November 9, 1983)

Abstract

The orbit of a nearly geostationary satellite may be determined from range observations at two ground stations. Ranges predicted from the determined orbit contain a diurnal error component corresponding to errors in the determined eccentricity and inclination. This paper derives a bound on the diurnal range error. It is shown that diurnal error decreases as the distance between the ground stations used to determine the orbit increases, and that separation in latitude reduces diurnal error more effectively than separation in longitude.

Introduction

The time-division multiple-access (TDMA) technique permits transponders on a synchronous communications satellite to be used with maximum efficiency. In this technique, transmissions from various ground stations are separated on the basis of their different times of arrival at the satellite. Thus, accurate predictions of the ranges from many ground stations to the satellite are required. One method for providing these predictions is to calculate range

* This paper is based on work performed at COMSAT Headquarters under the sponsorship of the International Telecommunications Satellite Organization (INTELSAT). Views expressed are not necessarily those of INTELSAT.

for an estimated orbit using range data from two ground stations well separated in latitude and longitude.

The range of a nearly geostationary satellite from a ground station shows diurnal oscillation. Slabinski [1] has studied the effect of ground station location and the eccentricity and inclination of the satellite orbit on this oscillation. Eccentricity and inclination errors in an estimated orbit similarly give rise to a diurnal error in the predicted range from any ground station to the satellite. The amplitude and phase of this error can be expressed by a complex number. Given values of this complex quantity at the two ground stations used to determine the orbit, its value at any other location may be obtained by an interpolation technique. This technique also permits easy calculation of a bound on the diurnal error.

Basic definitions

First, an earth-oriented rectangular coordinate system XYZ with origin over the equator at synchronous altitude and nominal satellite longitude must be defined. The X-axis points away from the center of the earth, the Y-axis points eastward along the synchronous arc, and the Z-axis points north. Assuming the earth to be a sphere of radius $R = 6{,}378$ km, let A denote the radius of the synchronous orbit (42,164 km). A ground station at geocentric latitude ℓ and longitude ϕ east of the nominal satellite longitude has XYZ coordinates

$$(R \cos \ell \cos \phi - A,\ R \cos \ell \sin \phi,\ R \sin \ell) \quad .$$

Let ρ_N be the range from the station to the satellite's nominal position, the XYZ origin. The station's unit sight vector toward the nominal satellite position, as illustrated in Figure 1, has components

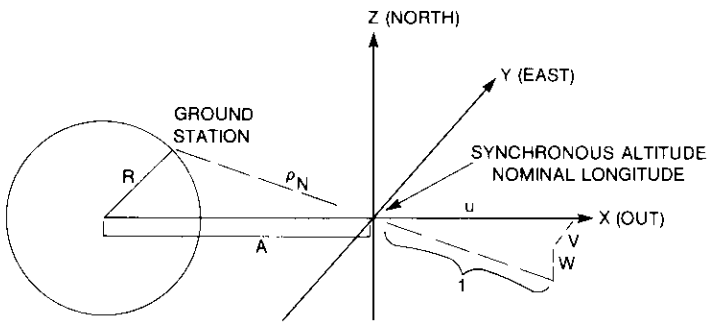

Figure 1. *Definition of Sight Vector*

$$(u, v, w) = \frac{1}{\rho_N}(A - R \cos \ell \cos \phi,\ -R \cos \ell \sin \phi,\ -R \sin \ell) \qquad (1)$$

where $\rho_N = \sqrt{A^2 - 2AR \cos \ell \cos \phi + R^2}$.

Reduction of force to inverse square attraction

The same method used on page 14 of Szebehely [2] may be employed to obtain the equations of satellite motion

$$\frac{d^2}{dt^2} X - 2n_0 \frac{d}{dt} Y - n_0^2 (X + A) = F_X \qquad (2a)$$

$$\frac{d^2}{dt^2} Y + 2n_0 \frac{d}{dt} X - n_0^2\ Y = F_Y \qquad (2b)$$

$$\frac{d^2}{dt^2} Z = F_Z \quad . \qquad (2c)$$

Here F_X, F_Y, and F_Z are the components of applied force per unit mass (which is assumed to depend only on time and satellite position), and n_0 is the rotation rate of the earth in radians per unit time.

Assuming that the estimated orbit is described by equations (2), with force components corresponding to the estimated position, then the errors in the estimated coordinates satisfy, to first order, the linearized equations of motion

$$\frac{d^2}{dt^2}\Delta X - 2n_0 \frac{d}{dt}\Delta Y - n_0^2 \Delta X = \frac{\partial F_X}{\partial X}\Delta X + \frac{\partial F_X}{\partial Y}\Delta Y + \frac{\partial F_X}{\partial Z}\Delta Z \qquad (3a)$$

$$\frac{d^2}{dt^2}\Delta Y + 2n_0 \frac{d}{dt}\Delta X - n_0^2 \Delta Y = \frac{\partial F_Y}{\partial X}\Delta X + \frac{\partial F_Y}{\partial Y}\Delta Y + \frac{\partial F_Y}{\partial Z}\Delta Z \qquad (3b)$$

$$\frac{d^2}{dt^2}\Delta Z = \frac{\partial F_Z}{\partial X}\Delta X + \frac{\partial F_Z}{\partial Y}\Delta Y + \frac{\partial F_Z}{\partial Z}\Delta Z \qquad (3c)$$

It will be shown that only terms in F_X, F_Y, and F_Z which correspond to the inverse square attraction of the earth need to be retained in equations (3). The force per unit mass caused by the gravitational attraction of a point mass M displaced $\vec{r}$ from the satellite is

$$\vec{F} = \frac{GM\vec{r}}{r^3} \qquad (4)$$

where G is the universal gravitational constant. Differentiating,

$$\frac{\partial}{\partial X}\vec{F} = GM\frac{\partial}{\partial X}\left(\frac{\vec{r}}{r^3}\right)$$

$$= \frac{GM}{r^2}\left(\frac{1}{r}\frac{\partial \vec{r}}{\partial X} - 3\frac{\partial r}{\partial X}\frac{\vec{r}}{r^2}\right) \quad (5a)$$

$$\frac{\partial}{\partial Y}\vec{F} = \frac{GM}{r^2}\left(\frac{1}{r}\frac{\partial \vec{r}}{\partial Y} - 3\frac{\partial r}{\partial Y}\frac{\vec{r}}{r^2}\right) \quad (5b)$$

$$\frac{\partial}{\partial Z}\vec{F} = \frac{GM}{r^2}\left(\frac{1}{r}\frac{\partial \vec{r}}{\partial Z} - 3\frac{\partial r}{\partial Z}\frac{\vec{r}}{r^2}\right) \quad . \quad (5c)$$

Substituting the distances and masses of the earth, moon, and sun into equations (5) shows that the magnitudes of the derivatives for sun and moon gravity are less than 0.0002 times those for the inverse square attraction of the earth. Therefore, derivatives of lunar and solar gravity will be omitted from equations (3). Similarly, derivatives of radiation pressure and zonal and tesseral harmonics in the earth's gravitational attraction will be omitted. Only derivatives of the earth's inverse square attraction will be retained.

Solution of linearized equations for inverse square attraction

Since the satellite remains near the geostationary orbit $X = Y = Z = 0$, the derivatives of force components with respect to position components will be replaced by their values on the geostationary orbit. Using equations (5), the linearized equations of motion become

$$\frac{d^2}{dt^2}\Delta X - 2n_0\frac{d}{dt}\Delta Y - n_0^2\Delta X = \frac{GM}{A^2}\left(2\frac{\Delta X}{A}\right) = 2n_0^2\Delta X \quad (6a)$$

$$\frac{d^2}{dt^2}\Delta Y + 2n_0\frac{d}{dt}\Delta X - n_0^2\Delta Y = \frac{GM}{A^2}\left(-\frac{\Delta Y}{A}\right) = -n_0^2\Delta Y \quad (6b)$$

$$\frac{d^2}{dt^2}\Delta Z = \frac{GM}{A^2}\left(-\frac{\Delta Z}{A}\right) = -n_0^2\Delta Z \quad . \quad (6c)$$

Kepler's third law has been used to replace GM/A^3 by n_0^2.

Equation (6c) is the equation of motion of a harmonic oscillator, with solution

$$\Delta Z = Re(S_{NS}\, e^{jn_0 t}) \quad (7)$$

for some complex S_{NS}.

Equations (6a) and (6b) are coupled and must be solved simultaneously. Substituting

$$\Delta X = \alpha e^{j\omega t}, \Delta Y = \beta e^{j\omega t} \quad (8)$$

into (6a) and (6b) gives

$$-\omega^2\alpha - 2j\omega n_0\beta - 3n_0^2\alpha = 0 \quad (9a)$$

$$-\omega^2\beta + 2j\omega n_0\alpha = 0 \quad . \quad (9b)$$

Solution of equations (9) provides three linearly independent families of complex solutions of equations (6a) and (6b). One family of solutions is

$$\Delta X = 0, \Delta Y = \beta \quad (10)$$

with both α and ω equal to zero.

When ω is nonzero, equation (9b) has the solution

$$\beta = 2j\left(\frac{n_0}{\omega}\right)\alpha \quad . \quad (11)$$

Substituting this β value reduces equation (9a) to the condition that the absolute value of ω is n_0. The corresponding solutions of equations (6a) and (6b) are

$$\Delta X = \alpha e^{-jn_0 t}, \Delta Y = -2j\alpha e^{-jn_0 t} \quad (12a)$$

and

$$\Delta X = \alpha e^{jn_0 t}, \Delta Y = 2j\alpha e^{jn_0 t} \quad . \quad (12b)$$

A final family of solutions of equations (6a) and (6b), not of the form of equation (8), is

$$\Delta X \text{ constant}, \Delta Y = -\tfrac{3}{2}n_0 t\,\Delta X \quad . \quad (13)$$

The actual diurnal ΔX oscillation must be real and of the form

$$\begin{aligned}\Delta X_{osc} &= \tfrac{1}{2} S_{EW}\, e^{jn_0 t} + \tfrac{1}{2}\overline{S}_{EW}\, e^{-jn_0 t} \\ &= Re(S_{EW}\, e^{jn_0 t}) \end{aligned} \tag{14}$$

(where the bar denotes complex conjugate) for some complex S_{EW}. Equations (12) show that the corresponding ΔY oscillation is

$$\begin{aligned}\Delta Y_{osc} &= 2j(\tfrac{1}{2} S_{EW}\, e^{jn_0 t}) - 2j(\tfrac{1}{2}\overline{S}_{EW}\, e^{-jn_0 t}) \\ &= 2[j \cdot \tfrac{1}{2}(S_{EW}\, e^{jn_0 t} - \overline{S}_{EW}\, e^{-jn_0 t})] \\ &= -2Im(S_{EW}\, e^{jn_0 t}) \quad . \end{aligned} \tag{15}$$

Representation of diurnal range errors

Approximating the range error for any ground station by

$$\Delta\rho = (u, v, w) \cdot (X, Y, Z) \quad , \tag{16}$$

the diurnal part of the range error becomes

$$\begin{aligned}\Delta\rho_{osc} &= u\Delta X_{osc} + v\Delta Y_{osc} + w\Delta Z \\ &= Re\left[(u + 2jv)\left(\Delta X_{osc} - \frac{j}{2}\Delta Y_{osc}\right)\right] + w\Delta Z \\ &= Re[((u + 2jv)\, S_{EW} + wS_{NS})\, e^{jn_0 t}] \quad . \end{aligned} \tag{17}$$

It will prove useful to represent the diurnal range error in the form

$$\Delta\rho_{osc} = Re[(u + 2jv)\,(S_{EW} + \zeta S_{NS})\, e^{jn_0 t}] \tag{18}$$

where $\zeta = \dfrac{w}{u + 2jv}$.

The multiplier ζ depends on the position of the ground station. It may be found from Figure 2 by locating the station relative to the vertical contours of constant latitude and the horizontal contours of constant longitude.

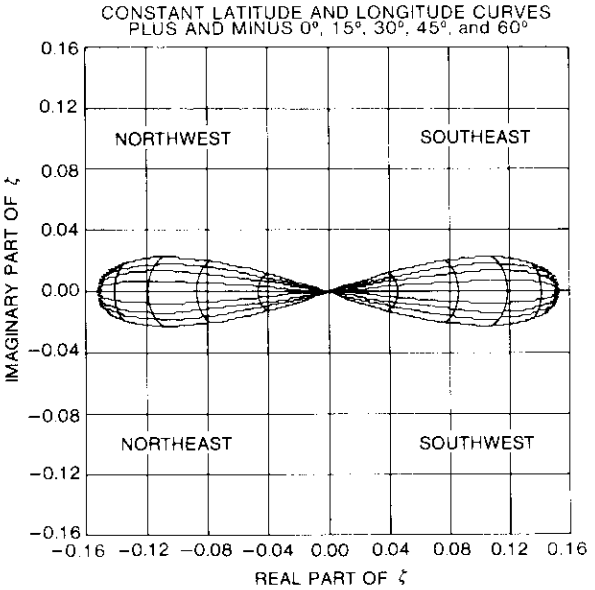

Figure 2. ζ *as a Function of Station Location*

Transformation of diurnal error amplitudes

The values of $S_{EW} + \zeta S_{NS}$ at the two ground stations used to determine the orbit can be employed in solving for S_{EW} and S_{NS}. Let the subscripts 1 and 2 denote values at the first and second ground stations, respectively. Then,

$$S_{EW} = \frac{\zeta_2(S_{EW} + \zeta_1 S_{NS}) - \zeta_1(S_{EW} + \zeta_2 S_{NS})}{\zeta_2 - \zeta_1} \tag{19}$$

and

$$S_{NS} = -\frac{(S_{EW} + \zeta_1 S_{NS}) - (S_{EW} + \zeta_2 S_{NS})}{\zeta_2 - \zeta_1} \quad . \tag{20}$$

For any location,

$$S_{EW} + \zeta S_{NS} = \frac{\zeta_2 - \zeta}{\zeta_2 - \zeta_1}(S_{EW} + \zeta_1 S_{NS}) + \frac{\zeta - \zeta_1}{\zeta_2 - \zeta_1}(S_{EW} + \zeta_2 S_{NS}) \quad . \tag{21}$$

This formula interpolates linearly between the $S_{EW} + \zeta S_{NS}$ values at complex ζ_1 and ζ_2.

Bound on diurnal error in estimated range

Since $v^2 + w^2$ is largest when the satellite is on the station horizon (see Figure 1), and in this case

$$v^2 + w^2 = \left(\frac{R}{A}\right)^2 \quad , \tag{22}$$

$$1.034 = \sqrt{1 + 3\left(\frac{R}{A}\right)^2} \geq \sqrt{(u^2 + v^2) + 3v^2} = |u + 2jv| \tag{23a}$$

and

$$|u + 2jv| \geq \sqrt{1 - w^2} \geq \sqrt{1 - \left(\frac{R}{A}\right)^2} = 0.988 \quad . \tag{23b}$$

Therefore, equation (18) implies that

$$\max |\Delta\rho_{osc}| = |u + 2jv|\,|S_{EQ} + \zeta S_{NS}| \leq 1.034|S_{EQ} + \zeta S_{NS}| \tag{24a}$$

and

$$|S_{EQ} + \zeta S_{NS}| = \frac{1}{|u + 2jv|}\max |\Delta\rho_{osc}| \leq \frac{1}{0.988}\max |\Delta\rho_{osc}| \tag{24b}$$

where the maximum is taken over a period of $\Delta\rho_{osc}$. From equation (21) it now follows that

$$\begin{aligned}\max|\Delta\rho_{osc}| \leq 1.034|S_{EW} + \zeta S_{NS}| &\leq 1.034\left[\frac{|\zeta_2 - \zeta|}{|\zeta_2 - \zeta_1|}|S_{EW} + \zeta_1 S_{NS}|\right. \\ &\quad \left. + \frac{|\zeta - \zeta_1|}{|\zeta_2 - \zeta_1|}|S_{EW} + \zeta_2 S_{NS}|\right] \\ &\leq \frac{1.034}{0.988}\left[\frac{|\zeta_2 - \zeta|}{|\zeta_2 - \zeta_1|}\max|\Delta\rho_{osc,\,1}|\right. \\ &\quad \left. + \frac{|\zeta - \zeta_1|}{|\zeta_2 - \zeta_1|}\max|\Delta\rho_{osc,\,2}|\right] \quad . \end{aligned} \tag{25}$$

Thus,

$$|\Delta\rho_{osc}| \leq 1.05\left[\frac{|\zeta_2 - \zeta|}{|\zeta_2 - \zeta_1|}\max|\Delta\rho_{osc,\,1}| + \frac{|\zeta - \zeta_1|}{|\zeta_2 - \zeta_1|}\max|\Delta\rho_{osc,\,2}|\right] \quad . \tag{26}$$

It can be seen that the denominators in inequality (26) increase more rapidly with increasing latitude separation of the ground stations used to determine the orbit than with increasing longitude separation.

As an example of the use of inequality (26), consider the diurnal error in the estimated range from the INTELSAT Andover ground station (longitude 289.3°E, latitude 44.6°N) to a satellite at 325.5°E. Suppose that the orbit has been determined using range data from the Tangua (317.2°E, −22.7°N) and Pleumeur-Bodou (356.5°E, 48.8°N) ground stations. Noting that Andover is 36.2° west, Tangua 8.3° west, and Pleumeur-Bodou 31.0° east of the satellite, measuring magnitudes of ζ differences on Figure 2 yields

$$\frac{|\zeta_{PB} - \zeta_{AND}|}{|\zeta_{PB} - \zeta_{TNG}|} \simeq 0.16 \quad \text{and} \quad \frac{|\zeta_{AND} - \zeta_{TNG}|}{|\zeta_{PB} - \zeta_{TNG}|} \simeq 1 \quad . \tag{27}$$

Consequently,

$$|\Delta\rho_{osc,\,AND}| \lesssim 0.17\max|\Delta\rho_{osc,\,TNG}| + 1.1\max|\Delta\rho_{osc,\,PB}| \quad . \tag{28}$$

Acknowledgment

The author wishes to thank V. J. Slabinski of INTELSAT for encouragement and for useful technical discussions during the preparation of this paper.

References

[1] V. J. Slabinski, "Variation in Range, Range-Rate, Propagation Time Delay, and Doppler Shift for a Nearly Geostationary Satellite," *Progress in Astronautics and Aeronautics*, Vol. 33, 1974, pp. 3–28.

[2] V. Szebehely, *Theory of Orbits—The Restricted Problem of Three Bodies*, New York: Academic Press, 1967.

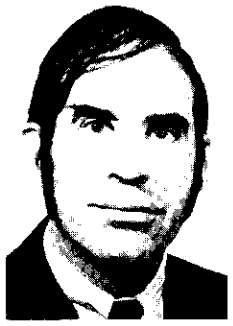

Peter C. Kammeyer received a B.S. in Mathematics, from the University of Washington in 1970, and M.S. and Ph.D. degrees from the Courant Institute of Mathematical Sciences, New York University, in 1972 and 1974, respectively. From 1982 to 1986, he was a Senior Specialist in Astrodynamics at COMSAT. He is presently at the U.S. Naval Observatory pursuing research in the dynamics of planetary orbits.

CTR Notes

New anode catalyst for the negative electrode of the nickel-hydrogen battery

H. VAIDYANATHAN

(Manuscript received November 7, 1985)

Introduction

The nickel-hydrogen (Ni/H_2) battery possesses a unique combination of electrochemical properties which makes it extremely attractive for aerospace applications where long life, high energy density, and reliability are important. The INTELSAT V series, the GSTAR, and the SPACENET communications satellites currently use Ni/H_2 batteries as a power source. Sandia National Laboratories, Albuquerque, New Mexico, sponsored a program to reduce the cost of the Ni/H_2 battery without sacrificing performance. This program resulted in development of the high-capacity, common pressure vessel Ni/H_2 battery for commercial applications.

The greatest contributor to the cost of the aerospace Ni/H_2 battery design is the negative electrode, because platinum black is used as the anode catalyst [1],[2]. Therefore, development of an electrode using an alternate catalyst material became imperative. Among the non-noble metal catalysts, Raney nickel has been referred to as a cost-effective alternative to platinum [3]. Thus, negative electrodes containing Raney nickel fabricated by Varta Batterie, Federal Republic of Germany, were evaluated to determine their applicability to Ni/H_2 cells. The experimental results showed that the Raney nickel electrodes exhibit somewhat higher polarization for the hydrogen oxidation reaction and are four times heavier and thicker than platinum catalyst electrodes. Consequently, attention was directed to other catalyst compositions which contain minute amounts of noble metal.

Carbon-based catalysts containing small amounts of platinum have been used in H_2/O_2 fuel cells for several years, and their catalytic activity has been discussed by Kunz and Gruver [4]. Two variations of catalyst electrodes are derived from carbon-platinum. The fuel cell carbon-platinum electrode consists of a hydrophobic carbon paper to which is applied a mixture of platinum black and Teflon®. Another variation uses supported carbon-platinum catalyst which is prepared by several methods, including the impregnation of carbon with a colloidal dispersion containing chloroplatinic acid and sodium dithionite [5]. In the latter variation, the available platinum area is believed to be maximized.

Hariharan Vaidyanathan is a Senior Member of the Technical Staff in the Energy Conversion and Storage Department of the Applied Technologies Division at COMSAT Laboratories.

This note outlines the development of a hydrogen anode based on supported platinum-carbon catalyst containing 2 to 10 percent platinum. Using a 10-percent platinum-on-carbon supported catalyst results in a tenfold reduction in platinum usage and significant cost savings when compared to the present aerospace electrode which uses 6 to 8 mg/cm^2 of platinum, with negligible loss in performance.

Electrode design, structure, and fabrication

At COMSAT Laboratories, a multilayered, rectangular hydrogen anode has been designed consisting of the catalyst on the front face, a central current-collecting grid, and a microporous, wet-proofing back layer. The chemical composition and wetability of each ply are different. The hydrogen reaction occurs on the front face, which constitutes a three-phase interface of gas, electrolyte, and solid catalyst sites. The back layer wet-proofs the electrode and prevents loss of electrolyte.

A new procedure for fabricating the electrode was developed which roll-compacts a mixture of the supported carbon-platinum catalyst, Teflon powder, and a bulking agent to produce very thin continuous catalyst films [6]. The procedure is amenable to fabricating extremely thin films (<0.02 mm) with a total catalyst (platinum-on-carbon) loading of 1 mg/cm^2. The film is easy to handle and store and can be sized to fabricate electrodes of desired catalyst loading. Properties of the catalyst film such as porosity, pore diameter, wetability, thickness, and platinum distribution and loading can be controlled with great accuracy. The catalyst film is subsequently laminated to one face side of the current-collecting grid, and a film of microporous Teflon is laminated to the opposite face. The structure is hydraulically pressed (0.015 cm) and then sintered at 330°C for 15 minutes.

The design variables in the new catalyst electrode are the type of carbon support, platinum loading, type of current-collecting grid, thickness of the catalyst layer, and the presence or absence of the wet-proofing microporous Teflon membrane. Table 1 presents the design features of a typical electrode. The weight and thickness of the new electrodes are very similar to those of conventional aerospace electrodes.

TABLE 1. DESIGN FEATURES OF THE NEGATIVE ELECTRODE

ITEM	DESCRIPTION
Dimension	14 × 12 × 0.015 cm
Weight	7 gm
Electrocatalyst	10% platinum on carbon
Hydrophobic Layer	Microporous Teflon
Electrode Tab	Integral to the grid
Current Collector	Expanded nickel grid
Platinum Loading	0.45 mg/cm^2

Catalyst Layer

The catalyst side of the electrode is semihydrophobic, with its mercury intrusion porosity and medium-pore diameter a function of catalyst loading. Compared to other cell components, the porosity of the negative electrode, ranging from 78.2 to 91.5 percent, is equal to or less than that of the separator but greater than that of the positive electrode. The median pore diameter is higher than that of the positive plate and the separator (ranging from 10.3 to 17.4 μm), thus minimizing flooding of the electrode by capillary action.

The catalyst layer is dimensionally very stable and structurally sound when the electrode is subjected to vigorous gas evolution. Since the hydrogen reaction is diffusion-controlled, a great deal of attention was directed toward achieving a balance of hydrophylic and hydrophobic properties. The roll compaction procedure produces a fabrillose Teflon matrix through which hydrogen gas diffuses faster than through the electrolyte. The thinner the layer of catalyst, the better the diffusion-limited process [7].

TYPE OF CARBON

The type of carbon used in the support is an important design variable. Candidate carbons differ markedly in their resistance to oxidation, stability in KOH, wetability, conductivity, and surface area. Experimental electrodes, some with the same platinum loading, were fabricated using several types of carbon. A comparison was made between Vulcan XC72, one of the most widely used carbons, and Shawinigan acetylene black. The electrodes were tested for polarization in a half-cell consisting of a platinum/carbon working electrode and platinum black reference electrodes. The polarization cell was activated with 30-percent KOH and 100 psi of hydrogen. The working electrode was polarized galvanostatically in the hydrogen oxidation region and the overvoltage was measured.

The experimental polarization data displayed in Table 2 show that polarization is worse for the electrode based on Shawinigan black. Subsequently, the two supported catalysts were characterized for surface area and microstructure. The surface areas, determined by the nitrogen adsorption method of Brunauer, Emmet, and Teller (the BET procedure), were 200 m^2/gm for the catalyst powders based on Vulcan XC72

TABLE 2. DEPENDENCE OF ELECTROCHEMICAL POLARIZATION ON THE NATURE OF THE CARBON SUPPORT

CARBON SUPPORT	PLATINUM CONTENT (%)	BET SURFACE AREA OF THE CATALYST POWDER (m^2/gm)	BET SURFACE AREA OF THE CATALYST LAYER (m^2/gm)	CARBON STRUCTURE FROM SAD PATTERN	PLATINUM DISTRIBUTION FROM TEM	OVERVOLTAGE AT 15 mA/cm^2 (mV)
Vulcan XC72	10	199.85	57.45	Amorphous	Well dispersed	25.9
Shawinigan Black	10	58.46	22.71	Amorphous	Large platinum particles	50.2

and 59 m^2/gm for Shawinigan black. There was a corresponding variation in the surface area of the catalyst layer, with 57.45 m^2/gm for the Vulcan material and 22.71 m^2/gm for the Shawinigan-based material.

Scanning electron microscopy (SEM) was used to obtain light-field electron micrographs of both catalysts. The crystalinity of the carbon support was determined by a selected area diffraction (SAD) technique. Figures 1 and 2 present the SEM micrographs and SAD patterns for both the catalysts. The SAD patterns reveal similarities in the amorphous nature of the carbon support. The spacing of the sharp diffraction rings in the SAD pattern is consistent with face-centered cubic platinum. The Vulcan XC72-based catalyst exhibits uniform dispersion of platinum with no large agglomerates, while the Shawinigan black catalyst contains larger diameter platinum particles. Table 2 illustrates the dependence of electrochemical polarization on the physical properties of the catalyst powder. Thus, the better catalytic activity of Vulcan XC72 (as indicated by low polarization) can be correlated to more uniform dispersion of platinum particles having a large surface area. Hence, Vulcan XC72 is preferred to Shawinigan black for the new anode catalyst.

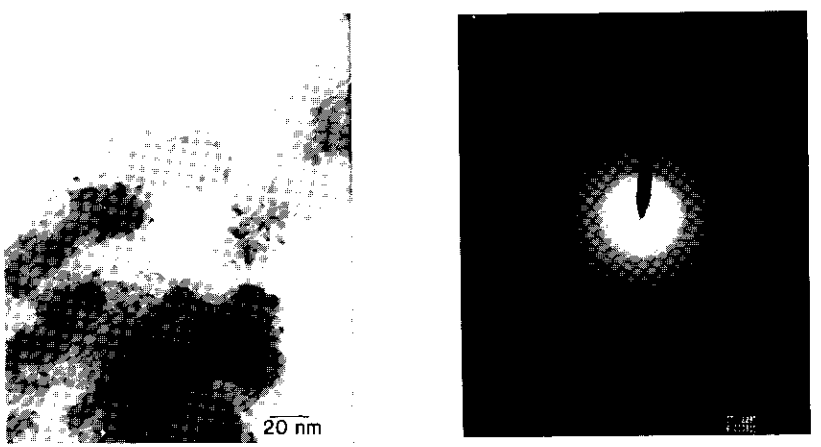

(a) Bright-Field Electron Micrograph (b) Corresponding SAD Pattern

Figure 1. *10% Platinum on Vulcan XC72 Catalyst Displays a Typical Distribution of Platinum (dark spots) on Carbon*

PLATINUM LOADING

The platinum loading in the electrode can be varied either by using different types of platinum/carbon-supported catalysts containing different amounts of platinum or by reducing the thickness of the catalyst layer, thereby reducing the loading of both carbon and platinum. Both methods were used to test electrodes with platinum loading from 0.16 to 0.45 mg/cm^2 to determine the overvoltage for hydrogen oxidation.

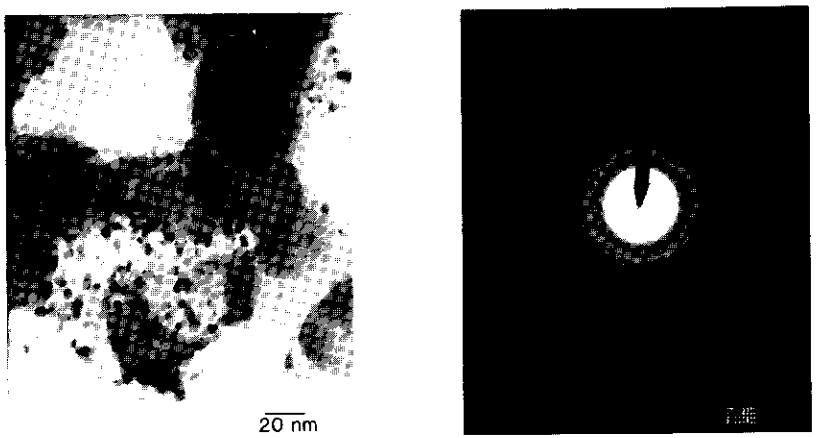

(a) Bright-Field Electron Micrograph (b) Corresponding SAD Pattern

Figure 2. *Platinum on Shawinigan Black Catalyst Displays a Typical Distribution of Platinum Particles (dark spots) Which are Slightly Larger*

Table 3 summarizes the test results, showing that polarization increases as platinum loading decreases. The polarization, using a very thin layer (<0.01 mm) at a platinum loading of 0.183 mg/cm^2, was lower than at a platinum loading of 0.24 mg/cm^2 achieved with a 5-percent platinum-on-carbon catalyst. Possible reasons for this anomaly could be the type of carbon (peat) in the 5-percent catalyst or the ease of hydrogen diffusion in a very thin catalyst layer.

TABLE 3. VARIATION OF ELECTROCHEMICAL ACTIVITY WITH PLATINUM LOADING

CATALYST TYPE (% Pt ON C)	MEANS OF ACHIEVING LOWER Pt LOADING	CATALYST LOADING (Pt + C) (mg/cm^2)	Pt LOADING (mg/cm^2)	POLARIZATION AT 15 mA/cm^2 (mV)
10	Lower platinum percentage in carbon	4.5	0.45	19
10	Thin catalyst layer	3.763	0.37	25.9
10	Thin catalyst layer	1.836	0.183	53.8
5	Lower platinum percentage in carbon	4.82	0.24	65
2	Lower platinum percentage in carbon	8.10	0.16	126

In the negative electrode, the wet-proofing Teflon (Gore-Tex(TM)) layer contributes approximately one-fourth of the cost of materials and is therefore another important variable. Electrodes fabricated with and without Gore-Tex backing were tested directly in 100-Ah prismatic Ni/H_2 cells. Figure 3 shows discharge curves for two cells, one with negative electrodes fabricated with Gore-Tex backing and the other without Gore-Tex. The voltage profiles are almost identical. In addition, both cells exhibited similar end-of-charge voltage and pressure. The cell without Gore-Tex on the negative electrodes has already completed 248 charge/discharge cycles, and cycle testing is being continued to determine its endurance limits. Preliminary results show that the Gore-Tex layer is superfluous for the commercial battery in a gravitational field, although it is important in an aerospace cell to prevent loss of electrolyte by entrainment.

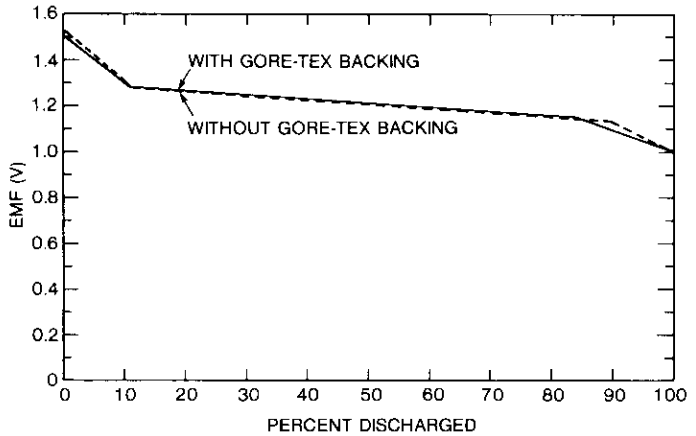

Figure 3. *Variation of Cell Electromotive Force During Discharge at C/5*

GRID DESIGN

Three types of grid designs (expanded nickel, electroformed perforated nickel, and 40 × 40 nickel wire mesh) were evaluated as the current collector by determining the potential drop at various locations at a polarizing current of 10 A. Figure 4 shows the electrode measurement locations. The potential drops at the bottom of the rectangular electrodes are 83, 58, and 52 mV for the three structures, respectively, whereas the potential drops at the center of the electrode are 38 mV for both the expanded nickel and electroformed perforated grids and 44 mV for the mesh. The potential drops at the top right corner are 32, 47, and 40 mV, respectively. Thus, with regard to potential distribution, all three grid designs are acceptable. The nickel content in the designs is 0.039 g/cm^2, 0.037 g/cm^2, and 0.0345 g/cm^2, respectively. While the 40 × 40 mesh and electroformed designs are currently less expensive, still further cost reduction is expected for the 40 × 40 mesh.

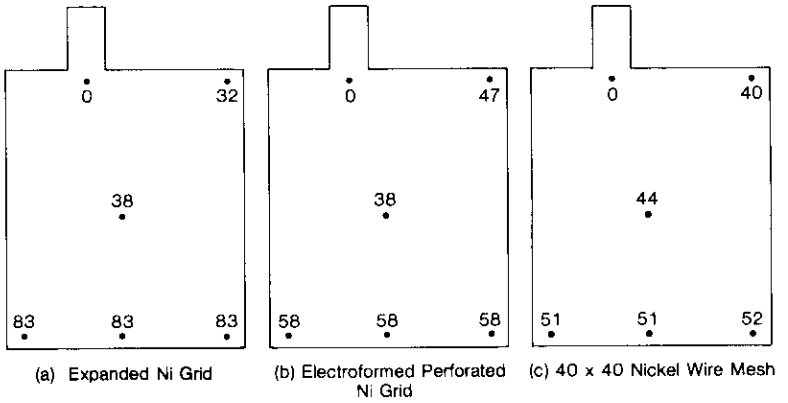

Figure 4. *Potential Mapping During a 10-A Charge (in mV)*

Life-cycle performance in cells

The new anode catalyst electrodes were tested in several 100-Ah prismatic cells and in two 7.5-V, 100-Ah common pressure vessel batteries. The cell design consisted of a rectangular electrode stack suspended in a polypropylene cell case of 19.2 × 14 × 4.7 cm. The battery contained six prismatic cells connected in series. The cells and battery are tested inside a stainless steel pressure vessel which holds the hydrogen gas. The cycling regime consisted of charging at the 10-hour rate and discharging at the 5-hour rate at 80-percent depth of discharge. One of the batteries has completed 531 cycles and another 127 cycles without any noticeable degradation in capacity. The batteries continue to be cycle-tested at Sandia National Laboratories. One of the 100-Ah cells was tested for 1,064 cycles and thereafter disassembled to examine the components. The negative electrodes from the cycled cell exhibited neither mechanical damage nor an increase in polarization.

Conclusions

Hydrogen electrodes fabricated using a new anode catalyst of 10-percent platinum and utilizing Vulcan XC72 carbon as support exhibit low polarization and charge/discharge characteristics similar to platinum-black-based electrodes. In the prismatic design with rectangular electrodes, the wet-proofing Gore-Tex layer can be eliminated without any adverse effect on performance. Life cycle characteristics of electrodes without Gore-Tex backing are being investigated. A less expensive grid design consisting of 40 × 40 nickel mesh has been substituted for expanded nickel. A rolling and compacting procedure developed to fabricate continuous films of very thin catalyst layer not only reduces the number of steps in the fabrication of the electrodes but also enhances uniformity, with greater control on loading level, thickness, absorbency, and wetability.

The foremost advantage of the new catalyst electrode is its lower cost. The negative electrode is the single most expensive component in the aerospace Ni/H_2 cell. Calculations show that the material cost of the aerospace negative electrode containing 8 mg/cm^2 of platinum black catalyst, expanded nickel grid design, and Gore-Tex backing can be reduced by 77.6 percent with supported platinum/carbon catalyst. Use of 40 × 40 mesh as the grid design would reduce the grid cost by about 88 percent. By eliminating Gore-Tex and using very thin catalyst layers, a reduction of about 92 percent in material costs can be realistically achieved. Experimental cells containing such low-cost negative electrodes are under test and their performance is excellent. Many of the cost reductions can be carried over to aerospace applications without loss of reliability or performance.

Acknowledgments

The author is grateful to M. J. Kaufman of the National Bureau of Standards for performing transmission electron microscopy, J. Symanski of Johnson Controls, Inc., for the potential drop measurements, P. Troup for sample preparation, and J. D. Dunlop and M. W. Earl for many helpful discussions.

References

[1] J. D. Dunlop *et al.*, "Design and Development of a Sealed 100-Ah Nickel-Hydrogen Battery," NTIS, Contract Report No. SAND 84-7155, Springfield, Virginia, August 1984.

[2] H. Vaidyanathan and J. D. Dunlop, "Performance of Carbon-Based Negative Electrodes for Ni/H_2 Batteries Based Upon Stable Hydrogen-Storing Materials," 14th International Power Sources Symposium, Brighton, England, September 17–20, 1984, *Proc.*, pp. 305–315.

[3] A. Winsel, "Raney-Nickel Based Hydrogen Electrode for Electrochemical Processes," 14th International Power Sources Symposium, Brighton, England, September 17–20, 1984, *Proc.*, pp. 437–445.

[4] H. R. Kunz and G. A. Gruver, "The Catalytic Activity of Platinum Supported on Carbon for Electrochemical Oxygen Reduction in Phosphoric Acid," *Journal of the Electrochemical Society*, Vol. 122, No. 10, 1975, pp. 1279–1287.

[5] V. M. Jalan and C. L. Bushnell, "Method for Producing Highly Dispersed Catalytic Platinum," U.S. Patent No. 4,136,059, and "Catalyst and Method for Making," U.S. Patent No. 4,137,372, 1979.

[6] H. Vaidyanathan, "Hydrogen Electrode for a Fuel Call," U.S. Patent No. 4,585,711, 1986.

[7] R. Holze and W. Vielstich, "The Kinetics of Oxygen Reduction at Porous Teflon-Bonded Fuel Cell Electrodes," *Journal of the Electrochemical Society*, Vol. 131, No. 10, 1984, pp. 2298–2303.

Synthesized C-band down-converter

E. W. ROTHERMICH AND S. T. WILLIAMS

(Manuscript received December 2, 1985)

Introduction

The advent of noncommercial television receive-only (TVRO) earth stations in the mid-1970s represents the first high-volume application of microwave communications technology in the consumer market. Previous microwave products intended for use by the general public, such as automotive radar detectors and microwave ovens, were not intended for communications and do not disseminate intelligence. With most new applications of technology, significant obstacles must be overcome before the resulting hardware can make the transition from a laboratory demonstration to a production item, and the microwave portion of Amplica's TVRO systems was no exception.

This paper examines several of the technical challenges encountered in the design of a consumer-oriented C-band to 70-MHz single-conversion down-converter. The problem of local oscillator (LO) frequency drift caused by exposure of the LO to a wide range of temperatures, and its solution via frequency synthesis, are given particular consideration. The economics of the consumer market have forced the evolution of a 2-GHz push-push oscillator in conjunction with subharmonically pumped mixers, resulting in direct conversion from C-band. Since an image reject mixer is required in order to suppress undesired in-band responses, amplitude and phase requirements for image rejection are presented. A prescaler originally intended for use in UHF television receivers is employed to divide the oscillator's 1-GHz fundamental down to a frequency at which phase locking can be performed. In addition, the requirement that this down-converter be compatible with all of Amplica's previous home TVRO systems has caused the inclusion of a precision analog voltage tuning system, which is explained in detail. Finally, the down-conversion performance of a typical production unit is documented.

Background

Early TVRO systems were relatively simple, typically using a frequency tuning knob for transponder selection, some means of selecting among various audio subcarriers, and a polarization control. Users included those living in areas with little or no

E. Wayne Rothermich is a Project Manager in the Microwave Technology Development Department of the Advanced Engineering Group at Amplica, Inc.

Scott T. Williams is a Microwave Engineer in the Microwave Products Development Department of the Advanced Engineering Group at Amplica, Inc.

VHF/UHF television available, hobbyists, and novelty seekers. The microwave LO, which selected the transponder frequency, was tuned using a control with continuous rotation so that fine tuning and transponder selection were both accomplished with one adjustment. Any LO drift with time or temperature was compensated for by periodically readjusting the tuning control. (This was perceived by most early users as a minor inconvenience relative to the benefits of owning a TVRO system.)

As TVRO became more commonplace, the predominant users wanted a TVRO system as an adjunct to pre-existing VHF/UHF television and demanded operational simplicity and convenience, including detent tuning which permits unambiguous selection of a desired transponder. The second generation of TVRO receivers attempted to fill this need, but with widely varying degrees of success.

Because of the required frequency precision, incorporation of detent in a consumer product involves more than just placing mechanical stops on the tuning control. When users select a particular transponder, they expect that their receiver will be precisely adjusted to the proper frequency and will not require fine tuning. This places stringent requirements on the LO frequency stability *vs* time and temperature. Of the two, temperature drift is by far the more difficult problem.

The frequency band used for TVRO down-links extends from 3.7 to 4.2 GHz. To avoid the severe loss encountered in small coaxial cable at these frequencies, most consumer systems place the first down-conversion stage (including the first LO) on the antenna structure. Thus the first LO, nominally operating from 3.77 to 4.27 GHz, is subjected to the full outdoor temperature range, typically from $-40°$ to $+65°C$ within the more populous areas of North America. This temperature range is only slightly less than that specified for military applications and represents a significant design challenge.

Due to size and cost constraints, consumer TVRO systems usually operate at carrier-to-noise ratios (*C/N*s) only slightly above the FM threshold. To achieve the best video signal-to-noise ratio (*S/N*), the IF filters are often significantly narrower than the nominal 36-MHz bandwidth of the transmitted signal. The bandwidth limit is reached when truncation noise becomes visible in demodulated video. For typical signals, a bandwidth of approximately 25 MHz has been found to be optimal.

Errors in centering the IF signal in the passband also result in truncation noise when a narrow IF passband is used. This establishes an absolute frequency accuracy requirement for the LO. Empirical data indicate that centering errors of 1 MHz or less produce only very small increases in truncation noise when a narrow filter is used.

A frequency shift relative to room temperature of 1 MHz out of 4 GHz at $-40°C$ represents a linear temperature coefficient of 3.8 ppm/°. This stability can be achieved in a voltage-controlled oscillator (VCO) by meticulous adjustment of the temperature compensation network; however, the economics of high-volume production preclude this approach. An alternate approach is fixed compensation, which produces zero drift for VCOs at the center of the statistical distribution. Production variations typically yield overall temperature-induced frequency drifts of 10 MHz. A few units will drift 100 MHz or more. These drifts are well beyond the required 1-MHz accuracy and demonstrate the need for a significantly different approach.

A quartz crystal oscillator can achieve the required stability at a level of economy compatible with consumer applications. The difficulty here is the requirement that the oscillator be tunable, which can be resolved by using the crystal oscillator as the frequency reference for a phase-locked synthesizer. This is the approach that was adopted for the Amplica model D-200 down-converter.

System considerations and design

In addition to the requirement for frequency stability, the specifications for the D-200 down-converter were directed toward the following goals:

- no significant contribution to the overall system noise figure,
- no limitation on overall system dynamic range,
- compatibility with all previous Amplica TVRO products,
- proper down-converter operation with any commonly available low-noise amplifier (LNA) intended for home use, and
- ease of installation and protection against improper installation.

Analysis of system noise figure requirements established that a down-converter maximum noise figure of 17 dB would be sufficient. The down-converter contribution to the system noise temperature varies depending on the gain of the preceding LNA. Assuming the following system configuration:

- Amplica 3.05-m (10-ft) fiberglass dish (temperature = 40 K),
- 0.1-dB loss feed horn,
- 3-dB loss interconnect cable [3.05 m (10 ft) of RG-213], and
- D-200 down-converter with worst-case noise figure (17 dB),

the noise figure contributions for LNAs would be

LNA Description	D-200 System Noise Temperature Contribution
35 dB, 80 K	8.7 K (0.128 dB)
50 dB, 80 K	0.96 K (0.01 dB)

The use of a higher-loss feed horn or higher noise figure LNA would lessen down-converter contribution to the overall system noise figure.

The second goal listed above dictates that a dynamic range and third-order intercept analysis be performed [1]. Table 1 presents the link budget, which provides the minimum signal power levels at the down-converter output, assuming the minimum signal level and a single transponder. Thus, the spurious noise output power in a 22-MHz bandwidth (worst-case minimum) at the IF output should be

$$-44.9 \text{ dBm} - 20 \text{ dB (noise suppression allowance)}$$

$$= -64.9 \text{ dBm (maximum)}$$

TABLE 1. LINK BUDGET FOR THE DOWN-CONVERTER

Noise Temperature*	98 K	
Antenna Noise Temperature	40 K	(estimated)
Total Noise Temperature	138 K	
System Noise Temperature (dB above 1 K)	21.4 dB	(138 K)
Boltzmann's Constant	−228.6 dBW	
Bandwidth (dB above 1 Hz)	73.4 dB	(22 MHz)
Total Incident Receiver Noise Power	−133.8 dBW	(−103.8 dBm)
Required *C/N*	7.0 dB	(minimum threshold)
Minimum Usable Power at Feed	−126.8 dBW	(−96.8 dBm)
Power at Feed Input	−96.8 dBm	
Feed Horn Loss	−0.1 dB	
Power at LNA Input	−96.9 dBm	
LNA Gain	35.0 dB	(minimum)
LNA Power Out	−61.9 dBm	
Cable Loss	−3.0 dB	
D-200 Conversion Gain	20.0 dB	(minimum)
Minimum D-200 Output	−44.9 dBm	(input to IF cable)

* System configured of a −0.1 dB feed loss; a 35-dB, 80-K LNA; a −3 dB cable; and a 20-dB conversion gain D-200 (noise figure = 17 dB).

Since the IF bandpass filter used in the receiver is non-ideal, this specification is applied to all spurious outputs other than the LO, associated harmonics and subharmonics, and spurious passbands.

The maximum required output power level is determined by performing a third-order intermodulation analysis, as presented in Table 2. Table 3 gives the required third-order intercept and 1-dB compression levels. Assuming that this total power forms two equal amplitude tones of −25.6 dBm each (for the purposes of worst-case design), the desired signal must be 42 dB above intermodulations, as presented in Table 4. For 25-dB maximum D-200 conversion gain, the two-tone level is

$$-25.6 \text{ dBm} + 25 \text{ dB conversion gain} = -0.6 \text{ dBm}$$

and the required third-order intermodulation product is

$$-0.6 \text{ dBm} + (42/2) = 20.4 \text{ dBm} \quad .$$

Since the 1-dB compression point is approximately 10 dB below the third-order intercept,

$$20.4 \text{ dBm} - 10 \text{ dB} = 10.4 \text{ dBm (minimum 1-dB compression level)} \quad .$$

TABLE 2. THIRD-ORDER INTERMODULATION REQUIREMENTS: D-200

ITEM	LEVEL	
Satellite Power	67.0 dBm	(1 dB stronger than Hughes Galaxy 1)
Path Loss	−195.0 dB	
Power at Dish	−128.0 dBm	
Dish Gain	43.5 dB	[4.57-m (15-ft) diameter, 60% efficient dish]
Power at Feed	−84.5 dBm	
Feed Horn Loss	−0.1 dB	(minimum)
At LNA Input	−84.6 dBm	
LNA Gain	55.0 dB	(maximum)
Miniamplivider*	3.0 dB	(maximum gain)
Cable Loss	0 dB	(no cable)
Input Level to D-200	−26.6 dBm	

* A C-band active splitter for use in multiple-receiver installations.

TABLE 3. REQUIRED THIRD-ORDER INTERCEPT AND 1-dB COMPRESSION LEVELS

ITEM	LEVEL
Input to D-200 (single transponder)	−26.6 dBm
Full 12 Transponders (one polarity)	10.0 dB
Limit D-200 IF Bandwidth to 130 MHz	−6.0 dB
Total Power: D-200 Input	−22.6 dBm

TABLE 4. SIGNAL MARGIN BUDGET

IMPAIRMENT SOURCE	CONTRIBUTION
Level of Single Transponder Below Full-Band Power	10 dB
Noise Suppression Allowance	20 dB
D-200 Gain Flatness Specification	4 dB
LNA Gain Flatness Specification	6 dB
Transponder-to-Transponder Variation	2 dB
Desired Level Above Intermodulations	42 dB

The third goal dictates that the D-200 be tuned by using a precision analog tuning voltage which requires a precision analog-to-digital (A/D) converter whose design is detailed later. Additionally, this third criterion is satisfied by conversion gain specifications of 20 dB minimum and 25 dB maximum.

The fourth consideration, that of maintaining compatibility with most consumer-available LNAs, limits the down-converter spurious passband response. Although the feed horn and CPR-229 input flange on the LNA limit the passband of the front end of the system, many LNAs produce considerably greater out-of-band noise than in-band noise. This apparent anomaly is caused by the front-end stage(s) of the LNA being tuned for minimum noise figure over the normal band of operation, while the out-of-band noise is not controlled. Further, the gain of the subsequent amplifying stages increases at roughly 6 dB per octave, resulting in significantly higher noise levels below the desired band.

A survey of several LNAs produced for the home TVRO market gave rise to the composite worst-case expected noise output levels shown in Figure 1. As a result of these findings, the D-200 spurious bandpass response level is specified at a minimum of 10 dB below the desired passband level.

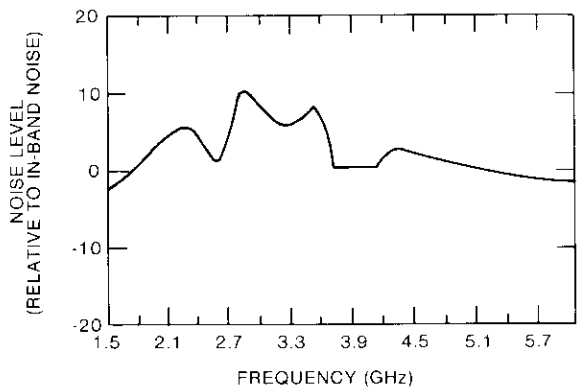

Figure 1. *LNA Noise Output Relative to In-Band Noise*

The final goal calls for the unit to be easy to install and relatively immune to improper installation. Easy installation has been achieved by replacing a power connector (uncommon in the consumer environment but used on previous Amplica down-converters) with a four-position terminal strip. RFI filters are used to reduce undesired LO leakage, to provide noise filtering on all inputs, and to maintain water seal. The type-*N* connector used on previous products for the 70-MHz IF output has been replaced with a waterproof, widely available type-*F* connector. To prevent damage to the unit in the event of improper connection of the power/tune control lines, four reverse voltage protection diodes have been incorporated. One of these diodes, which protects the main power input line, is actually a transient suppressor diode and thus also provides picosecond response for protection against voltage transients.

D-200 block diagram

Figure 2 is an overall block diagram of the D200 down-converter. The down-link signal from the TVRO system LNA is applied to the RF port of an image rejection harmonic mixer. The mixer is subharmonically pumped with a 2-GHz LO, and the 70-MHz difference frequency, after passing through an IF amplifier, is sent to the TVRO receiver.

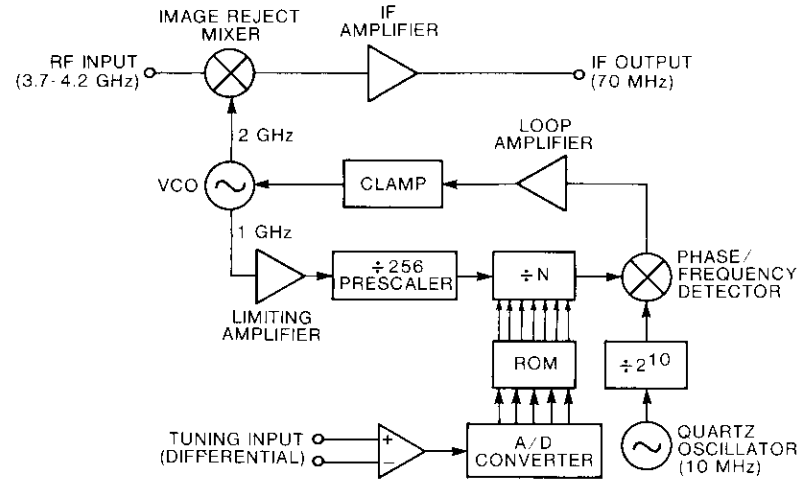

Figure 2. *Block Diagram of the D-200 Down-Converter*

Analog tuning voltages are produced within the TVRO receiver and sent differentially to the down-converter. Inside the down-converter, this signal is applied to a differential amplifier which removes the common-mode signals that can occur over a long run of control cable. The differential amplifier also normalizes the signal level and applies it to an 8-bit A/D converter with locally generated timing and reference voltage signals. The five most significant digits from the A/D converter are then applied to the address inputs of a 256-bit read-only memory (ROM). This ROM serves as a look-up table and translates the binary word from the A/D converter into a 7-bit word which controls the division ratio in a phase-locked loop.

The VCO is a push-push type [2] which supplies both 1- and 2-GHz outputs. The 2-GHz output is applied to the harmonic mixer, while the 1-GHz output goes through a limiting amplifier and on to a digital prescaler which divides the frequency by 256. The resulting 4-MHz signal passes through three stages of divide-by-*N* counters and enters one input port of a digital phase-frequency detector at a frequency of approximately 10 kHz. The other input of this detector is a reference signal of about the same frequency, derived from a quartz crystal oscillator by binary division. The output of the phase-frequency detector is an error signal which, after processing by the loop amplifier and clamp circuits, is used to control the VCO frequency. The result is a VCO locked to a quartz crystal oscillator operating at a much lower frequency.

The frequencies of these oscillators are related by the ratios of their respective digital divisions. Since the divisor for the VCO can be changed under external control, the VCO frequency can be tuned in fixed steps. In the case of the D200 down-converter, these steps correspond to the standard 20-MHz down-link channel spacings.

Local oscillator and mixer

As shown in Figure 2, the down-converter employs a push-push VCO structure and subharmonically pumped mixers. It is the use of these two sections in tandem which allows the economical production of a consumer-oriented down-converter.

The main advantage of the push-push VCO for this application is that it is rich in harmonic energy. This type of oscillator is often used to produce an output frequency of twice that achieved with a single transistor in a more conventional configuration. In the case of the D-200, this characteristic allows two very inexpensive transistors to produce the 2-GHz drive for the subharmonically pumped mixers. Since each transistor is actually oscillating at 1 GHz, an inexpensive prescaler can be used as part of the phase-locking system.

Each subharmonically pumped mixer consists simply of an antiparallel diode pair connected as shown in Figure 3. With the proper choice of diodes, less than 9 dB of conversion loss has been achieved [3].

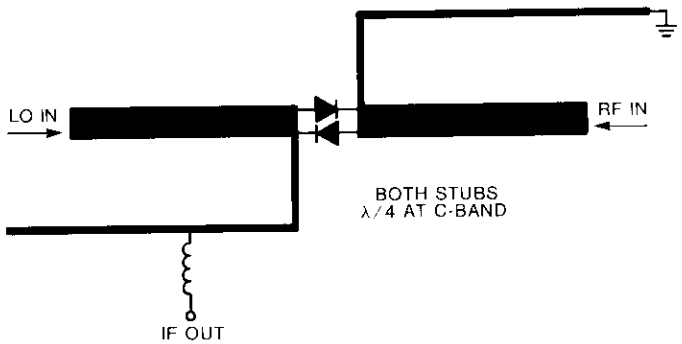

Figure 3. *Subharmonically Pumped Mixer*

This push-push VCO, subharmonically pumped mixer combination is not without drawbacks. Since the VCO produces considerable harmonic energy (at both even and odd harmonics), spurious passbands could occur unless care is taken to prevent them. A bandpass filter of sufficient selectivity proved to be larger than the available circuit board space. Therefore, suppression of some undesired harmonics had to occur within the VCO.

The push-push oscillator achieves frequency doubling through proper phasing of current waveforms rich in harmonic energy. The oscillator can be used as a VCO with the addition of a varactor diode within the resonating networks of each transistor. A more economical approach for frequency tunability is to use the oscillator transistors' collector-base junction as a voltage-variable capacitor by controlling the base bias. This latter approach was used in the D-200.

The output of the VCO is taken at the approximate center of two air core inductors (each attached to the collector of one oscillator transistor). When the output tap occurs at the exact impedance center of this structure, all odd harmonics are suppressed by over 23 dB. In production, the air core inductors are tuned to suppress the 3-GHz spurious passband by a minimum of 20 dB. Spurious passbands caused by higher-order harmonics present less of a problem since the branch line splitter at the down-converter input suppresses any inputs occurring at these frequencies.

Image rejection

To maintain compatibility with previous Amplica TVRO products while allowing the use of standard available accessories (*i.e.*, terrestrial interference filters and descramblers), the D-200 must have an IF output frequency of 70 MHz. Due to the additional cost of a second LO and the required control circuitry to maintain frequency stability, the unit must then employ single conversion.

An image rejection mixer structure is therefore incorporated to suppress the undesired image response shown in Figure 4. This mixer, illustrated in Figure 5, consists of a 90° branch line power splitter, two subharmonically pumped mixers, and a 90° lumped-element recombining hybrid at 70 MHz. Each of the hybrids is tuned in production to ultimately achieve 18 dB of minimum image rejection. The rejection achieved for a given phase imbalance, θ, and amplitude imbalance, A, is given by

$$\text{Rejection (dB)} = 10 \log \left[\left(\tan \frac{\theta}{2} \right)^2 + \left(\frac{10^{A/20} - 1}{10^{A/20} + 1} \right)^2 \right]$$

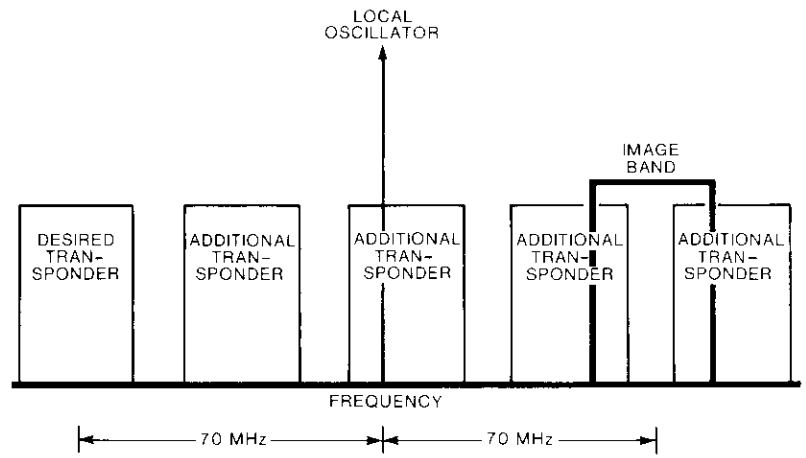

Figure 4. *Image Response Mixer*

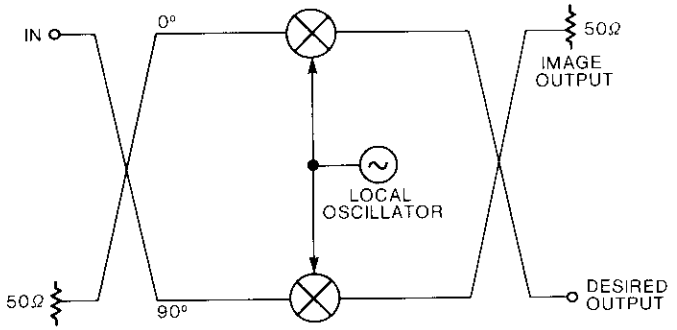

Figure 5. *Image Reject Mixer*

For example, for a phase imbalance of 5° and an amplitude imbalance of 0.5 dB, the image rejection is

$$\text{Rejection (dB)} = 10 \log \left[\left(\tan \frac{5^\circ}{2} \right)^2 + \left(\frac{10^{0.5/20} - 1}{10^{0.5/20} + 1} \right)^2 \right]$$
$$= 25.6 \text{ dB}$$

Additional work is underway to eliminate the necessity of tuning the input branch line hybrid in production, thus eliminating approximately 3 minutes from the tuning time presently required for a single unit (yielding a net savings of nearly $16,000 for every 10,000 units built).

Precision A/D conversion

In order for the D-200 to achieve compatibility with existing Amplica satellite receivers, the tuning voltage must lie in the range of 5 to 9 V. Dividing this span into 24 segments, 1 for each transponder frequency, results in a tuning voltage increment of 167 mV per tuning step. To ensure that the synthesizer always produces the correct LO frequency for the user-selected transponder, the tuning voltage produced by the receiver must fall within the corresponding A/D converter voltage window at the down-converter. This match contains three potential sources of error: resistive drops in the long ground return which can effectively offset all tuning voltages, the voltage drift produced by the receiver, and drift of the A/D converter windows.

The ground return offset voltages are eliminated by sending the tuning voltage differentially. The current on the control lines is small (~1 mA), which produces a drop of only a few millivolts in the longest cables used for TVRO systems. (The maximum length is limited to a few hundred feet by the resistance in the antenna aiming motor cables).

Voltage mismatch between the receiver and the down-converter is handled in the following way. If the receiver voltage is centered in the 167-mV A/D converter

window, the distance to the window edge (and to the next transponder frequency) is 83 mV. If 3 mV is budgeted for cable drops, the total allowable error is 80 mV. Equal division of this error between the receiver and the down-converter allows a worst-case error of +40 mV in each unit.

A total error budget of 40 mV for a signal covering 5 to 9 V represents a total tolerance of about 0.5 percent. To avoid the expense of using instrument-grade components, a method of trimming the circuitry to the required tolerances is needed. The popular method of using variable resistors to adjust the circuitry was rejected due to reliability problems encountered with consumer-grade potentiometers, especially under the conditions of extreme thermal cycling found in the outdoor environment. Additionally, the presence of variable components within consumer electronics often results in malfunctions due to adjustments attempted by persons lacking the equipment and procedural knowledge required to correctly set up the unit. These problems were overcome by using parallel combinations of fixed resistors in the critical areas of the circuit, with one resistor of a much higher value being chosen at the time of adjustment.

Resistor selection is performed at a semiautomatic test station equipped with a bed-of-nails fixture to permit quick simultaneous connections to several points on the circuit board. Careful choice of the resistors to be adjusted minimizes interaction and results in an overall accuracy of a few millivolts. The greater test time required for selection and installation of the fixed resistors is balanced by the reduction in component cost achieved by substituting fixed resistors for the more expensive adjustable resistors.

Figure 6 gives a simplified schematic of the precision analog circuitry. The differential tuning input is applied to an operational amplifier connected as a differential-to-single-ended converter. The adjustment of one resistor value at the inverting

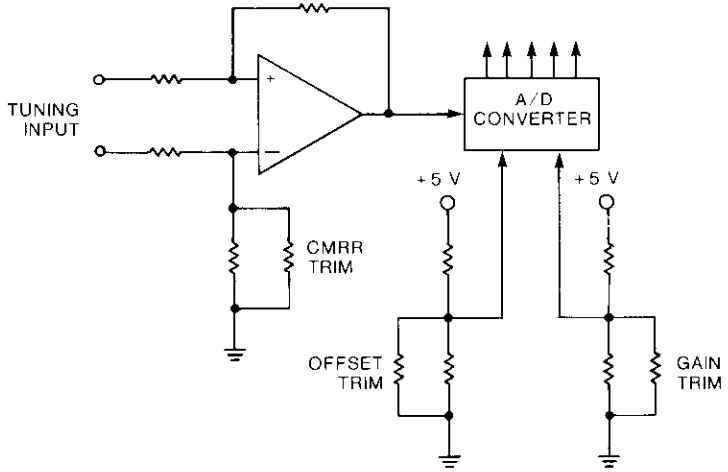

Figure 6. *Precision Analog Circuitry*

(minus) input is used to null the common-mode response of the circuit. The output of this circuit is applied to the input of a successive-approximation type of A/D converter. Other inputs to the A/D converter are voltages which determine the scale factor (gain) and offset voltage of the unit. These voltages are derived by resistive division from a precision 5-V regulator. By using metal film resistors (which have a specified maximum temperature drift of ± 50 ppm/°) throughout the circuit, the overall drift of the tuning voltage window edges is calculated to be within the 40-mV error budget over time, environment, specified tolerances of all components, and expected values of input common-mode voltage and power supply voltage.

Production monitoring

Currently, all D-200 down-converter units are tested for proper operation at 70°C (1-hr soak) prior to shipment. Additionally, a periodic sampling plan is being implemented to monitor randomly sampled units for proper operation, as well as to provide design engineers with the trend indication data needed to prevent device variations or manufacturing process variations from hindering the rapid production of quality units.

Figures 7, 8, and 9 depict the performance of a typical production unit. Spurious passbands, conversion gain, and image rejection are all within the prescribed specifications. The higher amplitude output apparent in the spurious output plot is the LO 1-GHz leakage.

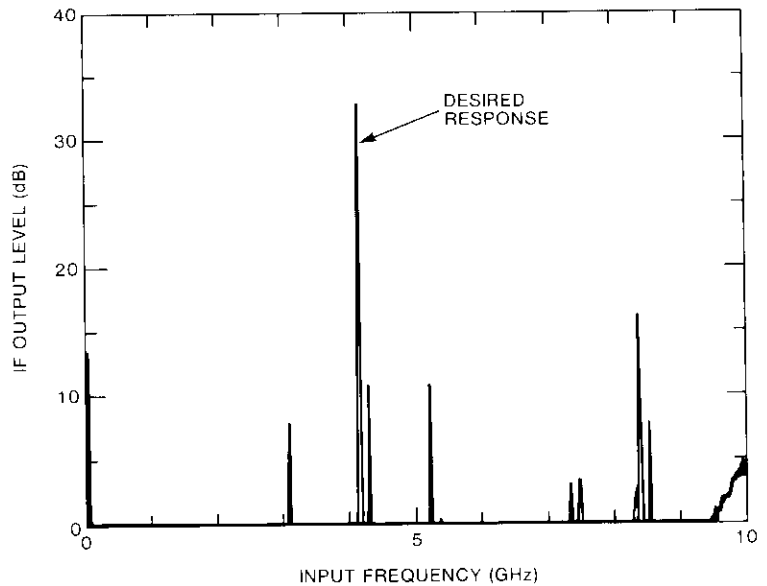

Figure 7. *Spurious Passbands*

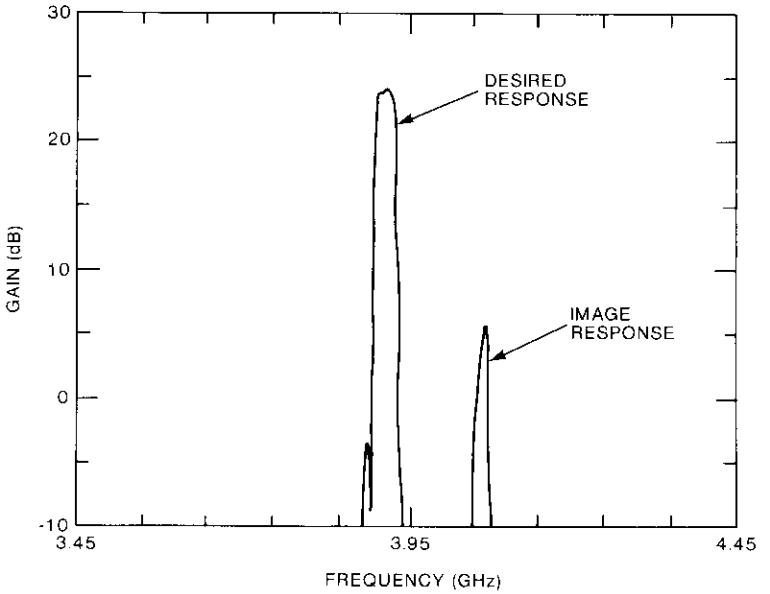

Figure 8. *Image Suppression*

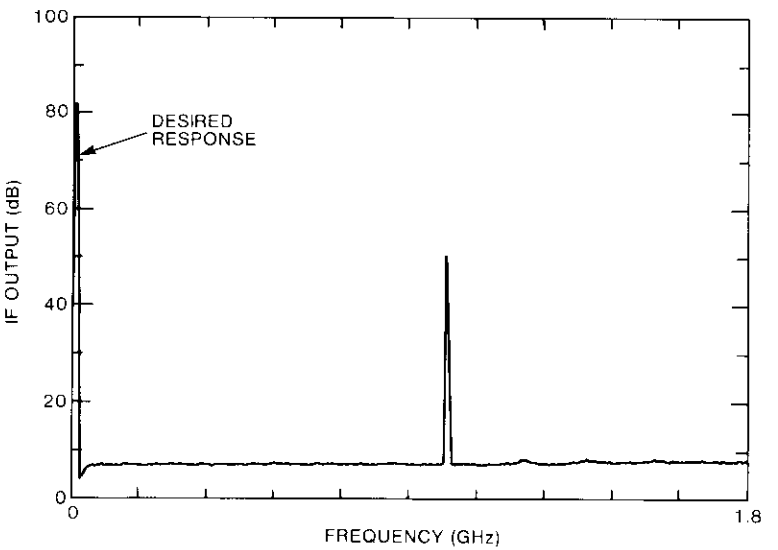

Figure 9. *Spurious Outputs*

Summary

The design of a consumer TVRO down-converter has been detailed. Through careful application of proven microwave circuits such as the push-push oscillator and subharmonically pumped mixer, a reliable consumer unit was produced. The use of a UHF television prescaler, precision analog tuning circuitry, and a well-controlled production program allowed the fabrication of a fully synthesized TVRO down-converter at an affordable price.

Acknowledgments

The authors would like to recognize the contributions of those who gave their time, effort, and skills to the D-200 project. The work of D. Brady, W. Lindblom, and H. Lambdin provided the foundation for the design. R. Stegens, R. Brooker, E. Keane, and E. Mandracchia provided advice and counsel on many technical subtleties. D. Hamner, M. Madorin, C. Mueth, R. Silcott, S. Wenzel, and S. Jiminez comprised the team responsible for building and testing the early hardware. H. Creamer, R. Lembke, and D. Hubert were responsible for the mechanical design, and P. Wilhelmsen for timely development of the production test system. Most importantly, the authors would like to thank L. Nevin, who made it all possible.

References

[1] F. McVay, "Don't Guess the Spurious Level of an Amplifier," *Electronic Design*, Vol. 15, No. 3, February 1, 1967, pp. 70–73.

[2] J. R. Bender and C. Wong, "Push-Push Design Extends Bipolar Frequency Range," *Microwaves & RF*, Vol. 22, No. 10, October 1983, pp. 91–98.

[3] L. E. Dickens and D. W. Maki, "An Integrated-Circuit Balanced Mixer, Image and Sum Enhanced," *IEEE Transactions on Microwave Theory and Techniques*, Vol. MTT-23, No. 3, March 1975, pp. 276–281.

Translations of Abstracts

Caractéristiques des évanouissements par trajets multiples sur les liaisons par satellite du service maritime en bande L

W. A. SANDRIN ET D. J. FANG

Sommaire

A l'intention particulière des ingénieurs des systèmes de télécommunications, on présente des modèles du processus d'évanouissement par trajets multiples dans les liaisons par satellite du service maritime en bande L. Ces modèles reposent essentiellement sur des données expérimentales obtenues de plusieurs sources. Ils comprennent des modèles d'évanouissement d'amplitude ainsi que de fréquence et de temps. Les premiers nommés comprennent un modèle de Rice destiné aux statistiques d'évanouissement (qui est applicable la plupart du temps) et un modèle de réflexion spéculaire qui présume une mer calme. Les modèles sont décrits de façon paramétrique en termes d'angle d'élévation et de gain d'antenne de la station navire. On définit également le spectre d'évanouissement (ou Doppler), les temps d'évanouissement et les largeurs de bande de correlation. Enfin, on examine des méthodes permettant de combattre les évanouissements par trajets multiples et pouvant être appliquées aux télécommunications maritimes commerciales.

Réseaux d'antennes à éléments en phase à 20 GHz utilisant des modules MMIC répartis

R. M. SORBELLO, A. I. ZAGHLOUL, B. S. LEE, S. SIDDIQI ET B. D. GELLER

Sommaire

On décrit des systèmes d'antennes à faisceaux d'exploration multiples et à faisceaux fixes multiples travaillant à 20 GHz et qui utilisent des modules de circuits intégrés hyperfréquence monolithiques (MMIC) qui fournissent la puissance radioélectrique et la valeur de phase dynamique voulues. Dans les configurations de réseaux alimentés à double réflecteur, on relève des réseaux en phase alimentant une paire de paraboles à foyer (confocal) pour des applications tant avec des faisceaux d'exploration que des